

National Technical University of Ukraine
“Igor Sikorsky Kyiv Polytechnic Institute”
Ministry of Education and Science of Ukraine

National Technical University of Ukraine
“Igor Sikorsky Kyiv Polytechnic Institute”
Ministry of Education and Science of Ukraine

Qualifying scientific work
on the rights of the manuscript

Liu Yang

UDC 628.165

DISSERTATION

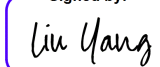
INCREASING THE EFFICIENCY OF CONTACT HUMIDIFIERS IN THE
OPERATING CONDITIONS OF THERMAL WATER DESALINATION SYSTEMS.

144 Thermal Power Engineering

14 – Electrical engineering

Submitted for the degree of Doctor of Philosophy

The dissertation contains the results of the author’s own research. All ideas, results, and
texts of other authors have been properly cited

Signed by:

2D8EEDC74C7B4E4... Liu Yang

Scientific Supervisor: Sereda Volodymyr Volodymyrovych, Candidate of Technical
Sciences, Associate Professor

Kyiv – 2025

ABSTRACT

Liu Yang. Increasing the efficiency of contact humidifiers in the operating conditions of thermal water desalination systems.

Dissertation for a Philosophy Doctor degree in specialty 144 Thermal Power Engineering. National Technical University of Ukraine “Igor Sikorsky Kyiv Polytechnic Institute” MES of Ukraine, Kyiv, 2025.

This dissertation is dedicated to the study of the air humidification process in a acrylic film-type contact heat exchanger under typical operating conditions of thermal water desalination systems.

The introduction explains the importance of the research topic, defines the object and subject of the study, highlights its scientific novelty, and states the aim and objectives. It also justifies the scientific principles and conclusions presented in the dissertation. Additionally, it details the practical significance of the findings, the author’s individual contribution, the validation of the findings, related publications, and outlines the scope and structure of the work.

Chapter 1 is devoted to the analysis of the current state of water desalination technologies and a review of contact humidifier designs used in thermal desalination systems. The chapter begins with an analysis of freshwater supply issues in China, identifying the regions most affected by water scarcity. It is shown that decentralized, small-scale seawater desalination is a promising solution for coastal areas and offshore islands. The chapter describes the main types of small-scale desalination units, including solar distillers, membrane systems, reverse osmosis, and humidification-dehumidification (HDH) systems. The advantages of HDH systems for use in remote and economically disadvantaged regions are discussed, along with factors that limit their implementation.

It is noted that significant attention in modern research is paid to the integration of HDH systems with power units based on steam turbines. In such hybrid schemes, the steam turbine acts as an electricity generator, and its exhaust steam serves as a heat source for the desalination process. Various configurations are considered in which the steam turbine condenser is used as an air or water heater for the HDH cycle. Analysis of

thermodynamic parameters showed that the optimization of working fluid expansion modes in the steam turbine and effective recovery of condensation heat allow increasing the total efficiency of the unit up to 94%, ensuring stable production of fresh water and electricity.

Particular attention is paid to the analysis of contact heat exchanger designs within HDH systems. It is established that the most common types of humidifiers are packed-bed towers and bubbling columns. The advantages and disadvantages of existing humidifier designs are summarized. The literature review reveals a lack of sufficient data on air and water pressure losses, which hinders a comprehensive assessment of humidifier performance, their energy and exergy indicators. Special attention is required for the selection of materials, which must combine corrosion resistance to aggressive environments (hot brine) with the necessary mechanical strength of the structure. Furthermore, the influence of thermal state of humidifier elements on their operational life and the stability of heat and mass transfer processes remains insufficiently studied.

The research presented in this dissertation is aimed at reducing the specific energy consumption of contact humidifiers under typical operating conditions of thermal desalination systems.

Chapter 2 describes the design of the experimental setup developed and constructed to investigate the air humidification process. The system features an open-air circuit and a closed water circuit. Its main components include a humidifier, a water heater, a pump, a fan, and a control and measurement system. The humidifier is a transparent acrylic tube, two meters in length, and with an internal diameter of 26 mm.

The choice of acrylic as a structural material is conditioned by its ability to ensure a stable stress state and a uniform thermal state of the wall due to low thermal conductivity. Unlike materials for bubble and spray humidifiers, acrylic demonstrates higher fracture toughness, which minimizes the risks of crack growth initiation and fatigue damage accumulation under conditions of frequent system startup and shutdown cycles.

To monitor the air temperature and humidity in real time, the setup employs instrumentation from *Regmik*, which enables a detailed analysis of heat and mass transfer dynamics during the humidification process. The system allows for adjustments to the

humidifier's thermal load, regulation of water and air flow rates, and systematic collection of experimental data. This setup makes it possible to study the energy performance of the humidifier under typical operating conditions of HDH systems.

An experimental procedure was developed, including data collection and processing methods, as well as calculation of the thermal balance between water and air, with a distinction between latent and sensible heat components. An error analysis was also conducted, accounting for uncertainties in both measurements and calculated parameters.

Chapter 3 investigates the operating parameters and energy performance of a tube film humidifier. It presents a classification of water film and air flow regimes within a vertical tube, along with an explanation of the mechanisms leading to flooding. The lack of clearly defined transition boundaries between flow regimes and the absence of accurate methods for determining air pressure losses below the flooding point have been noted.

The visual identification of flow regimes in the humidifier was carried out, and threshold values of water and air mass flow rates corresponding to regime transitions were established. It was found that at a superficial air velocity below 0.34 m/s, air pressure losses can be reliably determined using the Darcy-Weisbach equation. Based on this, it is recommended to limit the superficial air velocity in the humidifier to 0.34 m/s to minimize pressure losses and prevent contamination of the condensate with saltwater droplets.

The minimum water mass flow rate required to maintain continuous film flow was determined experimentally. The feasibility of using a minimum mass flow rate ratio of water to air ($MR = 2$) was substantiated. Under these conditions, maximum heat and mass transfer efficiency was achieved, ensuring optimal performance of the humidifier.

The influence of inlet water temperature (in the range up to 60 °C) on the intensity of heat and mass transfer processes was established. It is shown that increasing the temperature leads to an increase in humidifier productivity and outlet air temperature. Thermodynamic analysis revealed that with an increase in the temperature difference, the humidification efficiency decreases due to the increase in process irreversibility, while the exergy efficiency remains constant ($\eta_{hum}=0.58$). The obtained results confirm the energy feasibility of the proposed humidifier operating modes.

An important result of the operational tests is the confirmation of the durability of the humidifier's structural material. In the studied range of operating parameters, no signs of thermal deformation, clouding of the acrylic, or crack growth initiation were detected. This indicates that the heating-cooling operating cycles do not lead to critical changes in the stress state of the tube wall or the accumulation of fatigue damage, guaranteeing the durability of the structure.

Chapter 4 presents the developed thermodynamic model of a film humidifier based on heat and mass transfer equations. The model was validated using experimental data. New simplified empirical formulas were proposed to determine the heat and mass transfer coefficients in film humidifiers under the operating conditions of HDH systems. A calculation method was developed, which can be used for engineering design, techno-economic analysis, and operational optimization of film humidifiers in thermal desalination systems.

Modeling of the humidifier's performance was conducted, and the optimal geometric dimensions of the tube film humidifier were determined: a diameter of $d = 50$ mm and a height of $l = 1$ m. These parameters maximized the efficient use of the humidifier's volume, allowing high performance with minimal thermal and electrical energy consumption.

In addition, the influence of ambient air parameters on the operational characteristics of the film humidifier was analyzed. It was established that the apparatus productivity depends weakly on the ambient air temperature but decreases significantly with an increase in its relative humidity due to a decrease in the mass transfer potential. At the same time, it is shown that the gain output ratio (GOR) demonstrates a slight increase with an increase in both climatic parameters. This effect is explained by the decrease in the density of humid air and, consequently, the decrease in air mass flow rate, which leads to a reduction in the total thermal load on the humidifier.

Chapter 5 compares the energy performance of the investigated film humidifier with other common designs. A description of various types of packing materials widely used in HDH systems is provided. The operating parameters and energy characteristics of the humidifiers selected for comparison are presented.

The influence of the water-air mass flow ratio (MR) on evaporation intensity, thermodynamic efficiency, and air aerodynamic resistance was analyzed. It was established that in the temperature range characteristic of solar thermal systems (30–60 °C), the evaporation rate (ER) values for the film humidifier reach 200–800 kg/(m³·h), which is an order of magnitude higher than the indicators of systems with cellulose pads, Raschig rings, or paddy grass. The hydraulic advantages of the developed humidifier are separately substantiated: the absence of nozzles for water spraying allows creating the operating head exclusively due to the geometric height of the tube. This ensures minimal hydraulic losses on the liquid side compared to packed bed analogs, where energy costs for overcoming the resistance of sprayers are significant. It is demonstrated that the film humidifier ensures the highest evaporation intensity among all humidifier types. At the same time, its aerodynamic and hydraulic resistance is minimal. It is established that the use of a film humidifier allows reducing electricity consumption in the HDH system without deteriorating its productivity.

It was shown that the film humidifier achieves the highest evaporation intensity among all types analyzed, while maintaining minimal aerodynamic and hydraulic resistance. The results confirmed that using a film humidifier reduces the electricity consumption required for circulating water and air in the HDH system without compromising overall system performance.

The dissertation materials and research findings have been implemented at China Hydrogen Energy Group Co., Ltd and Liaoning Hongsheng Environmental Solutions Technology Co., Ltd.

Keywords: cycling air, energy efficiency, environmental safety, heat exchanger, heat transfer, mathematical model, separation, pressure losses, renewable energy, temperature gradient, thermal state, turbine, two-phase flow, water desalination plant, wastewater.

Publications presenting the main findings of the dissertation research.

Journal Articles:

1. Barabash, P., Solomakha, A., Sereda, V., Prytula, N., Strynada, P., **Liu, Y.** (2023). Heat and mass transfer of countercurrent air-water flow in a vertical tube. *Heat Mass Transfer*, 59, 1343–1351. <https://doi.org/10.1007/s00231-023-03342-2> (SCOPUS Q2).

Authors' contributions: Barabash P. provided scientific supervision; Solomakha A. developed methodology, fabrication of the experimental setup, participated in the experiments, writing, review and editing manuscript; Sereda V. performed the analysis and processing of experimental data, writing original draft; Prytula N. performed data visualization; Strynada P. funding acquisition; Liu Y. conducted the experiments.

2. Середя, В., Лю, Я., Подстєвая, Т. (2023). Високоєфективний контактний зволожувач для термічної опріснювальної установки. *Енергетика: економіка, технології, екологія*, 73(3), 131-138. doi:10.20535/1813-5420.3.2023.289729 (фахова, категорія Б).

Authors' contributions: Sereda V. was responsible for the research concept, scientific supervision, writing, review and editing the main text; Liu Y. developed the mathematical model of the humidifier, simulated its operation and writing original draft; Podstievaya T. conducted the literature review and performed data visualization.

3. Середя, В., Лю, Я., Подстєвая, Т. (2025). Експериментальне дослідження оптимальної продуктивності плівкового зволожувача для термічної системи опріснення. *Refrigeration Engineering and Technology*, 61(1), 25-36. doi:10.15673/ret.v61i1.3135 (фахова, категорія Б).

Authors' contributions: Sereda V. was responsible for the research concept, scientific supervision, fabrication of the experimental setup, writing, review and editing the main text; Liu Y funding acquisition, performed the literature review, analysis and processing of experimental data, writing original draft; Podstievaya T. conducted the experiments and performed data visualization.

Conference Proceedings:

1. Solomakha, A., Strynada, P., Barabash, P., Sereda, V., Prytula, N., **Liu, Y.** (2022). Mass transfer at fluid and gas countercurrent flow in vertical tubes. *International Conference of Young Scientists on Energy and Natural Sciences Issues: proceedings of the 18th International Conference* (pp. 406-409), May 24–27, 2022, Kaunas, Lithuania. Published by Lithuanian Energy Institute, 2022. ISSN 2783-6339, 796 p.

Author Contributions: Solomakha A. – conceptualization, methodology; Strynada P. – funding acquisition; Barabash P. – supervision; Sereda V. – formal analysis; Prytula N. – visualization; Liu Y. – investigation.

2. Лю, Я., Подстєвая, Т., Серєда, В. (2023). Високоєфективний контактний зволожувач для термічної опріснювальної установки. *Сучасні проблеми наукового забезпечення енергетики: матеріали XX Міжнародної науково-практичної конференція молодих вчених та студентів у 2-х т. (с. 226-227), м. Київ, 25–28 квітня 2023 р.* – Київ: КПІ ім. Ігоря Сікорського, видавництво «Політехніка», 2023. – ISBN 978-966-990-072-2 (Т. 1). – 256 с.

Author Contributions: Liu Y. – methodology, performing calculations; Podstievaia T. – literature review, visualization; Sereda V. – conceptualization, supervision.

3. Лю, Я., Подстєвая, Т., Серєда, В. (2025) Експериментальне дослідження оптимальної продуктивності плівкового зволожувача для термічної системи опріснення. *Сучасні проблеми наукового забезпечення енергетики: матеріали XXII Міжнародної науково-практичної конференції молодих вчених і студентів у 2-х т. (с. 164-166), м. Київ, 22–25 квітня 2025 р.* – Київ: КПІ ім. Ігоря Сікорського, видавництво «Політехніка», 2025. – ISBN 978-966-990-153-8 (Т. 1). – 215 с.

Author Contributions: Liu Y. – funding acquisition, formal analysis, literature review; Podstievaia T. – investigation, visualization; Sereda V. – conceptualization, supervision, methodology.

АНОТАЦІЯ

Лю Ян. Підвищення ефективності контактних зволожувачів в умовах роботи термічних систем знесолення води.

Дисертація на здобуття наукового ступеня доктора філософії за спеціальністю 144 «Теплоенергетика». – Національний технічний університет України "Київський політехнічний інститут імені Ігоря Сікорського", МОН України, Київ, 2025.

Дисертаційна робота присвячена дослідженню процесу зволоження повітря у акриловому контактному теплообміннику плівкового типу за характерних умов роботи термічних систем знесолення води.

У вступі висвітлено актуальність теми дослідження, визначено об'єкт, предмет, наукову новизну, мету та завдання дослідження. Обґрунтовано наукові положення та висновки, сформульовані в дисертації. Подано інформацію про практичне значення результатів, особистий внесок автора, апробацію результатів дисертації, публікації за темою дисертації, обсяг та структуру дисертації.

Розділ 1 присвячено аналізу сучасного стану технологій опріснення води та огляду конструкцій контактних зволожувачів, що застосовуються в термічних системах. Розділ починається з аналізу проблем забезпечення прісною водою в Китаї та визначення регіонів, які найбільше страждають від її нестачі. Показано, що децентралізоване маломасштабне опріснення морської води є перспективним рішенням для прибережних районів і морських островів. Описано основні типи маломасштабних установок опріснення, зокрема: сонячні дистилятори, мембранні системи, зворотний осмос та установки зволоження-осушення повітря (humidification-dehumidification, HDH). Зазначено переваги HDH-систем для використання у віддалених і малозабезпечених регіонах, а також визначено обмежувальні чинники їх впровадження.

Відмічено, що значна увага в сучасних дослідженнях приділяється інтеграції HDH-систем з енергетичними установками, основу яких складають парові турбіни. У таких гібридних схемах парова турбіна виконує функцію генератора електроенергії, а її відпрацьована пара слугує джерелом теплоти для процесу

опріснення. Розглянуто різні конфігурації, в яких конденсатор парової турбіни використовується як нагрівач повітря або води для HDH-контуру. Аналіз термодинамічних параметрів показав, що оптимізація режимів розширення робочого тіла в паровій турбіні та ефективна утилізація теплоти конденсації дозволяють підвищити сумарний ККД установки до 94%, забезпечуючи стабільне виробництво прісної води та електроенергії.

Значну увагу приділено аналізу конструкцій контактних теплообмінників у складі HDH-систем. Встановлено, що найпоширенішими зволожувачами є апарати з пакувальними матеріалами та барботажні колони. Узагальнено переваги та недоліки існуючих конструкцій зволожувачів. Огляд літератури засвідчив відсутність достатніх даних щодо втрат тиску повітря й води, що ускладнює комплексну оцінку ефективності зволожувачів та їх енергетичних і ексергетичних показників. Окремої уваги потребує питання вибору матеріалів, які повинні поєднувати корозійну стійкість до агресивного середовища (гарячого розсолу) з необхідною механічною міцністю конструкції. Також недостатньо вивченим залишається вплив нестаціонарного теплового стану елементів зволожувача на їх експлуатаційний ресурс та стабільність процесів тепломасообміну. Дослідження, викладене у цій дисертації, спрямоване на зменшення питомого енергоспоживання контактних зволожувачів в характерних умовах роботи термічних систем знесолення води.

Розділ 2 містить опис конструкції експериментальної установки, спроектованої та виготовленої для дослідження процесу зволоження повітря. Основними елементами установки є зволожувач, водяний нагрівник, насос, вентилятор, система регулювання та вимірювання параметрів. У якості зволожувача використано прозору акрилову трубку довжиною 2 м і внутрішнім діаметром 26 мм. Вибір акрилу як конструкційного матеріалу обумовлений його здатністю забезпечувати стабільний напружений стан та рівномірний тепловий стан стінки завдяки низькій теплопровідності. На відміну від матеріалів барботажних і розпилювальних зволожувачів, акрил демонструє вищу в'язкість руйнування, що мінімізує ризики ініціювання росту тріщин та накопичення втомних пошкоджень в умовах частих циклів пуску та зупинки системи.

Для моніторингу температури й вологості повітря в режимі реального часу застосовано контрольно-вимірювальну апаратуру компанії «Regmik», що дало змогу детально аналізувати динаміку тепломасообміну в процесі зволоження повітря. Розроблена система дозволяє змінювати теплове навантаження зволожувача, регулювати витрати води та повітря й здійснювати систематичний збір даних. Така установка дає змогу досліджувати енергетичні характеристики зволожувача у характерних для HDH-систем режимах.

Розроблено методику проведення експериментів, яка включає процедури збору та обробки даних, а також розрахунок теплового балансу між водою і повітрям із виокремленням часток прихованої та явною теплоти. Проведено аналіз похибок, що можуть виникати як у процесі вимірювань, так і під час обчислення розрахункових параметрів.

У розділі 3 досліджено режимні параметри та енергетичні характеристики трубного плівкового зволожувача. Наведено класифікацію режимів течії водяної плівки та повітря у вертикальній трубці, а також описано механізми виникнення затоплення. Зазначено відсутність чітких меж переходів від одного режиму течії до іншого та точних методів визначення втрат тиску повітря нижче точки затоплення.

Проведено візуальну ідентифікацію режимів течії в зволожувачі, встановлено граничні значення масових витрат води і повітря, за яких відбувається перехід між режимами. Виявлено, що за поверхневої швидкості повітря менше 0.34, втрати тиску за повітрям можна достовірно визначати за допомогою формули Дарсі–Вейсбаха. Запропоновано обмежити поверхневу швидкість повітря в зволожувачі до 0.34, що дозволяє мінімізувати втрати тиску та уникнути забруднення конденсату краплями солоної води.

Експериментально встановлено мінімальне значення масової витрати води, необхідне для підтримання безперервного протікання плівки. Обґрунтовано доцільність використання мінімального співвідношення масових витрат води до повітря $MR = 2$. За таких умов забезпечується максимальна ефективність тепломасообміну та ефективна робота зволожувача.

Встановлено вплив температури води на вході до зволожувача (в діапазоні до 60 °C) на інтенсивність процесів тепломасообміну. Показано, що підвищення

температури призводить до зростання продуктивності зволожувача та вихідної температури повітря. Термодинамічний аналіз виявив, що зі збільшенням температурного напору ефективність зволоження знижується через зростання незворотності процесів, водночас ексергетичний ККД залишається постійним ($\eta_{hum}=0,58$). Отримані результати підтверджують енергетичну доцільність запропонованих режимів роботи зволожувача.

Важливим результатом експлуатаційних випробувань є підтвердження стійкості конструкційного матеріалу зволожувача. У досліджуваному діапазоні режимних параметрів не виявлено ознак термічної деформації, помутніння акрилу або ініціювання росту тріщин. Це свідчить про те, що робочі цикли нагріву-охолодження не призводять до критичних змін напруженого стану стінки труби та накопичення втомних пошкоджень, гарантуючи довговічність конструкції.

У розділі 4 розроблено термодинамічну модель плівкового зволожувача на основі рівнянь тепломасообміну. Проведено валідацію моделі на основі експериментальних даних. Запропоновано нові спрощені емпіричні формули для визначення коефіцієнтів тепло- і масовіддачі у плівкових зволожувачах за режимних параметрів HDH-систем. Розроблено метод розрахунку, який може бути використано для інженерного проєктування плівкових зволожувачів, техніко-економічного аналізу та оптимізації режимів їхньої роботи в термічних системах опріснення води.

Проведено моделювання роботи плівкового зволожувача. Визначено оптимальні геометричні розміри трубного плівкового зволожувача: діаметр $d = 50$ мм та висота $l = 1$ м. За таких параметрів об'єм зволожувача використовується максимально ефективно, що дозволяє досягти високої продуктивності за найнижчих витрат теплової та електричної енергії.

Крім того, проаналізовано вплив параметрів зовнішнього повітря на експлуатаційні характеристики плівкового зволожувача. Встановлено, що продуктивність апарата майже не залежить від температури зовнішнього повітря, проте суттєво знижується зі зростанням його відносної вологості внаслідок зменшення потенціалу масопереносу. Водночас показано, що коефіцієнт енергетичної ефективності (GOR) демонструє незначне зростання у разі

підвищення обох кліматичних параметрів. Цей ефект пояснюється зниженням густини вологого повітря та, відповідно, зменшенням масової витрати повітря, що призводить до зниження загального теплового навантаження на зволожувач.

У п'ятому розділі проведено порівняння енергетичних показників досліджуваного плівкового зволожувача з іншими поширеними конструкціями. Наведено опис різних типів пакувального матеріалу, які широко застосовуються у HDH-системах. Представлено режимні параметри та енергетичні характеристики зволожувачів, які було обрано для порівняння.

Проаналізовано вплив коефіцієнта співвідношення масових витрат води і повітря (MR) на інтенсивність випаровування, термодинамічну ефективність та аеродинамічний опір повітря. Встановлено, що у характерному для геліотермічних систем діапазоні температур ($30\text{--}60\text{ }^{\circ}\text{C}$) значення ER для плівкового зволожувача досягають $200\text{--}800\text{ кг}/(\text{м}^3\cdot\text{год})$, що на порядок вище за показники систем із целюлозними насадками, кільцями Рашига або рисовою травою.

Окремо обґрунтовано гідравлічні переваги розробленого зволожувача: відсутність форсунок для розпилення води дозволяє створювати робочий напір виключно за рахунок геометричної висоти трубки. Це забезпечує мінімальні гідравлічні втрати на стороні рідини порівняно з насадковими аналогами, де витрати енергії на подолання опору розпилювачів є значними.

Продемонстровано, що плівковий зволожувач забезпечує найвищу інтенсивність випаровування серед усіх типів зволожувачів. Водночас його аеродинамічний та гідравлічний опір є мінімальним. Встановлено, що використання плівкового зволожувача дозволяє знизити споживання електроенергії в HDH-системі без погіршення її продуктивності.

Матеріали дисертації та результати досліджень впроваджено в компаніях China Hydrogen Energy Group Co., Ltd. та Liaoning Hongsheng Environmental Solutions Technology Co., Ltd.

Ключові слова: відновлювана енергетика, втрати тиску, двофазний потік, екологічна безпека, енергоефективність, математична модель, опріснювальна установка, розділення, стічні води, температурний градієнт, тепловий стан, теплообмінник, теплопередача, турбіна, циркуляційне повітря.

TABLE OF CONTENTS

LIST OF SYMBOLS AND ABBREVIATIONS	16
INTRODUCTION	19
CHAPTER 1. REVIEW OF CONTACT HUMIDIFIER DESIGNS IN THERMAL WATER DESALINATION SYSTEMS	24
1.1. Problems of Supplying Clean Drinking Water in China	24
1.2. Small-Scale Desalination Systems.....	27
1.2.1. Solar Distillers.....	28
1.2.2. Membrane Systems	29
1.2.3. Reverse Osmosis	30
1.2.4. Air Humidification-Dehumidification (HDH) Cycle	32
1.2.5. Combination of humidification-dehumidification and power cycles	33
1.3. Overview of Contact Humidifier Designs	36
1.4 Conclusions to Chapter 1, Research Aim and Objectives	53
CHAPTER 2. EXPERIMENTAL SETUP AND METHODOLOGY FOR STUDYING THE AIR HUMIDIFICATION PROCESS	55
2.1. Design and Layout of the Experimental Setup	55
2.2. Research Methodology and Measurement Error Assessment	60
2.3. Experimental Data Processing Methodology.....	66
2.3.1. Heat Balance of the Humidifier	66
2.3.2. Determination of the Humidifier's Energy Performance Indicators	70
2.4. Assessment of Calculation Uncertainty	72
2.5. Conclusions to Chapter 2	76
CHAPTER 3. RESULTS OF STUDYING THE OPERATING PARAMETERS AND ENERGY CHARACTERISTICS OF THE CONTACT HUMIDIFIER	77
3.1. Design Air Flow Rate	77
3.1.1. Water Film and Air Flow Regimes in a Vertical Tube.....	77
3.1.2. Flooding Point.....	78
3.1.3. Determination of the Optimal Air Flow Rate	80

	15
3.2. Optimal MR Ratio.....	84
3.3. Energy Efficiency Indicators	87
3.4. Conclusions to Chapter 3	88
CHAPTER 4. THERMODYNAMIC MODEL DESING AND CALCULATION	
METHOD	90
4.1. Mathematical Description of the Model	90
4.2. Results of Mathematical Modeling	93
4.2.1. Optimal Geometric Dimensions of the Humidifier	93
4.2.2. Influence of External Air Parameters on the Humidifier Efficiency	99
4.3. Development of a calculation method	101
4.4. Conclusions to Chapter 4.	104
5. COMPARATIVE ANALYSIS OF THE HUMIDIFIERS' PERFORMANCE	106
5.1. Comparison of a Film Humidifier with Packed Bed Humidifiers	106
5.2. Comparison of a Film Humidifier with Bubble Columns	114
5.3. Comparison of a Film Humidifier with Atypical Designs.....	117
5.4. Conclusions to Chapter 5	122
CONCLUSIONS.....	123
REFERENCES.....	125
APPENDIX A: LIST OF PUBLICATIONS.....	135
APPENDIX B: THE ACT OF IMPLEMENTATION IN THE CHINA HYDROGEN ENERGY GROUP	136
APPENDIX C: THE ACT OF IMPLEMENTATION IN THE LIAONING HONGSHENG ENVIRONMENTAL SOLUTIONS TECHNOLOGY	137

LIST OF SYMBOLS AND ABBREVIATIONS

Symbols:

- c_p – specific heat capacity, J/(kg·K)
 D – diffusion coefficient of water vapour into air, m²/s
 d – humidifier inner diameter, m
 E – exergy, W.
 f – frictional factor
 F_{hum} – humidifier interphase surface area ($= \pi dl$), m²
 J – diffusion flux, kg/(m²·s)
 j – superficial phase velocity
 h – specific enthalpy, J/kg
 h_{con} – convective heat transfer coefficient, W/(m²·K)
 h_d – mass transfer coefficient, m/s
 h_{vl} – latent heat of water, J/kg
 m – mass flow rate, kg/s
 M_a – molar air mass (=28.96), g/mol;
 M_v – water vapor molar mass (=18.02), g/mol
 N – power, W
 Nu – Nusselt number
 Pr – Prandtl number
 p_{par} – partial pressure of water vapor in moist air, Pa
 Q – heat transferred, W
 R_a – air gas constant (=287.2), J/(kg·K);
 R_v – water vapor gas constant (=461.53), J/(kg·K);
 Re_a – Reynolds number of moist air ($= w_{a,in} d / \nu_a$)
 Re_f – film Reynolds number ($= 4\Gamma / \mu_a$)
 s – entropy, J/(kg·K)
 Sc_a – Schmidt number of moist air ($= \nu_a / D$)
 Sh – Sherwood number

t – temperature, °C

$t_{a,aver}$ – average temperature of moist air in a humidifier ($= 0.5[t_{a.in} + t_{a.out}]$), K

V – volume, m³.

w – velocity, m/s

l – length, m

Greek Letters:

Γ – mass flow rate per unit perimeter, ($= m_w / [\pi d]$), kg/(m s)

ΔP – pressure drop, Pa/m

ΔT – mean logarithmic temperature difference in humidifier,

$$\left(= \frac{(t_{w,out} - t_{a,in}) - (t_{w,in} - t_{a,out})}{\ln \frac{(t_{w,out} - t_{a,in})}{(t_{w,in} - t_{a,out})}} \right), \text{ K}$$

$\Delta \omega$ – mass flow rate of moisture transferred from hot water to air, kg/s

ε – exergetic efficiency

η – effectiveness

λ – thermal conductivity, W/(m·K)

μ – dynamic viscosity, [Pa·s]

ρ – density. kg/m³

ν – kinematic viscosity, m²/s

ϕ – relative humidity of air

ω – humidity ratio of air, kg water/kg dry air

Sub- and superscripts

a – moist air

con – convective

$calc$ – calculated

$evap$ – evaporation

exp – experimental

hmt – heat and mass transfer

hum – humidifier

id – ideal

in – humidifier inlet

out – humidifier outlet

v – water vapor

w – water

Abbreviations:

ABS – Acrylonitrile Butadiene Styrene

ER – evaporation rate per unit humidifier volume

GOR – gain output ratio

HDH – humidification-dehumidification

HDH-PWR – humidification-dehumidification and power cycle

MD – membrane distillation

MR – mass flow rate ratio

ORC – organic Rankine cycle

PVC – polyvinyl chloride

SEC – specific energy consumption

SD – solar distiller

RO – reverse osmosis

INTRODUCTION

Relevance of the Work. In the near future, the rapid growth of the global population and the pollution of freshwater sources by industrial waste are expected to lead to a global freshwater shortage. Identifying new sources of freshwater is essential to overcoming this threat. Considering that seawater accounts for 97% of the world's water resources, desalination technologies represent one of the most effective solutions to address freshwater scarcity – particularly in coastal and offshore island regions.

Currently, the development of decentralized and small-scale freshwater production solutions is especially relevant. These solutions are suitable for remote communities that lack access to electricity or centralized water distribution networks. One of the most promising in this context is seawater desalination based on the humidification-dehumidification (HDH) process. This method offers several advantages, including moderate operating temperatures, atmospheric pressure operation, simple system design, and low capital operating costs. However, existing HDH systems still consume significant amounts of thermal and electrical energy to remove the salts from seawater.

By addressing the limitations of the previous research and providing comprehensive experimental data on the hydrodynamics and heat and mass transfer processes during air humidification, this study contributes to the development of energy-efficient film humidifiers for small-scale HDH systems. The results are expected to play a key role in optimizing HDH system performance for minimal energy consumption, thereby improving overall system efficiency and enabling operation based entirely on renewable energy sources.

Connection of work with research programmes, plans, and topics.

The topic of the dissertation aligns with the priority areas of scientific and technological development and innovation activity – namely, “Energy and Energy Efficiency” and “Rational Use of Natural Resources” – as outlined in the Law of Ukraine “On Amendments to Certain Laws of Ukraine on Priority Areas of Science and Technology Development and Innovation” dated December 21, 2023. The research focuses on the investigation of hydrodynamic, heat and mass transfer processes during

air humidification in direct contact heat exchangers. It is aimed at increasing the efficiency of seawater and brackish water desalination.

Some materials of the dissertation research were part of the study programs and projects which were implemented at the Department of Heat and Alternative Power Engineering of the National Technical University of Ukraine “Igor Sikorsky Kyiv Polytechnic Institute”, including:

- Development and preparation of innovative distillers for the concentration of thermosensitive solutions (state registration number 0121U110195);
- Development and manufacture of a mass-exchange centrifugal distiller for the recovery of drinking water in extreme conditions (state registration number 0123U101994).

Aim and objectives of the research.

This research aims to enhance the performance of thermal water desalination systems based on the humidification-dehumidification (HDH) cycle by reducing the specific energy consumption of direct contact humidifiers.

Following the aim, the main objectives of the research are as follows:

1. To analyze the existing designs of direct contact heat exchangers used in HDH systems, identify their advantages and limitations, and evaluate and compare the energy efficiency indicators of various types of humidifiers.
2. To experimentally investigate the hydrodynamics and heat and mass transfer during air humidification in a tube contact heat exchanger under typical operating conditions of HDH systems.
3. Based on the analysis of the research results, determine the geometric dimensions of the setup and the air and water flow rates to obtain the maximum performance and energy efficiency of the HDH system.
4. To develop a model for calculating a tube contact heat exchanger when used as a humidifier in a thermal water desalination system.
5. To compare the efficiency of a tube film heat exchanger with other common humidifier designs.

Object of the research: the air humidification process in a film-type direct contact heat exchanger under typical operating conditions of thermal desalination systems.

Subject of the research: the influence of operating parameters of thermal desalination systems on the energy performance of direct contact humidifiers.

Methods of the research.

The scientific and methodological basis of the study includes experimental methods, mathematical and thermodynamic modeling, as well as methods of analysis and comparison. Experimental and theoretical results were processed using application software packages such as Mathcad and Microsoft Excel.

The scientific novelty of the results is as follows:

1. New experimental data on hydrodynamics and heat and mass transfer during air humidification, obtained over a wide range of changes in the main operating parameters of HDH systems, have been obtained, which expanded the possibilities of analyzing the influence of air velocity, water flow rate, and water temperature on the energy performance characteristics of a film humidifier.

2. For the first time, the limiting value of superficial air velocity has been experimentally substantiated, ensuring intensive heat and mass transfer without transition to the “flooding” regime and droplet contamination of the distillate. This made it possible to achieve the lowest pressure losses and maintain stable, efficient operation of the film humidifier.

3. For the first time, the minimum value of the mass flow rate coefficient required to ensure continuous flow of the liquid film has been experimentally determined. This finding enables the prevention of a sharp decrease in the efficiency of heat and mass transfer, and ensures optimal humidification performance with minimal energy consumption.

Practical values of the research findings.

1. The main shortcomings of the most common types of humidifiers used in thermal desalination systems have been identified, namely: high specific electricity consumption, significant aerodynamic resistance, and lack of data on water pressure losses. All of this

complicates the comprehensive analysis of existing humidifier designs, making it impossible to determine their economic and exergy efficiency.

2. Based on the experimental data obtained, an engineering calculation method for a film-type contact humidifier has been developed. This method can be used for engineering design of film humidifiers, techno-economic analysis, and optimization of their operating modes in water desalination, air conditioning, or heat recovery systems.

3. It has been proven that the use of a film contact heat exchanger will lead to a reduction in electricity consumption required for water and air circulation in the HDH system without degrading its performance.

The results of the dissertation research have been tested at China Hydrogen Energy Group Co., Ltd. and Liaoning Hongsheng Environmental Solutions Technology Co., Ltd.

Personal contribution of the author.

The scientific results presented in this dissertation have been obtained by the author and include the following contributions:

- development of the experimental setup;
- formulation of experimental procedures and data processing techniques;
- processing, analysis, interpretation, and generalization of the experimental results;
- development of a thermodynamic model and a calculation method for the film humidifier.

The dissertation was performed at the Department of Heat and Alternative Power Engineering of the Educational and Scientific Institute of Nuclear and Thermal Energy at the National Technical University of Ukraine “Igor Sikorsky Kyiv Polytechnic Institute” under the scientific supervision of Volodymyr Sereda, Candidate of Science (Engineering), Associate Professor.

Approval of dissertation results.

The materials of the dissertation were reported and discussed at the following conferences: 18th International Conference of Young Scientists on Energy Issues (Lithuania, Kaunas, May 24–27, 2022), XX International Scientific and Practical Conference of Young Scientists and Students “Modern Problems of Scientific Support

for Energy” (Ukraine, Kyiv, April 25–28, 2023), XXII International Scientific and Practical Conference of Young Scientists and Students “Modern Problems of Scientific Support for Energy” (Ukraine, Kyiv, April 22–25, 2025).

Publications. The main results of the dissertation were published in six scientific publications, including three journal articles (one of which is SCOPUS (Q2) and Web of Science (Q2) indexed, another is published in a professional journal of Ukraine of Category B), and three conference papers.

Structure and scope of work. The dissertation consists of an introduction, five chapters, three appendixes, and a list of references comprising 83 sources. The total volume of the work is 136 pages, including 78 figures and 19 tables.

CHAPTER 1. REVIEW OF CONTACT HUMIDIFIER DESIGNS IN THERMAL WATER DESALINATION SYSTEMS

1.1. Problems of Supplying Clean Drinking Water in China

At present, the shortage of fresh water is one of the key global issues threatening socio-economic stability and ecological balance in many regions of the world. With population growth, rapid urbanization, and climate change, the demand for fresh water is constantly increasing, while available natural resources remain limited [1].

In 2024, the United Nations included China among the 13 countries in the world facing the most severe water shortages. According to the latest statistics covering 149 countries and regions, China ranked 110th globally in terms of per capita water resources. This acute shortage is especially pronounced in urban areas, where the number of residents living in water-scarce regions significantly exceeds that of other countries, highlighting the scale and urgency of China's water crisis. The population inhabiting water-deficient areas has reached 160 million, accounting for 21% of the global population residing in water-scarce areas. Out of 669 cities in China, 400 suffer from insufficient water supply, and 110 face severe water scarcity, which amounts to 16 million cubic meters daily. The total freshwater resources in China amount to approximately 2.8 trillion m³. In terms of per capita water availability, the country ranks 88th globally [2]. In China, a rapidly urbanizing country, about 300 million people lack access to clean drinking water, and nearly 90% of coastal cities experience water shortage [3]. Annual industrial and economic losses caused by water shortages exceed 230 billion yuan. The country's total water consumption has increased from over 500 billion cubic meters in the past to approximately 800 billion cubic meters, accounting for more than 28% of its available water resources [4]. According to international experience, when a country's water consumption exceeds 20% of its available water resources, it is highly likely to face a water crisis.

Water resources in China are extremely unevenly distributed. The southern part of the country is rich in water resources, whereas the northern and western regions suffer

from acute water shortages. In the Yellow River basin and the North China Plain, there is a huge demand for water from both agriculture and cities, while local water resources are limited. This leads to excessive groundwater extraction, land subsidence, and ecological problems. Furthermore, the eastern coastal areas of China, which are important economic and agricultural centers, are constrained in their development by the lack of water [5].

According to the study [6], 67 out of 131 major lakes in China have reached a state of eutrophication. The eutrophication of lakes and reservoirs has significantly deteriorated water quality in nearby cities, seriously affecting the health and well-being of residents. Moreover, urban rivers have been blocked, the water levels in lakes and reservoirs have declined, and the availability of land and water resources for ecological purposes has been restricted. For instance, in Shenzhen, there have been cases of unauthorized encroachment on reservoir management boundaries and the occupation of lands allocated for water-related ecological functions [6].

An analysis in [7] estimates China's total water shortage at approximately 300-400 mln. m³, assuming current average demand is met without overexploitation of groundwater. The economic losses caused by water scarcity exceed those from flooding [8]. In many regions of China, this shortage has led to intense competition for water between industry and agriculture, and between urban and rural areas.

For a long time, the water scarcity problem has been underestimated. Many have assumed that water resources, as public property, should be used freely or at a very low cost [9]. As a result, while there is a clear shortage of water resources, wasteful practices remain widespread. For example, although China is a major agricultural country, agriculture accounts for 61% of national water consumption, yet the utilization efficiency is only around 40%. In contrast, developed countries typically achieve utilization rates of 70% to 80% [10].

Laws and regulations regarding water resource recycling in China remain imperfect. Existing legislation includes the Water Law of the People's Republic of China, the Law on Prevention and Control of Water Pollution, and the Environmental Protection Law [11]. However, current regulations are incomplete, sector-specific standards are lacking, and many laws are outdated, which complicates the effective management of

freshwater use. For instance, the Law on Promoting Circular Economy, adopted in August 2018, only encouraged industrial enterprises to implement advanced water-saving technologies and equipment to fulfil water conservation plans and strengthen water management aimed at emission reduction, but it did not provide specific provisions on water resource recycling.

Effective water resource recycling cannot be separated from the support of advanced technologies, such as water saving, wastewater treatment, seawater desalination, reuse of treated water, and rainwater harvesting. The development of these technologies in China significantly lags behind the leading international standards. As a result, operational costs for using and recycling water resources remain very high [12]. Small and medium-sized enterprises tend to avoid adopting wastewater treatment technologies, which limits economic development. A large volume of domestic and industrial wastewater is directly discharged into rivers, lakes, and reservoirs without treatment, causing severe pollution. Furthermore, the construction of urban wastewater treatment facilities is seriously lagging, with nearly 10% of cities lacking any treatment plants [13]. Some existing treatment facilities are either inefficient or non-operational, leading to ineffective wastewater treatment. The coefficient of direct reuse of urban wastewater in China is less than 30% [14]. Many water supply projects face issues related to aging infrastructure and emergency conditions, with occasional damages and leaks resulting in significant water losses.

Given the critical need to enhance water treatment and recycling technologies, seawater desalination emerges as a vital and complex solution. This technology involves marine science, information technology, chemical and energy industries, employing new materials, along with other disciplines. Desalination can play an important role in the fields of electronics, power generation, bioengineering, medicine (therapy), chemical industry, and environmental protection. As a key component of the circular economy and clean production, seawater desalination technologies will stimulate related industries to increase annual production value by tens of billions of euros and bring significant economic, social, and environmental benefits.

The technology of water desalination emerged between the 1950s and 1960s. Initially, it was used on ships and islands. With the continuous advancement of technology and the expansion of freshwater-scarce regions, seawater desalination was gradually introduced and applied on vessels. Countries have attached great importance to it and progressively started to implement it in industrial and civil sectors.

Desalination is a technical process that removes salt and other impurities from seawater through chemical or physical methods to obtain fresh water. After decades of technological development, modern seawater desalination technologies used for international commercial purposes can be divided into two categories: industrial (large-scale) and decentralized (small-scale) desalination.

The development of small-scale seawater desalination is an important means of increasing water reserves and optimizing the water supply structure in China. Small-scale desalination is suitable for small communities with a freshwater demand of less than 20 cubic meters per day. Renewable energy sources can be used for small desalination systems in remote communities, which helps minimize transportation costs. In addition, local or decentralized desalination methods are appropriate for small factories, laboratories, and emergencies. However, the cost of producing fresh water in decentralized desalination systems is higher than in large-scale systems [1].

Thus, decentralized seawater desalination is of great importance for alleviating water resource constraints in coastal areas and offshore islands, and for ensuring the sustainable development of China's economy and society.

1.2. Small-Scale Desalination Systems

In China, the promotion of small-scale desalination systems can effectively address water shortages, reduce the use of groundwater, support local economic and environmental protection, and contribute to sustainable development. Small-scale desalination technologies include solar distillers, membrane systems, reverse osmosis, and humidification-dehumidification units [1]. These technologies often use both

renewable energy (particularly solar energy) and secondary energy sources (waste heat). Let us consider the advantages and disadvantages of small-scale desalination systems.

1.2.1. Solar Distillers

A solar distiller (SD) has a simple design (Fig. 1.1). Brackish or seawater evaporates in a container under direct solar radiation, which passes through transparent glass or plastic. The evaporated water then condenses and flows from the top of the distiller to the sides of the container, where it can be collected. The resulting fresh water is of high quality, as microorganisms and salts remain in the tank [15].

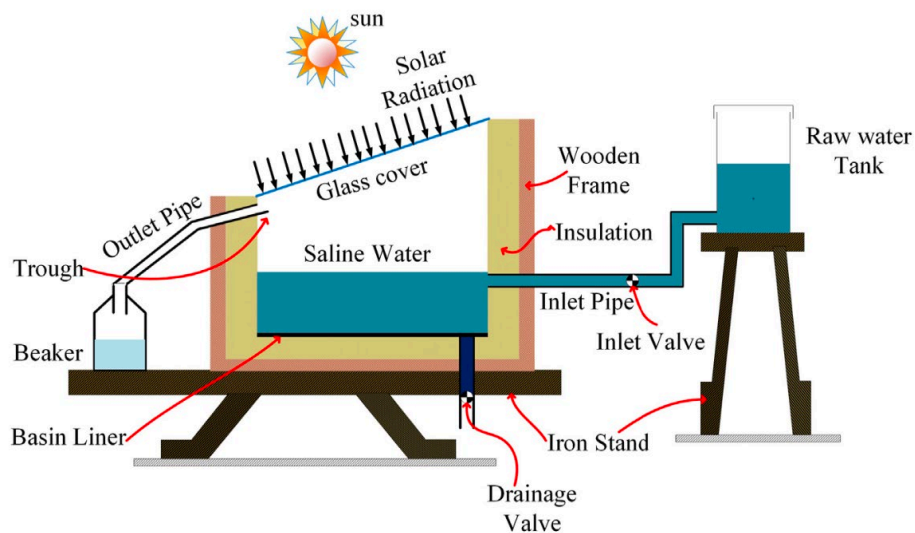


Fig 1.1. Diagram of a solar distiller [15].

SD were extensively studied in [15-21]. It was established that the performance of such a system is influenced by various operating parameters, including the intensity of solar radiation, water level, ambient temperature, type of glass, tilt angle and thickness of the cover, and wind speed. Even under ideal operating conditions, a solar distiller has an efficiency of less than 45%, with a maximum daily output of five liters of fresh water per square meter [21].

The primary reason for the low efficiency of a SD is the loss of latent heat of water vapor condensation on the glass cover [16, 17]. A SD with low productivity cannot

economically compete with other desalination methods. However, due to the low demand for fresh water, a solar distiller, as a small-scale desalination system, remains competitive.

Single-stage SDs have not been widely adopted because of their low productivity. The tilt angle of the glass cover depends on the latitude of the solar distiller's location [18]. The optimal tilt angle is determined by the intensity of solar radiation and the average variation of the azimuth angle [19, 20]. A thicker glass cover with lower thermal conductivity can reduce heat transfer. Lowering the temperature of the cover increases the production of fresh water [21].

Overall, the solar distillation apparatus has the lowest thermal efficiency among thermal desalination systems. Nevertheless, its thermal efficiency can be improved using various active and passive methods [15-18].

1.2.2. Membrane Systems

Membrane distillation (MD) is a new technology that combines the advantages of thermal and membrane desalination. Membranes have significant advantages, including a simple operation process, a high salt rejection, and a compact design. There are studies focused on improving the energy efficiency and freshwater production by integrating membranes with solar collectors [22-28].

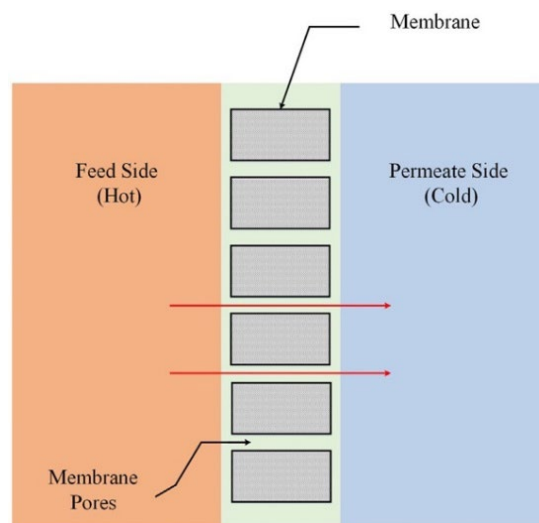


Fig. 1.2. Schematic diagram of the membrane distillation [23].

A schematic diagram of membrane distillation is shown in Fig. 1.2. Typically, a microporous membrane serves as a physical barrier separating the heated saline water from the cooler chamber. Due to the non-isothermal nature of the process, vapor molecules move from the chamber with higher water vapor pressure to the chamber with lower water vapor pressure (from the warmer side to the cooler side) through the membrane pores.

Overall, the mechanism of distillate transfer in MD can be divided into the following stages [24];

- evaporation of water from the heated side of the membrane;
- transport of water vapor through the non-wetted pores;
- condensation of the transferred water vapor on the permeate side of the membrane.

MD systems can achieve a high water recovery rate from water with high salinity and are suitable for small-scale and domestic applications [22, 23]. Membranes require low-grade thermal energy (from 30 to 90°C), which can be provided by solar radiation [25, 26]. Photovoltaic panels can also supply the necessary power for the MD operation [27]. The MD advantages include the following: no need for pretreatment of saline water; low operating temperature; capability of desalinating high-salinity water; and potential integration with solar energy [24-28]. However, MD systems also have disadvantages, such as high capital costs, the need for a large membrane surface area, membrane wetting, and low durability [22, 23, 25, 27].

1.2.3. Reverse Osmosis

Reverse osmosis (RO) is a process in which a solvent passes through a semi-permeable membrane into a solution with a high concentration of solute. This process equalizes the solute concentrations on both sides of the membrane. RO uses pressure as the driving force to overcome the osmotic pressure of the saline solution.

A RO system consists of four main components: a pretreatment system, a high-pressure pump, a membrane unit, and a post-treatment system (Fig. 1.3). Pretreatment is

very important, as the membrane surface must be kept clean. All suspended solids and microbial bacteria need to be removed. High-pressure pumps provide pressure in the range of 1 to 7 MPa. The pressure forces clean water through the membrane while salts are retained and removed. Post-treatment includes stabilizing the water quality by adjusting the pH and disinfecting the water [29].

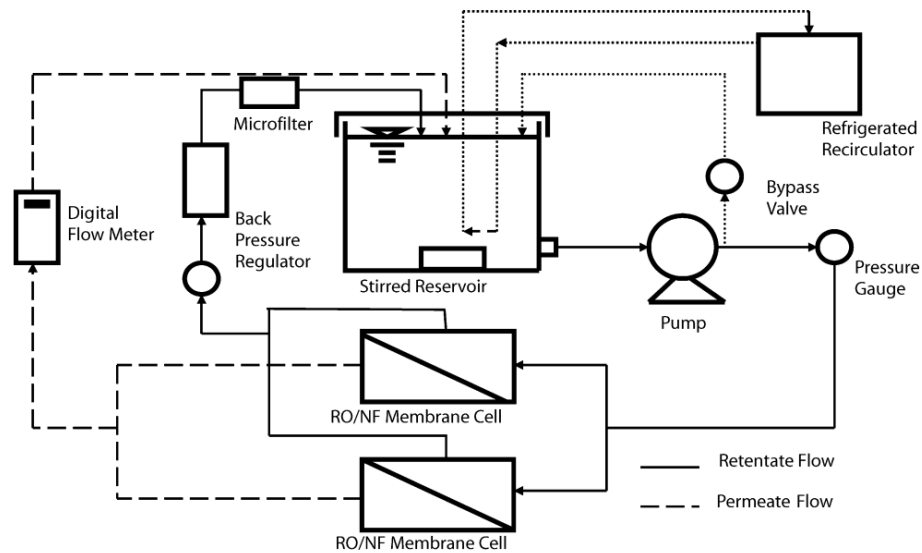


Fig. 1.3. Schematic of the reverse osmosis desalination system [29]

The advantages of reverse osmosis include continuous operation (24 hours a day), high water flow rate with a new membrane, high water recovery rate, salt removal efficiency of up to 99.5%, and low energy consumption ($\approx 6 \text{ kWh/m}^3$) [30-35]. The disadvantages include the need for additional pretreatment, since pesticides, herbicides, and chlorine have smaller molecules than water and may pass through the membrane; removal of natural minerals; and high water loss through the system [34, 35].

The major limiting factor for the widespread adoption of reverse osmosis in China is its high cost and the technical requirements for concentrate pretreatment [34]. In addition, the RO process is sensitive to the temperature of the feed seawater. The acceptable temperature range for seawater is from 15°C to 35°C in the northern offshore areas (such as the Bohai Bay). Low water temperature requires additional measures to be taken to raise it. As a result, the cost of RO desalination increases [34].

1.2.4. Air Humidification-Dehumidification (HDH) Cycle

Desalination through humidification-dehumidification (HDH) is a thermal cycle that functions similarly to the natural water cycle. The core principle of the HDH cycle is comparable to that of solar distillers. However, in solar distillers, during condensation, all the latent heat of water evaporation is lost to the environment, leading to low thermal efficiency. The HDH cycle enhances this process by separating evaporation and condensation into different devices. This enables the recovery of the latent heat of evaporation and its reuse for heating [33-36].

An HDH system (Fig. 1.4) primarily consists of two heat exchangers – a humidifier and a dehumidifier – connected at the top to enable air circulation.

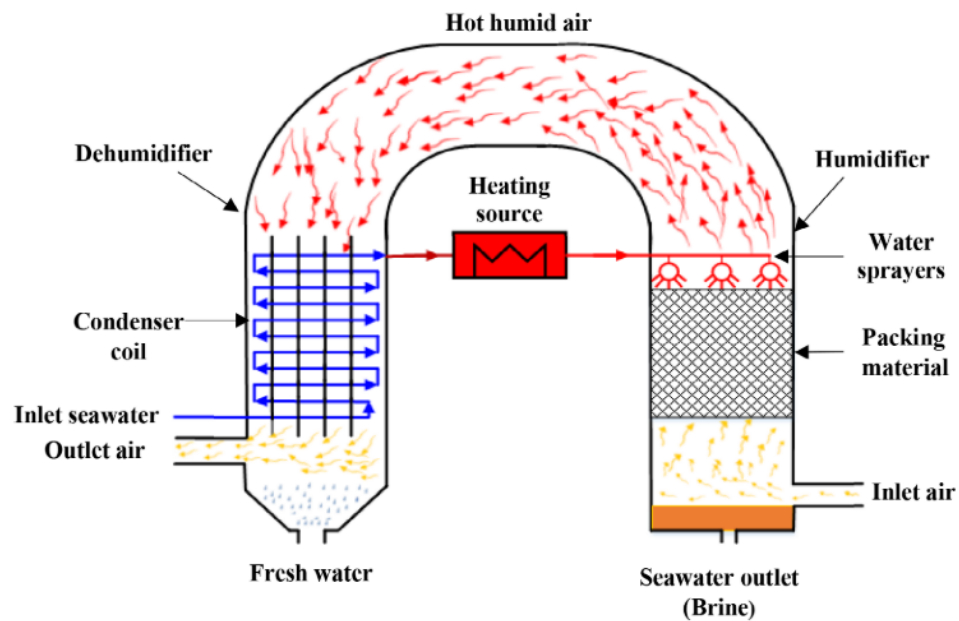


Fig. 1.4. Schematic diagram of the HDH thermal desalination system [37]

The purpose of the dehumidifier is to condense moisture from the air to obtain the required amount of fresh water. Dehumidifiers are mostly surface-type recuperative heat exchangers, typically with coil configurations or finned surfaces on the air side. The required heat exchange surface area of the dehumidifiers is determined based on the condition that all water vapor absorbed in the humidifier must be condensed from the air [38].

A humidifier is a contact heat and mass exchange device in which moisture from saline water evaporates into the air. The productivity of an HDH system is defined by the amount of water vapor absorbed by the air in the humidifier [38].

The advantages of HDH systems include high flexibility, low operating and maintenance costs, and suitability for remote areas. To improve the system efficiency, various types of renewable energy can be used [39, 40]. However, there are also disadvantages such as significant energy consumption and the need to establish an optimal water-to-air mass flow ratio for effective operation [40, 41].

An HDH technology has significant potential for implementation in remote and impoverished regions of China. The major limiting factor here is a high thermal energy demand. Therefore, improving the energy efficiency of HDH systems is considered one of the most promising directions for experimental research.

1.2.5. Combination of humidification-dehumidification and power cycles

Combined desalination and power systems (HDH-PWR), driven by low-temperature heat sources (renewables and waste heat), can play a crucial role in meeting the need for freshwater and energy, as well as in decreasing environmental pollutions [39]. To provide water and electricity, much attention has been paid to HDH-PWR systems due to their promising advantages compared to power systems integrated with RO units [40].

Heretofore, numerous theoretical studies have been conducted on HDH-PWR systems in which various configurations of HDH and power cycles were used. He et al. [41] studied an HDH-ORC system (Fig. 1.5) in which the hot brine from HDH cycle was used as the heat source of the organic rankine cycle (ORC). It was shown that the regulation of operating parameters of the HDH cycle i.e. the temperature of inlet water to the humidifier can maximize the performance of the cycle.

In a similar investigation [42] the possibility of using the condenser of ORC as the air heater of HDH cycle was studied from a thermodynamic standpoint (Fig. 1.6). It was concluded that a decrease in pinch temperature of the condenser of the ORC led to an

increase in freshwater productivity. In continuation of their study, He et al. [43] coupled an air-heated HDH cycle with an ORC (Fig. 1.7). In order to boost the performance of the ORC, the discharged brine entering the evaporator was reheated inside the boiler. It was illustrated that there was an optimum for a mass flow rate of saline water to air in which yield, GOR and efficiency reached the maximum level.

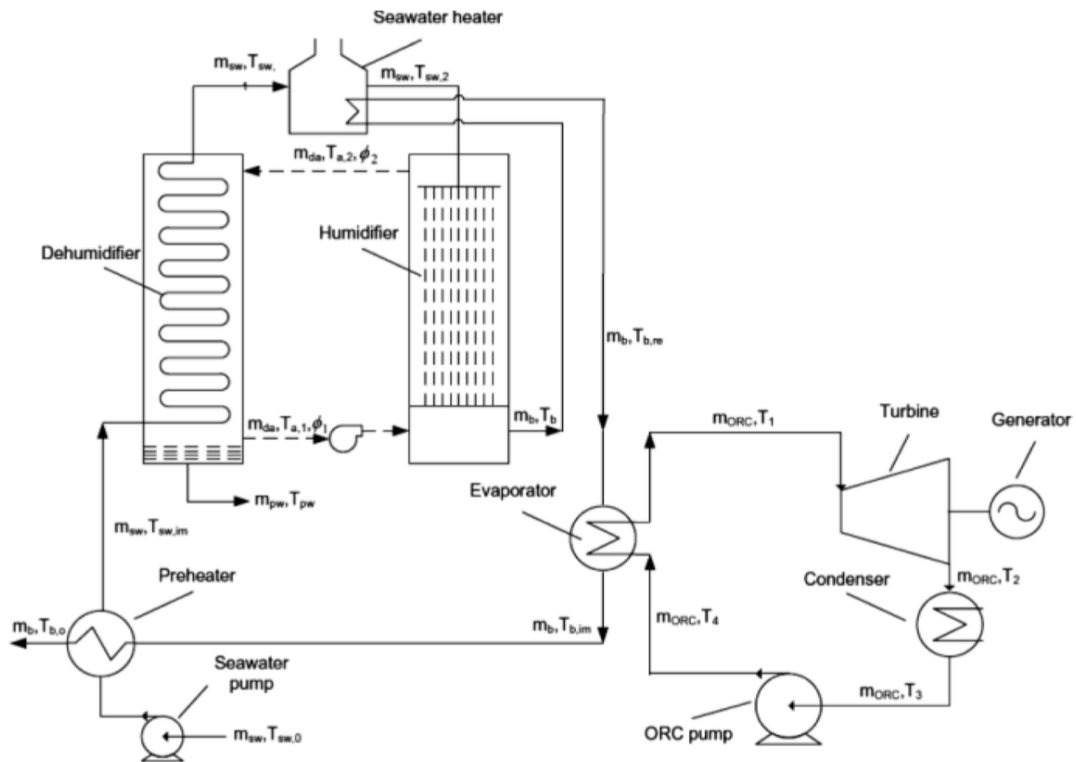


Fig.1.5. Use of brine as a heat source for ORC [41].

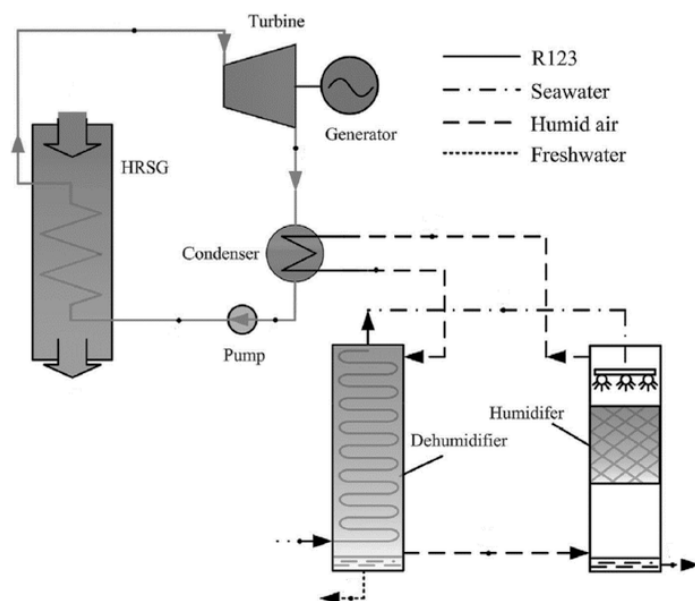


Fig. 1.6. Recovery of ORC condensing heat for operation of HDH units [42].

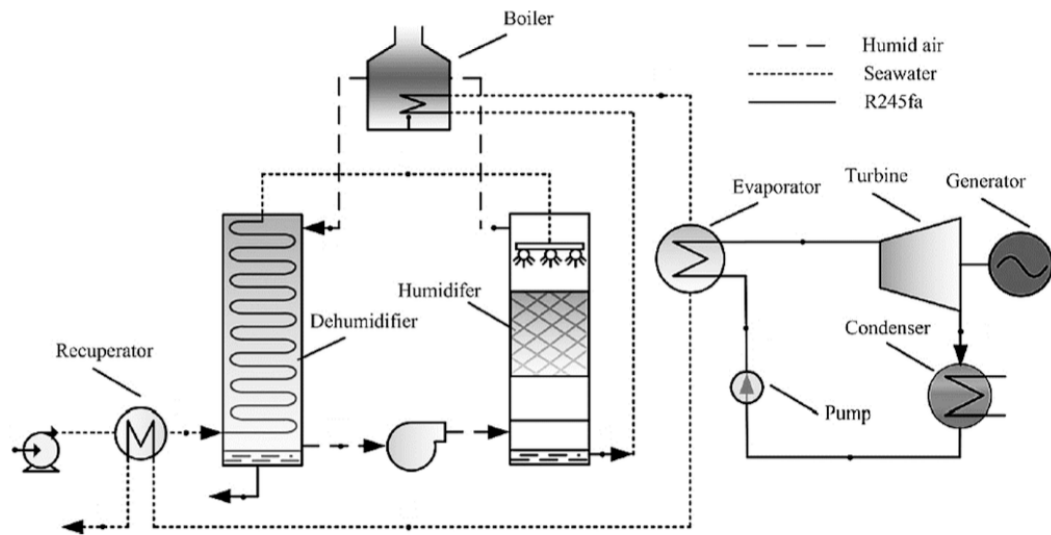


Fig. 1.7. Integration of an air-heated HDH cycle with ORC [43].

A comprehensive thermoeconomic investigation was conducted on the combination of a regenerative ORC with HDH system powered by geothermal water [44]. As it can be seen in Fig. 1.8, direct contact dehumidifier was used as opposed to conventional dehumidifiers in HDH cycles. The findings showed that the vapor generator of the ORC cycle exhibited the maximum irreversibility. Furthermore, increasing the evaporation temperature of the ORC was advantageous both for the thermodynamic performance and the relevant cost.

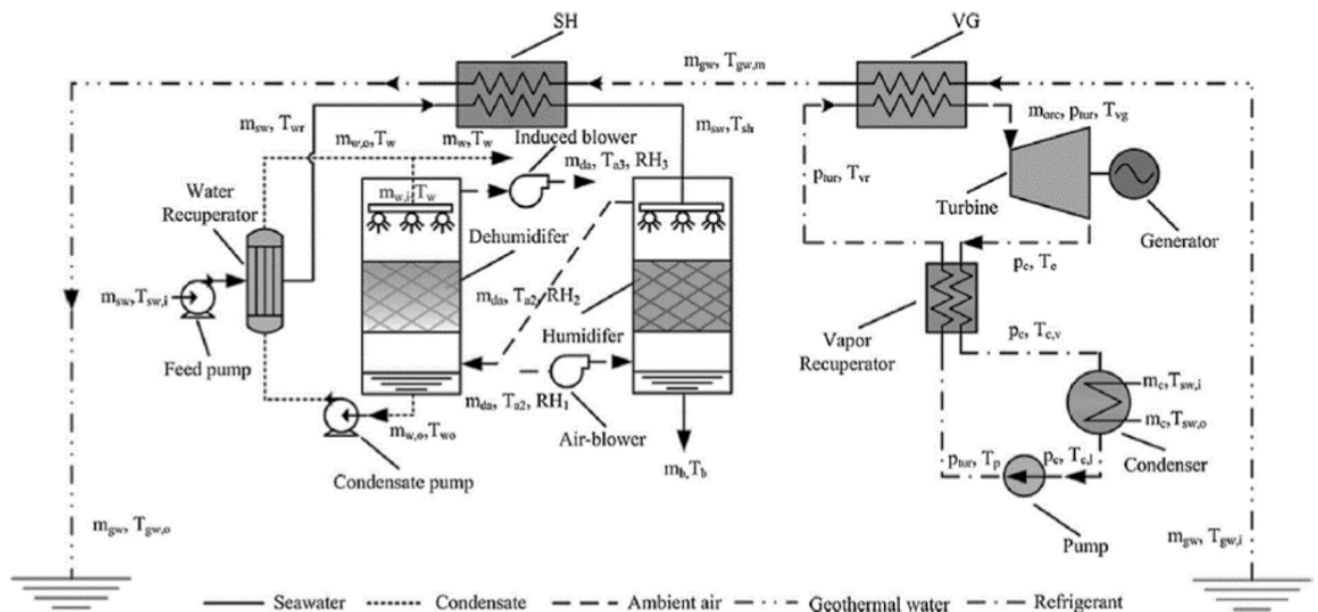


Fig. 1.8. Integration of ORC with direct contact dehumidification [44].

Several investigations conducted on HDH systems have reported widely varying values of freshwater yield, generated power and thermal efficiency of the combined systems. It can be seen that the diverse data reported by different authors have been hugely affected by various criteria, including configurations of HDH cycles, types of power cycles, heat source temperatures, etc. It is evident that the thermal efficiency of the power/water cycles varied hugely between 31.19% and 94.86% based on various working conditions. It is observed that the combination of air-heated HDH cycles with ORC, having the priority of air-heated HDH cycles to water-heated ones, led to the highest value of thermal efficiency [43]. However, this highest value of thermal efficiency obtained by [43] should be considered according to its heat source temperature, which is not reported in this investigation. It is worth mentioning that except for one mentioned study [40], cost of freshwater has not been investigated in other researches.

1.3. Overview of Contact Humidifier Designs

Various types of contact heat exchangers are used to humidify air in HDH systems, including spray towers, bubblers, and packed bed columns [45]. All these devices operate on the same principle. During the contact of water with air, water vapor diffuses into the air, increasing its humidity. The driving force for this diffusion process is the difference in concentration between the water-air interface and the water vapor in the air. This concentration difference depends on the vapor pressure at the water-air interface and the partial pressure of water vapor in the air.

Kebeel et al. [48] studied an HDH system with an open water loop and a closed air loop (Fig. 1.9). Saline water was heated in a solar collector before entering the humidifier, which was made of galvanized steel with a thickness of 1.5 mm, a rectangular cross-sectional area of $50 \times 80 \text{ cm}^2$, and a height of 200 cm. Two types of cellulose paper were used as packing material (Fig. 1.9). The first consisted of ten sheets, each measuring $80 \times 50 \times 10 \text{ cm}^3$, with openings in the shape of equilateral triangles with 5 mm sides. In the second variant, the side length of the triangle was 7 mm. The specific surface area of

the packing material was $2800 \text{ m}^2/\text{m}^3$, and the total heat and mass transfer surface area was 8 m^2 for the 5 mm cellulose and 6.8 m^2 for the 7 mm cellulose.

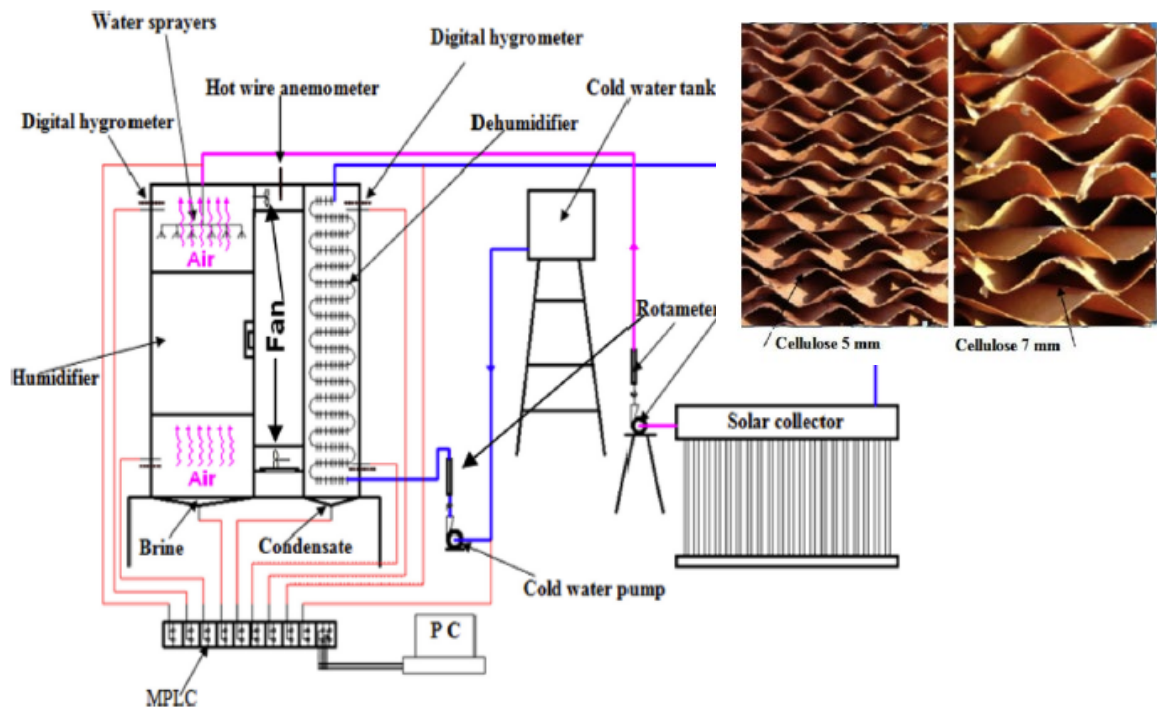


Fig. 1.9. Schematic of the HDH system with cellulose paper [48]

The authors [48] primarily focused on identifying the advantages of different types of packing materials and comparing natural (free) air circulation with three types of forced circulation (one fan at the bottom of the humidifier, one at the top, and two fans at the bottom and the top). Additionally, the researchers assessed the ratio of the cold water flow at the inlet of the dehumidifier to the hot water flow at the inlet of the humidifier (C/H). The saline water flow rate during the experiments varied from 1 to 4 kg/min. However, the airflow rate was not specified. The results [48] showed that maximum productivity was achieved when $C/H=2$. It was also found that forced air circulation with the fan placed at the inlet to the humidifier (bottom position) and 5 mm cellulose paper appeared to be the most effective. Under these conditions, the humidifier efficiency reached 99.5%.

It should be noted that the temperature of the saline water at the inlet of the humidifier ranged from 50 to 90 °C. This temperature range was not suitable for normal system operation due to salt precipitation and, consequently, fouling of the heat transfer surfaces in the collector, humidifier, and dehumidifier [49]. Furthermore, the study [48]

did not provide data on the heat consumed in the solar heater, making it impossible to determine the system's energy efficiency.

A distinctive feature of the study [50] was the use of biomass energy to heat water and air at the inlet of the desalination unit with an open air cycle (Fig. 1.10). The humidifier was a cylindrical chamber made of sheet steel with a cross-sectional area of 0.09 m^2 . The height of the container was 0.5 m at one end and 0.6 m at the other. The tilted top cover allowed the condensate to drain into the distillate collection tray. At a height of 0.12 m, a bubbling tube with a diameter of 0.039 m was installed for air supply.

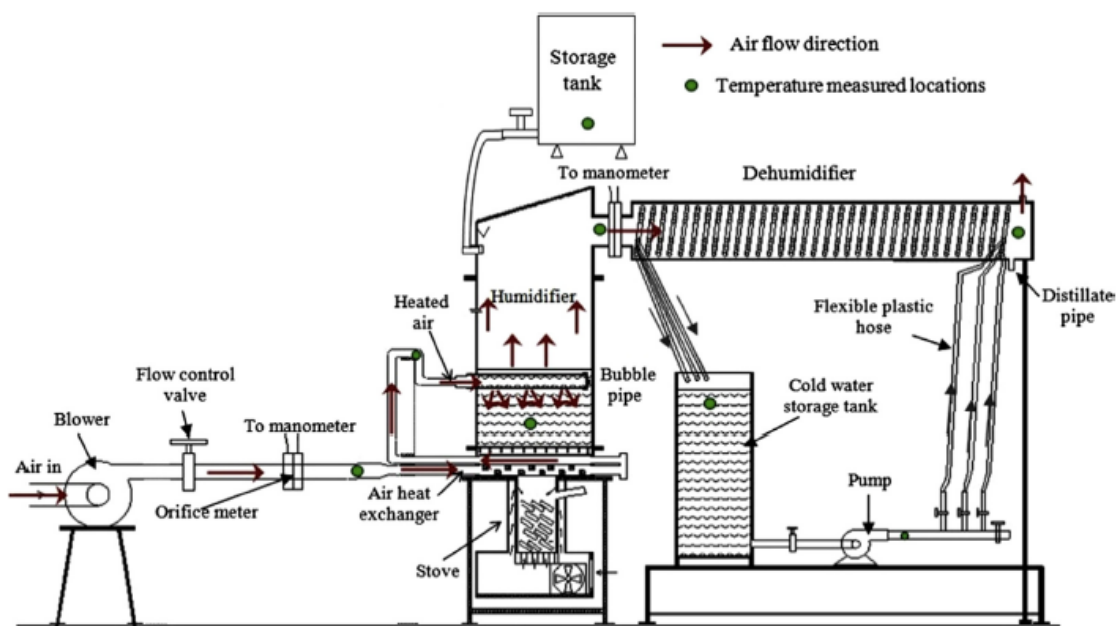


Fig. 1.10. Schematic of the desalination unit with a bubbling humidifier [50]

In the study [50], the influence of various parameters (diameter of the bubbling tube holes, water level in the humidifier, water temperature, and mass flow rates of air and cooling water) on the efficiency of the HDH system was investigated. Experiments were conducted with the air mass flow rate of 0.014-0.018 kg/s and the water mass flow rate of 0.025-0.0575 kg/s. Under these conditions, the system's productivity was 1.8-3.5 kg/h when using unheated (external) air and 4.25-6 kg/h when the air was preheated with flue gases. The authors [50] identified optimal values for the air flow rate (0.018 kg/s), cooling water flow rate (0.058 kg/s), water temperature (60 °C), water level in the humidifier (170 mm), and the diameter of the bubbling tube holes (1 mm). It is worth

noting the significant aerodynamic resistance of such a system (7.5-35 kPa) and its low energy efficiency (maximum GOR = 1). Noteworthy, the study [50] did not report the temperatures to which the air was heated before entering the humidifier.

In the study [51], a new design for compact and lightweight air humidifiers for HDH systems was proposed (Fig. 1.11). The heat exchanger consisted of a dense array of 24 vertically aligned strings along which the films of heated liquid could flow under the influence of gravity. A counterflow of air directly contacted the liquid film, transferring the resulting water vapor to the dehumidifier. This geometric configuration had a high phase interface-to-volume ratio, which was necessary for highly efficient heat and mass transfer processes and for reducing pressure drops in the gas phase. During the experiments, the saline water flow rate was 1.6 and 2.4 g/s, and the air flow rate varied from 1.5 to 12.5 kg/h. The inlet air temperature to the humidifier remained constant (22°C), while the saline water was heated to 80 and 90°C. Under these conditions, the authors [51] achieved evaporation rates from 5 to 12.5 kg/day. The efficiency of the string humidifier ranged from 1 to 4 Pa. It should be noted that energy performance indicator, specifically the gain output ratio (GOR), was not determined in the study [51], and the highest productivity with minimal pressure loss was obtained at a very high saline water temperature (90 °C) and the highest saline water flow rate (MR = 5,8).

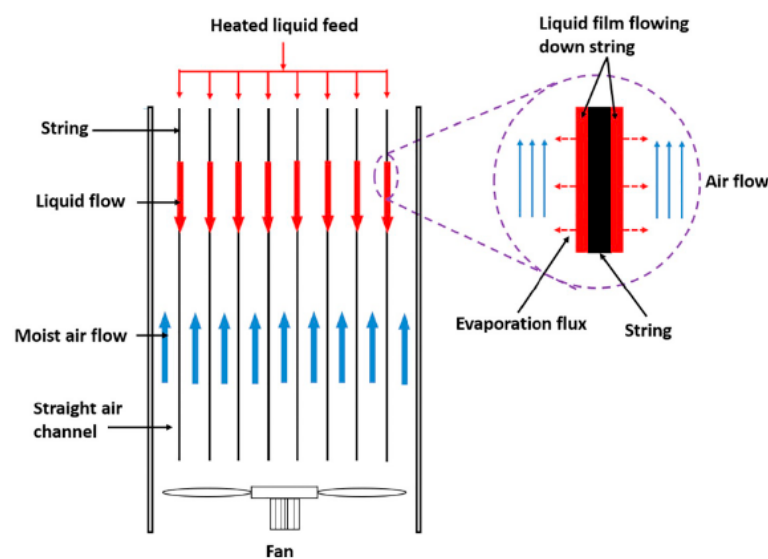


Fig. 1.11. Diagram of the HDH system with a string humidifier [51]

Eder and Preißinger [52] researched the operation of a bubbling cylindrical humidifier as part of an open-air and open-water HDH system. A distinctive feature of the setup was heating of the air at the outlet of the humidifier before it entered the dehumidifier (Fig. 1.12). However, the rationale for this design decision was not provided. The bubbler was made of stainless steel and acrylic glass, with a diameter of 140 mm. Water was supplied to the heat exchanger through a screen with holes of various diameters (ranging from 1 to 3 mm).

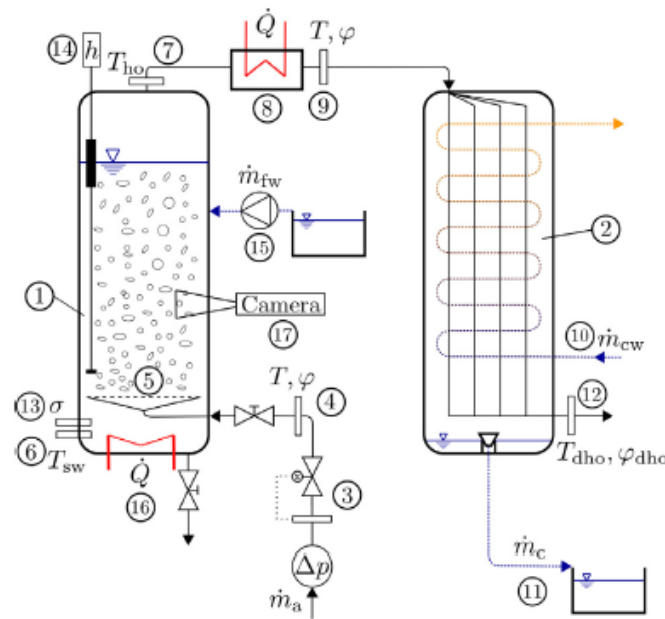


Fig. 1.12. Schematic of the HDH system with a bubbling column [52,53]

The productivity of this system ranged from 0.05 to 0.55 kg/h at a water temperature in the humidifier of 40-80°C, air velocity of 0.5-5 cm/s, and liquid level height of 60-378 mm. The authors determined the optimal parameters for the humidifier; however, GOR, MR, and RR values were not provided, nor were the necessary data for their calculation. It was established that the system's productivity increased with rising water temperature. In addition, the freshwater generation rate G_{fw} increased by approximately 29% with the rise in liquid level from 60 to 378 mm. These results were explained by the authors [52] as being due to enhanced heat and mass transfer in the first case and reduced heat losses from the water surface of the humidifier in the second.

In a subsequent study, Eder et al. [53] focused on investigating the heat and mass transfer coefficients between air and water in their bubbling column (Fig. 1.12). The authors [53] demonstrated that the air at the outlet of the humidifier reached a saturated state ($\phi = 100\%$) under various operating conditions. Unlike the previous study [52], the liquid level in the humidifier was less than 0.1 m. Significant changes in the humidifier efficiency were observed within this range. As a result, Eder et al. [53] proposed a diagram of the expected humidifier efficiency depending on air velocity and liquid height. However, one important parameter – aerodynamic pressure – was neither determined experimentally, nor were recommendations provided for its evaluation.

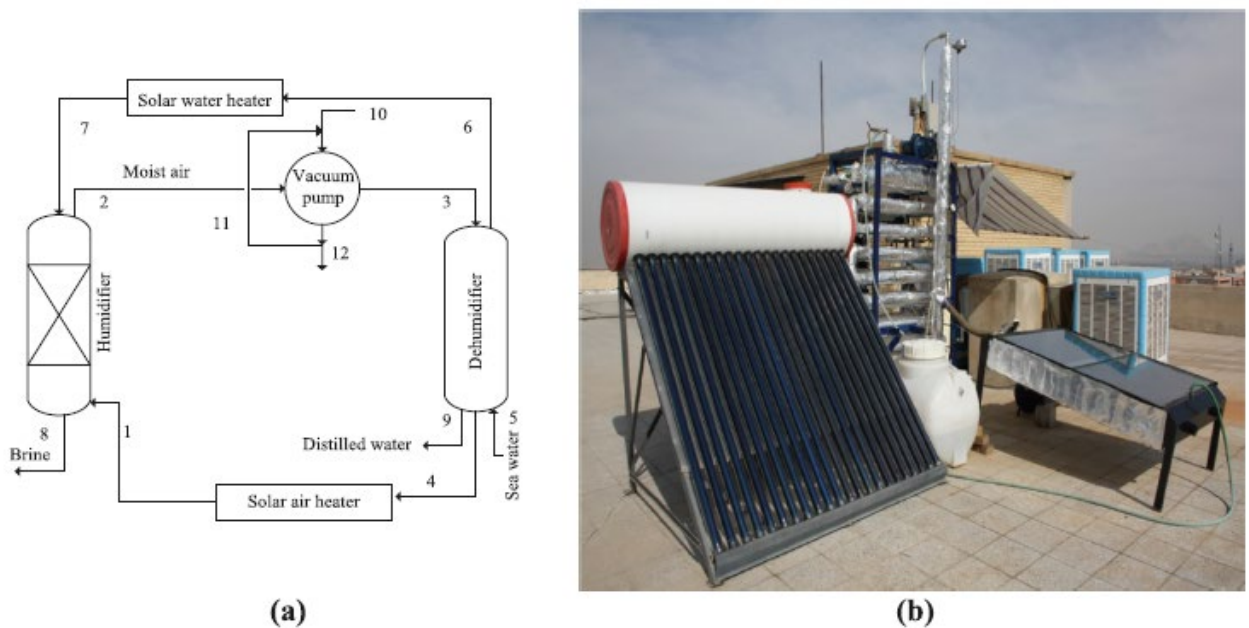


Fig. 1.13. Schematic (a) and photo (b) of vacuum thermal desalination [54, 55]

Rahimi-Ahar et al. [54, 55] investigated the humidification-dehumidification processes in the HDH system that is open to water and closed to air, with simultaneous water heating via solar collectors (see Fig. 1.13). The humidifier was a 2.5 m high tube with a diameter of 0.1 m and a packing material, the type and characteristics of which were not specified. An innovative aspect was the use of a vacuum pump to reduce pressure in the humidifier, which increased the air's moisture absorption capacity. The experiments were conducted under the following conditions: air and water temperatures at the humidifier inlet ranged from 35-75°C and 60-90°C, respectively; the air flow rate was 10 kg/h, and the water flow rate ranged from 10-30 kg/h; the water temperature at

the dehumidifier inlet was 10-35°C. Reducing the pressure in the humidifier from 90 kPa to 50 kPa significantly increased productivity, GOR, and other parameters. Under these conditions, the freshwater production rate reached 1.07 L/h per 1 m² of solar collector surface, and the maximum GOR was 3.43.

The study [56] focused on increasing the productivity of the HDH desalination system that used solar energy to heat water and operated with closed air and water cycles (see Fig.1.14). The bubble-type humidifier was made of galvanized sheet metal with a thickness of 3 mm, an area of 0.4×0.4 m², and a height of 0.15 m at the front and 0.35 m at the back. To reduce heat losses, the outer surface of the humidifier was insulated with a 0.02 m thick PVC coating. A distinctive feature of the study [56] was the use of heat pipes as humidifiers – this was the first time such a solution was applied. The system's productivity ranged from 0.22 to 0.83 kg/(h·m²) at air flow rates of 0.002-0.005 kg/s. Aref et al. [56] found that the higher the distillate flow rate (G_{fw}), the greater the overall efficiency and heat recovery in the humidifier. In addition, an increase in the air flow velocity led to a higher number of bubbles in the humidifier, resulting in an increased contact surface area between the air bubbles and the water. The maximum efficiency of the bubble-type humidifier was approximately 60%.

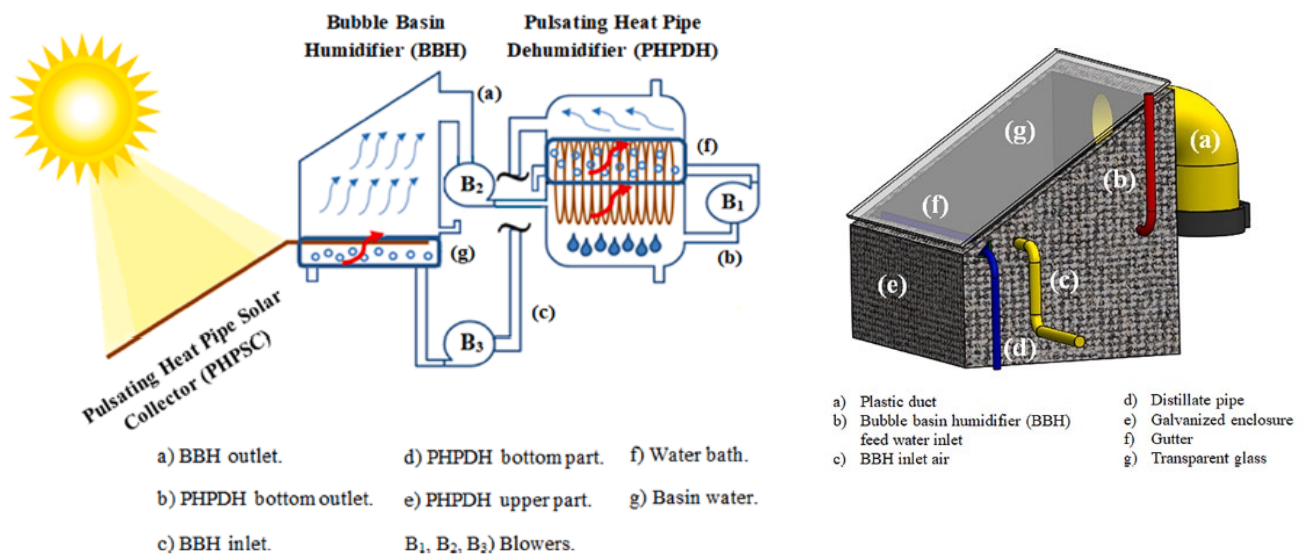


Fig. 1.14. Diagram of the HDH desalination system with a bubble-type humidifier [56]

An original design of the HDH desalination system was studied in works [57-59]. The experimental setup consisted of four main components: the saline water circuit, the humidifier, the hot air circuit, and the dehumidifier, as shown in Fig. 1.15.

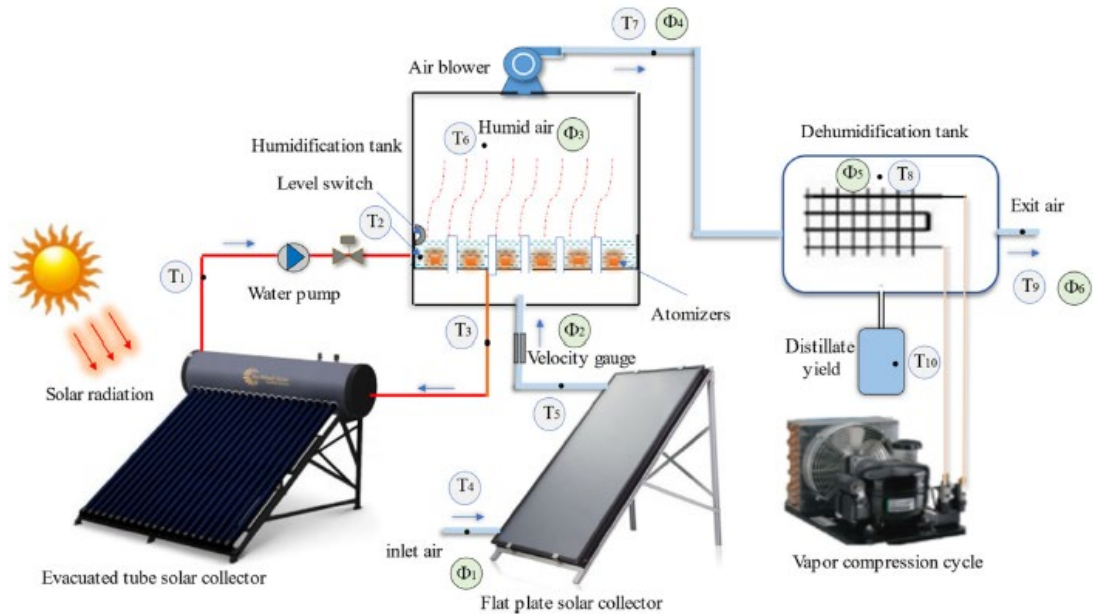


Fig. 1.15. Diagram of HDH desalination with an atypical humidifier [57]

The water circuit included a vacuum tube solar collector and a DC pump. The humidifier was made of galvanized steel with dimensions of 80×80×90 cm. A water tank measuring 77×77×15 cm was mounted inside the humidifier at a height of 20 cm from the base (Fig. 1.16).

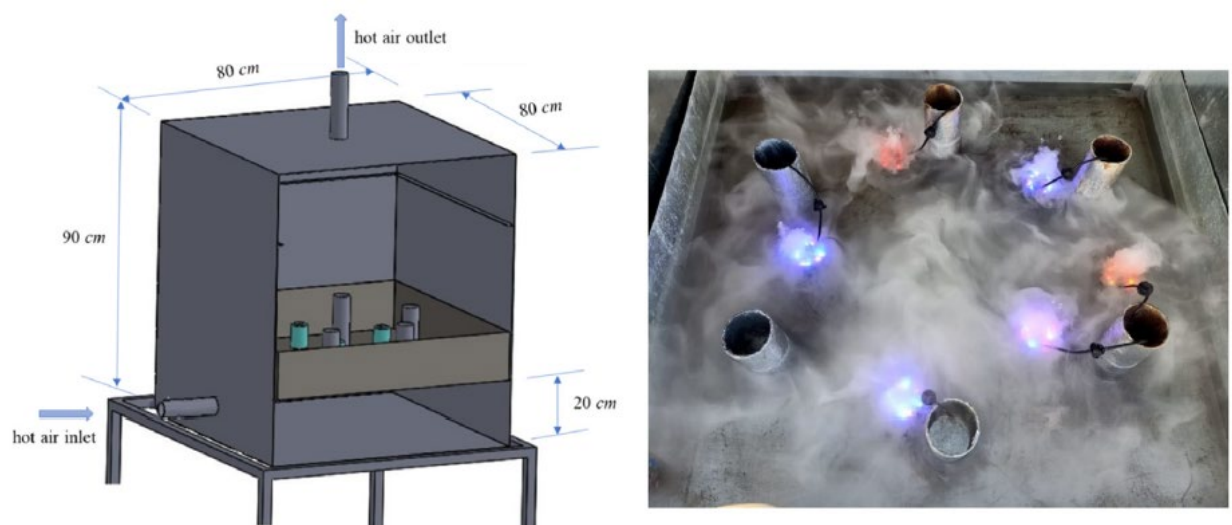


Fig. 1.16. Design of the humidification chamber from [57]

Six high-frequency ultrasonic atomizers, each 3 cm in height, were installed in the water tank to increase the humidity of the air. The experiments were conducted with two, four, and six atomizers activated. The water level in the tank was set at three different values: 1 cm, 2 cm, and 4 cm above the atomizers. The dehumidifier was a mini-chiller evaporator mounted inside the tank. The distilled water condensed on the evaporator was collected in a measuring container.

El-Said et al. [57] conducted their experiments under the following conditions: air flow rate of 0.009-0.017 kg/s; saline water flow rate of 0.008-0.03 kg/s. The authors [57] found that increasing the number of atomizers and lowering the water level in the humidifier positively influenced the daily distillate output. The system's productivity was significantly affected by the air flow rate. The highest hourly distillate production occurred at $G_a = 0.011$ kg/s, while the lowest was at 0.009 kg/s. The highest gain output ratio (GOR) of the system was approximately 1.54, and the maximum daily output was 7.74 kg.

A distinguishing feature of the study [58] was the use of porous tubes made of activated carbon in the humidifier instead of high-frequency ultrasonic atomizers. These tubes were mounted inside the humidifier between the two tanks measuring $77 \times 77 \times 15$ cm (Fig. 1.17). A total of 36 hollow carbon cylinders were installed, each 48 cm long, with an outer diameter of 55 mm and a wall thickness of 1.3 cm. The upper tanker served as a feeder, from which the water flowed downward by gravity along the tubes. The tank was filled to different water levels: 1, 2, and 3 cm, respectively. Experiments were conducted at $G_a = 0.0057$ -0.0173 kg/s and $G_w = 0.02$ -0.022 kg/s. The authors [58] observed that the system's productivity was primarily affected by the air flow rate. Distillate production increased by approximately 100%, 38.46%, 15.9%, and 34.5% at flow rates 0.0057, 0.0086, 0.0144, and 0.0173 kg/s, respectively. The optimal water level in the humidifier was 3 cm. The highest daily output was around 6.12 kg; the highest GOR was 1.24. It should be noted that using porous tubes for air humidification did not show advantages compared to the previously described setup with ultrasonic atomizers, as the energy performance indicators in the studies [57] and [58] were approximately at the same level.

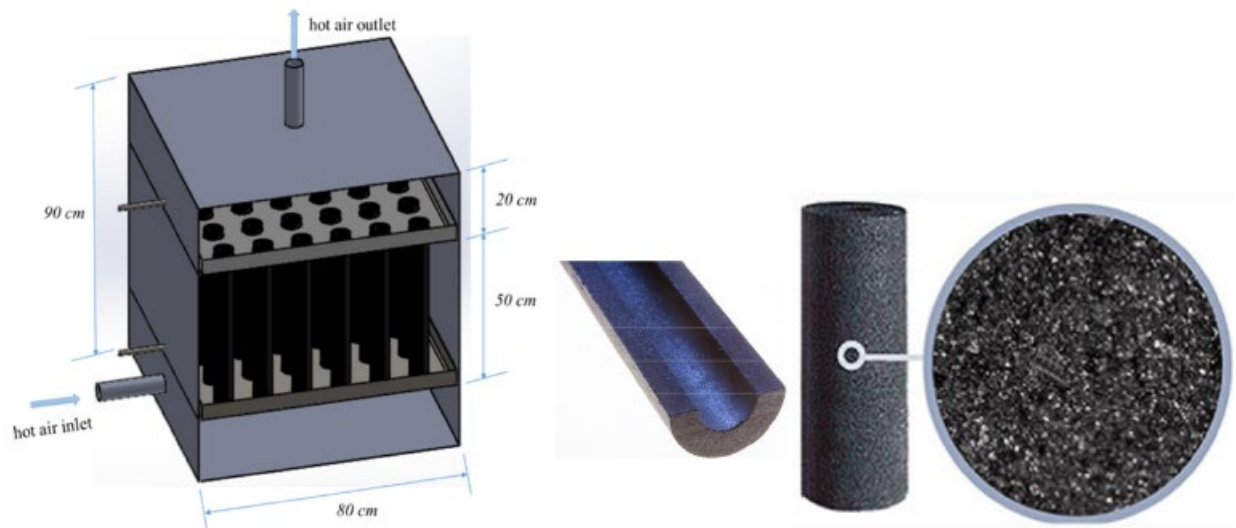


Fig. 1.17. Design of the humidifier with porous tubing [58]

The following study by Abdelaziz et al. [59] completely replicated the diagram, humidifier design, and the results of the setup performance from [57]. It can be noted that neither the use of a mini chiller for cooling the air in the dehumidifier nor the new humidifier designs offered significant advantages compared to other solutions. The water recovery ratio and the humidifier efficiency were among the lowest of all configurations reviewed.

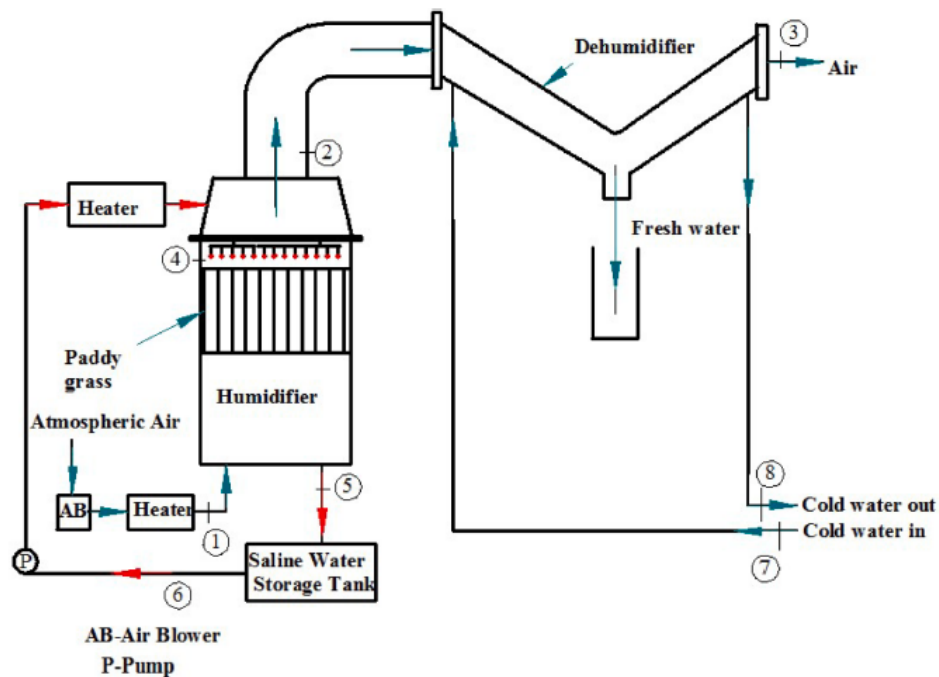


Fig. 1.18. Schematic of the HDH system with a separate cooling loop [60]

Thanaiah et al. [60] studied seawater desalination using artificial and biological packing materials. A distinctive feature of the proposed design was a separate water circuit for air cooling in the dehumidifier (Fig. 1.18). In this case, saline water circulated only in the humidifier and was heated at the inlet to the required temperature. The humidifier was made of mild steel with a square cross-section of 0.4×0.4 m and a height of 1m. To increase the contact area between air and water, hot water was sprayed using two sprinklers installed at the top of the humidifier. Each sprinkler consisted of 36 holes spaced 0.8 cm apart.

Experiments were conducted both without packing material and with polypropylene and paddy grass (Fig. 1.19). The latter consisted of 1,600 grass stems, each with a diameter of 0.005 m and a length of 0.4 m. The packing density of the paddy grass was $157.07 \text{ m}^2/\text{m}^3$ with a surface area of 10.05 m^2 . The maximum freshwater production rate was 0.39, 0.46, and 0.73 kg/h without packing, with polypropylene, and with paddy grass, respectively. The air flow rate ranged from 0.005 to 0.475 kg/s, while the water flow rate ranged from 0.01 to 0.0475 kg/s. Under these conditions, the GOR coefficient reached values of 0.1-0.28 (with no packing material), 0.15-0.4 (with polypropylene), and 0.3-0.65 (with paddy grass).



Fig. 1.19. Types of packing materials researched in [60]

In [61], the performance of a small-scale desalination unit was evaluated using hydrophobic plastic packing materials of various shapes (balls, saddles, and snowflakes) (Fig. 1.20). A mathematical model was developed to simulate the desalination process by calculating the temperature, productivity, and efficiency of the HDH system for each

packing material under steady-state conditions. The modeling results were compared with the experimental data.



Fig. 1.20. Hydrophobic plastic packing materials of various shapes [61]

The experimental setup described in [61] is shown in Figure 1.20. The dehumidifier consisted of five finned heat exchangers with aluminum fins and copper tubes connected in series. Another key component was a humidifier – a rectangular container made of polycarbonate with external dimensions $150 \times 150 \text{ mm}^2$ and a height of 320 mm. The humidifier was filled with packing material, and water was sprayed onto it using a sprinkler. Air circulated from the humidifier to the dehumidifier through a rectangular duct. To prevent heat loss to the environment, the entire system was insulated with polyurethane foam. The void fraction and specific geometric surface area of the balls were 92% and $280 \text{ m}^2/\text{m}^3$; saddles – 97% and $169 \text{ m}^2/\text{m}^3$; snowflakes – 97% and $138 \text{ m}^2/\text{m}^3$, respectively.

The experiments were conducted with the water flow rate of 6.12-18 kg/h and the air flow rate of 20.16-27.36 kg/h. The results did not show significant differences among the various shapes of packing materials. The distillate output, energy efficiency of the system, and aerodynamic resistance of the humidifier all fell within a similar range. It is also worth noting that in this setup, the water was cooled before being supplied to the dehumidifier, which allowed for lowering the air temperature and condensing more fresh water from the air. Therefore, it is surprising that the energy efficiency of this system was at the same level – or even lower – than that of other configurations without water cooling.

In [62], the performance of a solar HDH system using a centrifugal humidifier was experimentally analyzed. The experimental setup is shown in Figure 1.21. It consists of

five main components: a solar collector for heating seawater, a solar air heater, a centrifugal humidifier, a dehumidifier, and a measurement system for evaluating performance.

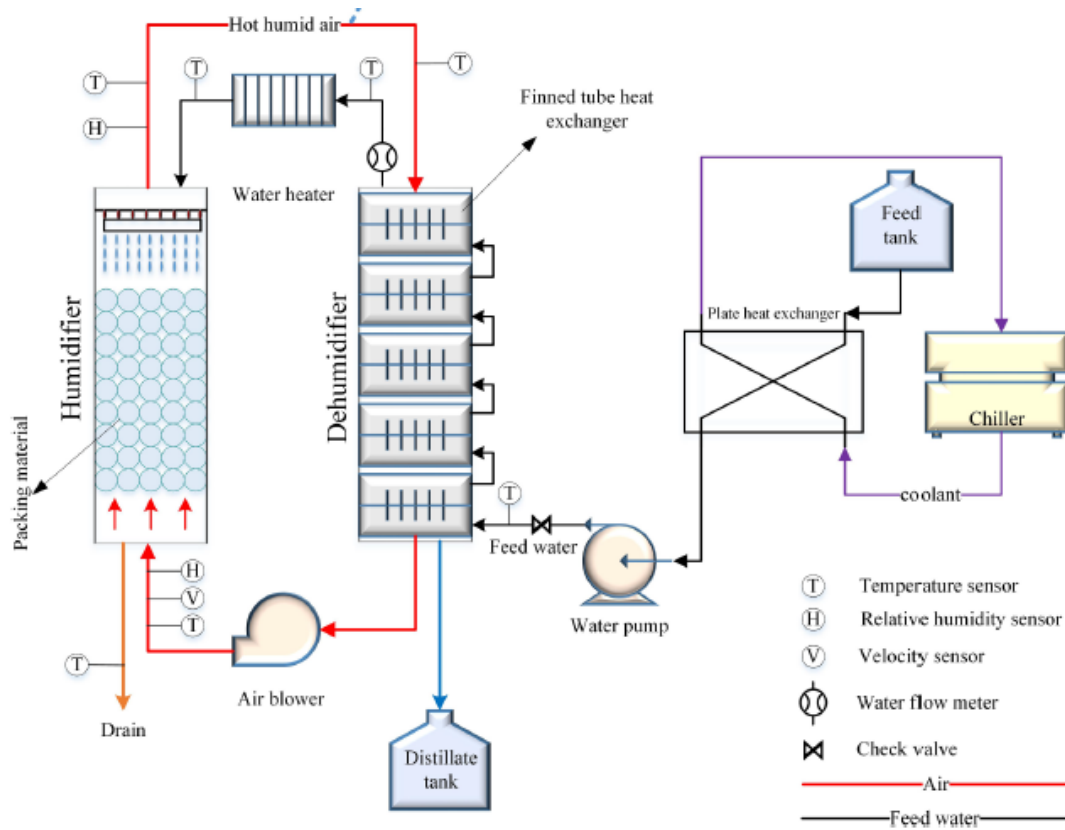


Fig. 1.21. Experimental setup from [61]

The air humidifier (Fig. 1.22) consisted of a rectangular casing and a centrifugal sprayer. The humidifier casing was made of galvanized steel and had dimensions of 0.60×0.60 m and a height of 1.0 m. The front side of the casing was made of plastic, allowing for observation of the air humidification process. The outer surface of the humidifier was insulated with 0.05 m-thick fiberglass. As shown in Figure 1.22, the sprayer consists of three main components: a drive mechanism, a hot water supply system, and a rotating sprinkler. The sprayer is driven by an AC motor and features multiple nozzles through which seawater is sprayed inside the humidifier. Seven different nozzle placement configurations were tested during the study.

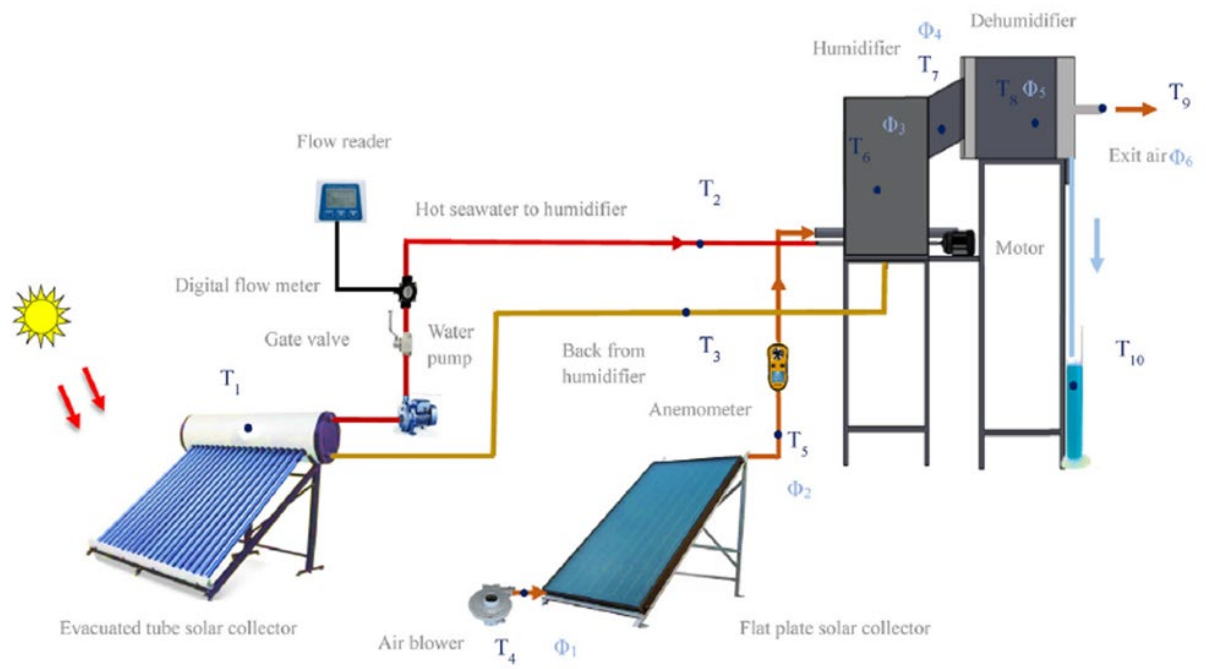


Fig. 1.21. Schematic diagram of the HDH system with a centrifugal humidifier [62]

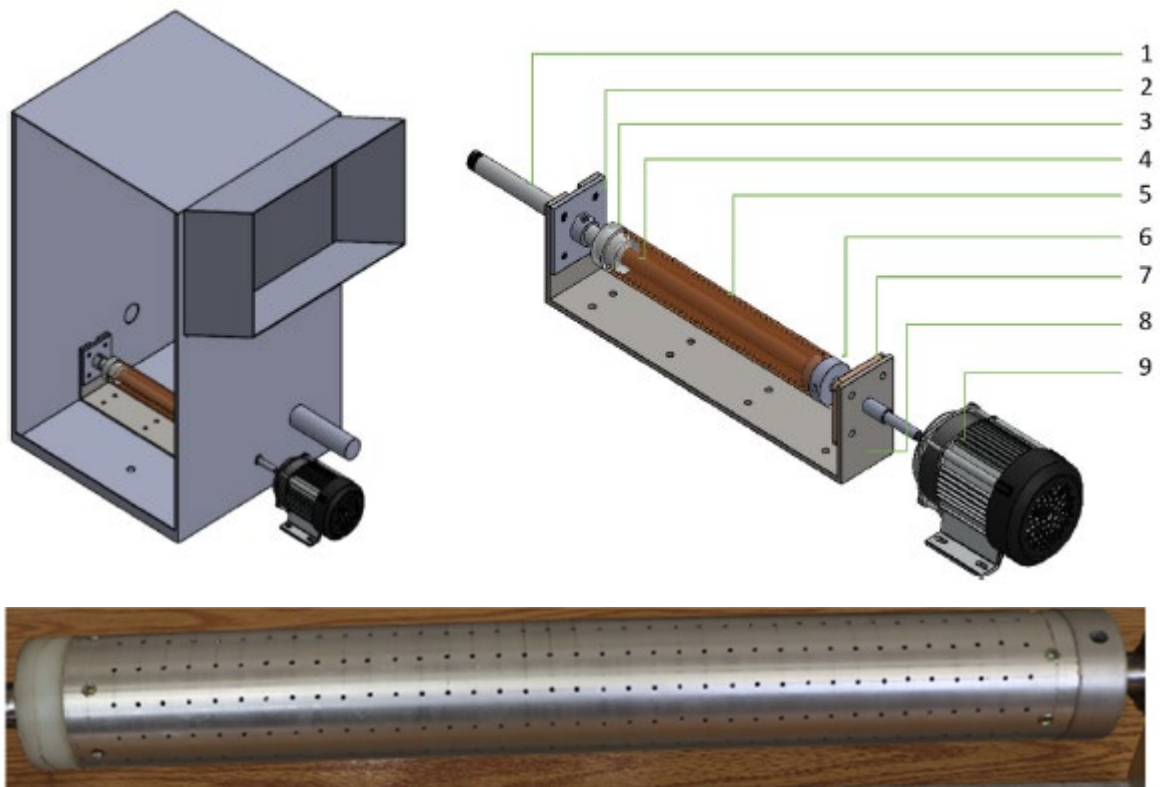


Fig. 1.22. Diagram of the rotary spraying humidifier [62]

The experiments were conducted at five different air flow rates (0.044, 0.038, 0.031, 0.025, and 0.019 kg/s) and five different water flow rates (0.051, 0.047, 0.039, 0.031, and 0.025 kg/s). The results [62] showed that a greater number of spray holes reduced performance, while increasing the sprinkler's rotational speed, by contrast, increased the distillate yield. The maximum distillate production (1.6 kg/s) and GOR (1.45) were achieved at the highest air (0.044 kg/s) and water (0.051 kg/s) flow rates. It should be noted that in [62], the authors did not report the air and water temperatures in the humidifier or determine the efficiency of the proposed humidifier design ε_{hum} , η_{hum} . At the same time, the overall system efficiency reached only 0.5. This low value can be attributed to the additional electrical energy consumption required to rotate the sprayer.

In [63], the characteristics of a closed-air and open-water version of the HDH cycle were experimentally investigated. The HDH system was built using a humidifier with a packing layer and finned tubular heat exchangers, which serve as the dehumidifier and are widely used in various industrial applications. Water heating took place after the dehumidifier, at the inlet to the humidifier.

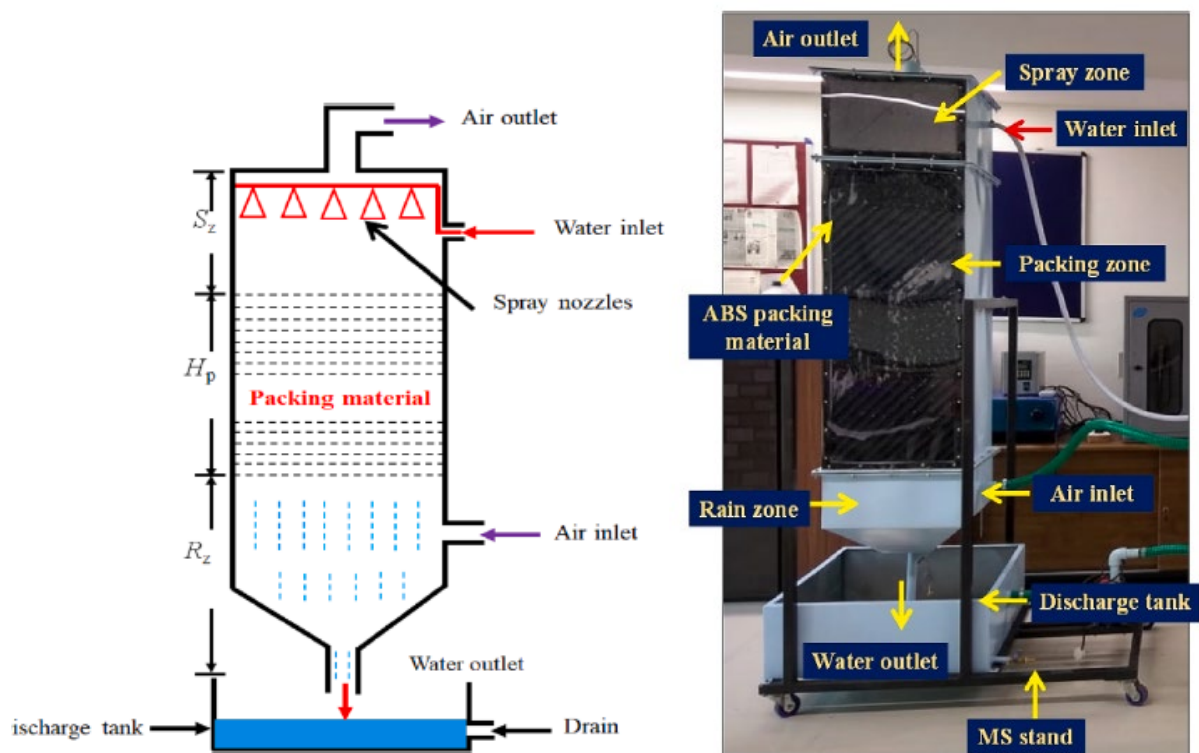


Fig. 1.23. Schematic and photo of the contact humidifier from [63]

The humidifier consists of three main sections and operates in a counterflow regime (i.e., air and water flow in opposite directions, see Fig. 1.23). The upper section, with a height of 0.3 m, is the zone where heated water is sprayed from all the nozzles. This is also where the hot, humid air exits the humidifier unit. The second section, located below the first, is 1.1 m high and is referred to as the packing material zone. It is filled with ABS plastic at a specific surface area of $226 \text{ m}^2/\text{m}^3$. The third section, 0.435 m in height, is situated at the bottom. Cold air is supplied to this section and moves upward as it interacts with the water trickling down from the packing material. Additionally, the concentrated brine is discharged into a drainage tank located at the very bottom of the humidifier.

Garg et al. [63] found that their system could produce approximately 125.5 liters of fresh water per day, operating at a water inlet temperature to the humidifier of only 61.7°C and achieving a mass flow rate ratio (MR) of 2.34. Under these operating conditions, the reported energy efficiencies of the humidifier and dehumidifier were approximately 0.75 and 0.80, respectively, while the coefficient of $\text{GOR} = 0.81$. The authors [63] noted that their system could be further improved and proposed integrating a solar-powered absorption heat transformer. The potential of this solution was evaluated analytically, without experimental validation.

Khan et al. [64] experimentally evaluated the performance of an HDH system with two bubble column humidifiers (Fig. 1.24).

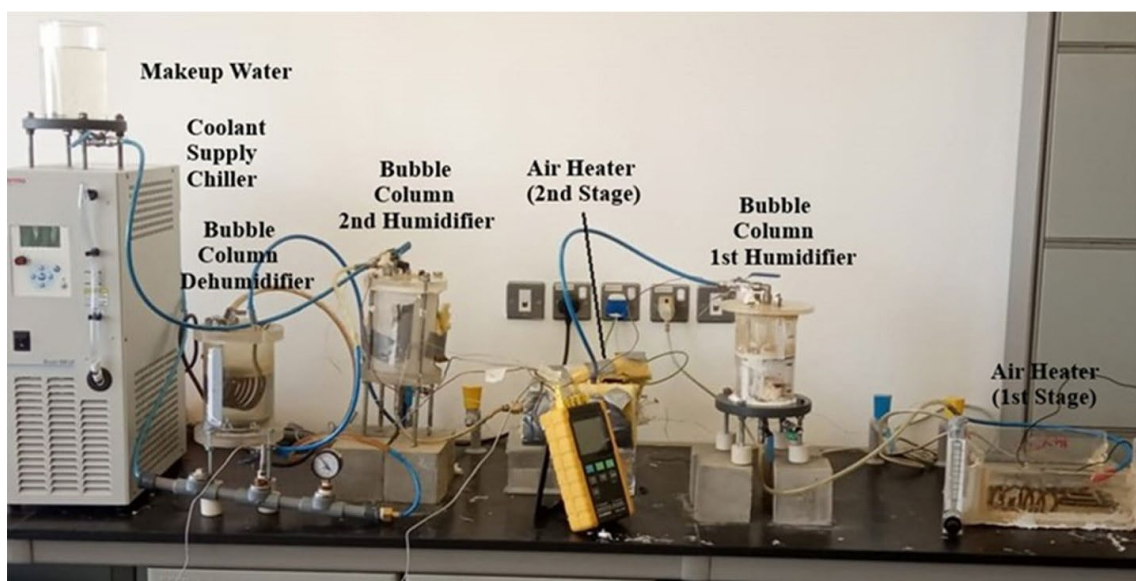


Fig. 1.24. Diagram of the desalination unit with two bubble column humidifiers [64]

The bubble columns were made of plexiglass in cylindrical form. The first humidifier had an internal diameter of 11.5 cm and a height of 16 cm. The perforated plate installed in the first humidifier consisted of 66 holes, each with a diameter of 5 mm. The second humidifier had a diameter of 13.5 cm, and its sprayer contained 60 holes with a diameter of 2 mm.

In [64], it was shown that increasing the air flow rate and temperature enhances the performance of the bubble column humidifiers. Additionally, the optimal parameters for maximum distillate production (0.3 kg/h) were identified: input power of 0.71 kW, air temperature of 140°C, air flow rate of 2.55 kg/h, and water levels in the first and second humidifiers of 3 cm and 6.5 cm, respectively.

Shaikh and Ismail [65] developed a solar collector-driven HDH system with a packed bed humidifier designed for Indian climatic conditions. As packing material, the authors [65] used 10 sheets of cellulose paper, each with a diameter of 0.4 m and a thickness of 10 cm (Fig. 1.25). The humidifier was made of plexiglass acrylic and had a cylindrical shape with a diameter of 0.4 m and a height of 1.75 m. To ensure uniform water distribution, an axial nozzle was installed 25 cm above the packing material. With the air flow rate of 10 kg/h and the feed water flow rate of 50 kg/h, the maximum productivity of the HDH system reached 6.5 kg per day, while the average thermodynamic efficiency of the humidifier was 0.62.

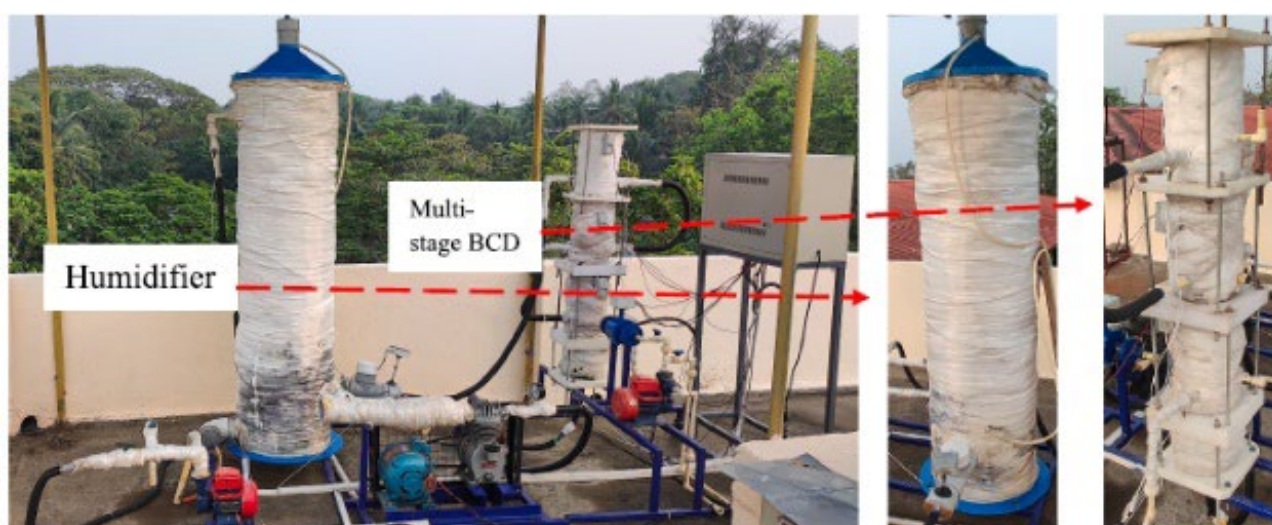


Fig. 1.25. General overview of the packed bed humidifier from [65]

According to the conducted review, the most common types of humidifiers in HDH systems are packed bed heat exchangers and bubble column humidifiers. Bubble column units [50, 52, 53, 56, 64] exhibit the highest thermodynamic efficiency; however, they are characterized by significant aerodynamic resistance (more than 10 kPa) and low volumetric productivity. This results in higher specific electricity consumption (SEC). Packed bed heat exchangers [48, 54, 55, 60, 61, 63, 65] demonstrate high efficiency due to their large heat and mass transfer surface area and relatively low air-side pressure losses (10...100 Pa). At the same time, they require a substantial flow of saline water ($MR > 1$). Additionally, saline water must be pumped through the humidifier at a high pressure to ensure effective spraying through the nozzles. Consequently, the pump power and energy consumption increase, which in turn raises the SEC value.

The advantages of a string-type humidifier [51] include low aerodynamic resistance and high heat and mass transfer efficiency. However, such performance is achieved at a water temperature of 90°C. Heating water to this temperature is impractical due to the potential for salt deposition within the HDH system components. Despite the structural complexity, other unconventional humidifiers [57-59, 62] demonstrate productivity comparable to packed bed units. Moreover, humidifiers equipped with ultrasonic atomizers [57, 59] and rotating attachments [62] consume more electricity.

Therefore, the lack of data on water and air pressure losses complicates the comprehensive analysis of existing humidifier designs and prevents the evaluation of their economic and exergy efficiency. This highlights the need for further research aimed at identifying optimal humidifier configurations.

1.4 Conclusions to Chapter 1, Research Aim and Objectives

1. Decentralized small-scale seawater desalination plays a significant role in alleviating water resource constraints in coastal regions and offshore islands, contributing to the sustainable development of China's economy and society.

2. The low-temperature small-scale thermal desalination technology based on humidification-dehumidification of air (HDH) offers distinct advantages for deployment

in remote and economically disadvantaged regions of China. However, the high thermal energy demand for freshwater production remains the primary limiting factor.

3. The performance of HDH systems is primarily determined by the amount of water vapor absorbed by air in the humidifier. Therefore, improving the efficiency of heat and mass transfer processes in humidifiers represents a promising direction for experimental research in HDH systems.

4. The most common types of humidifiers used in HDH systems are packed bed heat exchangers and bubble column humidifiers. However, these devices exhibit high specific electricity consumption, which increases the cost of freshwater and reinforces dependence on energy resources (particularly electricity).

5. The lack of data on water and air pressure losses hinders a comprehensive analysis of humidifiers and prevents the evaluation of their economic and exergy efficiency. This gap necessitates further research aimed at identifying optimal humidifier configurations.

Based on the analysis of the existing scientific studies on heat transfer during filmwise condensation of moving vapor inside smooth horizontal tubes, **the aim of this research** was formulated as follows: to enhance the performance of contact humidifiers in thermal desalination systems in order to reduce both thermal and electrical energy consumption for freshwater production in remote and economically disadvantaged areas of China.

In accordance with this aim, the following **main research objectives** were defined:

1. To experimentally investigate the hydrodynamics and heat and mass transfer processes during air humidification in a tube contact heat exchanger under typical HDH system operating conditions.

2. Based on the analysis of the experimental results, determine the geometric dimensions of the unit and the air and water flow rates required to achieve the maximum performance and energy efficiency of the HDH system.

3. To develop a calculation methodology for the tube contact heat exchanger when used as a humidifier in a thermal desalination system.

4. To compare the performance of the tube film heat exchanger with other commonly used humidifier designs.

CHAPTER 2. EXPERIMENTAL SETUP AND METHODOLOGY FOR STUDYING THE AIR HUMIDIFICATION PROCESS

2.1. Design and Layout of the Experimental Setup

To carry out the experimental investigation, an experimental setup was designed and constructed at the Department of Heat and Alternative Power Engineering of the Educational and Scientific Institute of Nuclear and Thermal Energy at the National Technical University of Ukraine “Igor Sikorsky Kyiv Polytechnic Institute”. The general view and schematic diagram of the setup are shown in Figures 2.1 and 2.2, respectively.

The setup includes an open-air circuit and a closed-water circuit. The system’s main parts are the humidifier (10), the water heater (6), the pump (8), the fan (15), and the control and measurement system used to monitor key parameters.

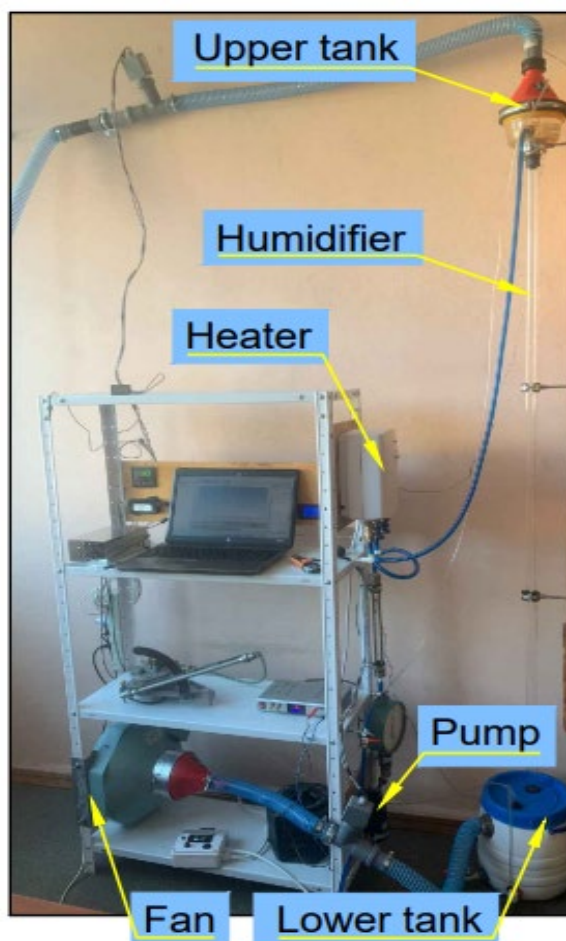


Fig. 2.1. Photograph of the experimental setup

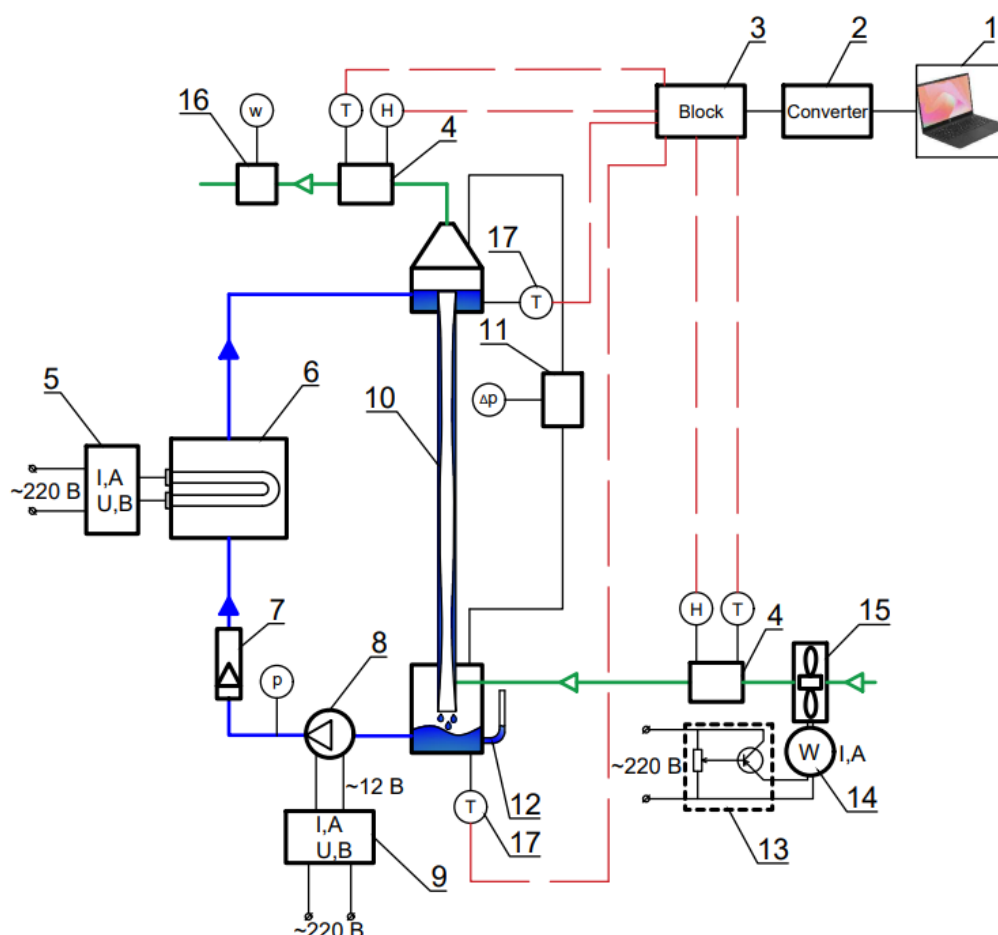


Fig. 7. Schematic of the experimental setup:

1 – laptop; 2 – RS485/USB interface converter;
 3 – eight-channel meter; 4 – air relative humidity and temperature converter; 5 – power regulator with a temperature sensor; 6 – flow-through water heater; 7 – rotameter; 8 – diaphragm pump; 9 – laboratory power supply unit with smooth adjustment of output parameters using current and voltage potentiometers with 0-24 V, 6 A with a digital electronic meter; 10 – experimental humidifier; 11 – inclined tube micromanometer; 12 – piezometer; 13 – adjustable laboratory autotransformer; 14 – digital multifunction AC meter; 15 – fan; 16 – anemometer, 17 – Pt1000 thermocouple.

A humidifier (10) is a transparent acrylic tube, 2 meters long, with an internal diameter of 26 mm, fixed between two reservoirs.

An electrical heater (6) (Fig. 2.3) was designed to preheat the water before it is fed into the humidifier. The compact casing of the unit contains a flow-through chamber and two heating elements (tubular electric heaters) with a rated power of 1 kW and 2 kW, respectively. The water temperature at the humidifier inlet is regulated by adjusting the power supplied to the heating elements via a controller (5).



Fig. 2.3. General view of the heater

A diaphragm water pump (8) (Fig. 2.4) provides circulation of water within the setup's water circuit and has the following technical specifications:

- maximum flow rate – 6 L/min;
- operating voltage – 9...14.4 V;
- operating current – up to 6 A;
- power – 72 W;
- operating pressure – up to 0.9 MPa;
- operating temperature – 0...100°C;
- weight – 0.6 kg.

Water flow was regulated using a laboratory power supply unit (9) by smoothly adjusting the operating voltage and current.



Fig. 2.4. General view of the diaphragm pump

The duct fan (15) supplied ambient air to the experimental setup and had the following technical specifications:

- maximum airflow rate – $437 \text{ m}^3/\text{h}$;
- operating voltage – up to 230 V, operating current – 0.31 A;
- power – 70 W;
- weight – 3 kg.



Fig. 2.5. General view of the fan

The airflow rate is regulated using a laboratory autotransformer (13). The set values of voltage and current are displayed on a digital meter (14).

The following instruments are integrated into the experimental setup to measure the required parameters. A rotameter (7) is connected to the water circuit to measure the volumetric flow rate of water. The pump head is measured with a pressure gauge. The air velocity at the outlet of the humidifier is measured by an anemometer (16). The total air pressure losses in the humidifier are recorded using a micromanometer (11). The water temperatures at the inlet and outlet of the humidifier are measured with the thermocouples (17). The air temperature and relative humidity at the inlet and outlet of the humidifier are measured using digital sensors (4). All temperature and humidity values are transmitted in real time to a software application on a laptop (1) via a data acquisition system consisting of an eight-channel meter (3) and an interface converter (2). The atmospheric pressure is measured using a barometer. The specifications and measurement errors of all instruments are presented in Table 2.1.

Table 2.1. Specifications of Measuring Instruments

<i>Instrument</i>	<i>Parameter</i>	<i>Range</i>	<i>Accuracy</i>
<i>1</i>	<i>2</i>	<i>3</i>	<i>4</i>
Digital Converter DVT-303	Air temperature	-35–80°C	±0.4°C
	Air relative humidity	0–100%	±3%
Thermocouple Pt1000	Water temperature	-40–270°C	±(0.3+0.005t)°C
Rotameter RM-0.1	Water flow rate	up to 100 L/h	±2.5 L/h
Rotameter RM-0.04	Water flow rate	up to 40 L/h	±1 L/h
Anemometer testo 410i	Air velocity	0.4–30 m/s	±0.2 m/s ±2% of the measured value
Micromanometer	Air pressure drop	up to 600 Pa	± 3 Pa
Manometer	Pump head	up to 60 kPa	±0.6 kPa
Barometer	Atmospheric pressure	80-106 kPa	±0.2 kPa

Continuation of Table 2.1

1	2	3	4
Single-channel output DC power supply	Heater power	0–30 A 50–300 V	± 0.01 A ± 0.1 V
Digital multi-function meter	Fan power	up to 4.5 kW	$\pm 1\%$
	Pump power		
Vernier caliper	Tube diameter	150 mm	± 0.1 mm
Measuring tape	Tube height	up to 3 m	± 1.3 mm

All instruments used during the experiments were accompanied by a technical passport and/or a valid calibration certificate. Therefore, the measurement accuracy of each instrument was known. The complete list of measurement accuracies is presented in Table 2.1 in the format $\pm X$, where X denotes the corresponding measured value.

2.2. Research Methodology and Measurement Error Assessment

The installation works as follows. The upper reservoir (Fig. 2.6.a) is filled with water using a pump (8), ensuring an even flow of the water film along the inner surface of the humidifier (10). From the tube, the water flows into the lower reservoir (Fig. 2.6.b). The water level in the lower reservoir is monitored using the piezometer (12). From the lower reservoir, the water is pumped back to the upper reservoir by the diaphragm pump (8), completing a full cycle. Smooth regulation of water flow is achieved using the laboratory power supply (9) by adjusting the input current (0 - 6 A) and voltage (0–24 V). A flow-through electric heater (6) is used to raise the water temperature to the desired value. The required heating power is set via a controller (5).

Ambient air is supplied to the humidifier (10) by the fan (15) through the lower reservoir, flows upward through the system, and exits into the environment from the upper reservoir. During the heat and mass transfer between the air and the falling water film inside the tube, the air becomes warmer and more humid, while the water is being cooled. The airflow rate in the humidifier is controlled by adjusting the input voltage to the fan

within the range of 0-220 V using an autotransformer (13). The fan's power consumption is measured using a digital multifunction AC meter (13). The range of changing operation conditions is shown in Table 2.2.



Fig. 2.6. Design of the upper (a) and lower (b) reservoirs

Table 2.2. Measured Experimental Variables

<i>Parameter</i>	<i>Range</i>	<i>Standard Uncertainty</i>
Air velocity in the tube	3.3-15.2 m/s	3.3-8 %
Mass flow rate of water	10-80 kg/h	3.1-9.6 %
Air pressure drop in the humidifier	19-324 Pa	1-15 %
Air temperature at the humidifier inlet	24-29°C	2%
Air humidity at the humidifier inlet	≈65%	4.7%
Air temperature at the humidifier outlet	27-48°C	2%
Air humidity at the humidifier outlet	≈98%	3%
Water temperature at the humidifier inlet	28-59°C	1.3%
Water temperature at the humidifier outlet	25-42°C	1.4%
Pump head	22.3 kPa	2.7%
Power consumption of the fan	≈7.5 W	1%
Power consumption of the pump	≈1.5 W	1%

The maximum relative measurement errors are calculated using the following formula:

$$\delta X = \frac{\Delta X}{X} 100\%, \quad (2.1)$$

where: X is the minimum value of the measured variable (Table 2.2).

ΔX is an absolute measurement error determined according to the accuracy of the measuring instrument used for each variable (Table 2.1).

The air velocity inside the tubes is measured using a compact vane anemometer Testo 410i (Fig. 2.7). The device is positioned at the air inlet zone of the tube and aligned with the direction of air flow (Fig. 2.2). The inlet zone diameter corresponds to the humidifier's internal diameter (26 mm). The anemometer is equipped with a wireless Bluetooth module and operates in conjunction with a mobile application, which allows for convenient real-time data collection, processing, and analysis.

Measurements are conducted in a continuous mode for a specific time interval (at least one minute for each trial). The data collected during a one-minute interval for one of the variable sets is shown in Figure 2.8.



Fig. 2.7. General view of the anemometer Testo 410i

As shown in Figure 2.8, the amplitude of air velocity fluctuations is minimal, indicating a stable airflow. Minor variations in velocity are caused by an interaction

between the air and the liquid film inside the humidifier, which leads to the formation of local vortices and turbulent zones. Therefore, in each experiment, the average air velocity over a one-minute measurement interval is used for further calculations. For the measurements presented in Figure 2.8, an average air velocity is 2.3 m/s.

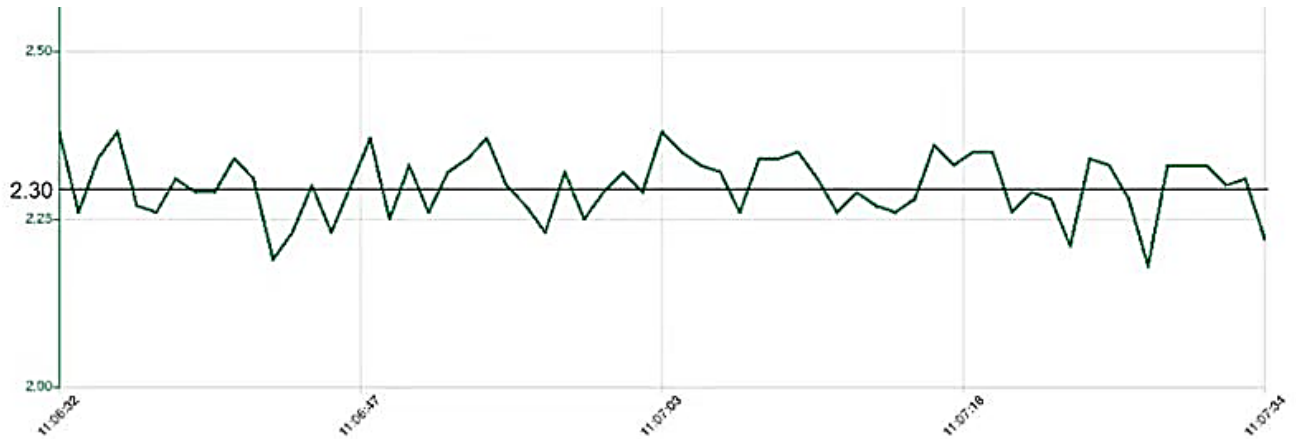


Fig. 2.8. Variation of air velocity in the humidifier over a one-minute measurement interval

To measure the water temperature, Pt1000 resistance temperature detectors manufactured by REGMIK [66] (Fig. 2.9.a) are used. DVT-303 digital humidity and temperature sensors (Fig. 2.9.b) are applied to determine the air parameters at the inlet and outlet of the humidifier.



Fig. 2.9. General view of the Pt1000 (a) and DVT-303 (b) sensors

The digital signals from the Pt1000 and DVT-303 sensors are transmitted to the eight-channel measuring device (18) (Fig. 2.10) for monitoring and displaying the measured values on a built-in digital indicator.



Fig. 2.10. General view of the eight-channel converter (I8)

To collect, store, and visualize temperature and humidity data in real time, the digital signals from the measuring device (18) are transmitted to a laptop screen using an RS-485/USB interface converter (Fig. 2.11) and the “REGMIK Data Acquisition System” software (Fig. 2.12). The temperature and humidity measurements are taken at 5-second intervals throughout the entire duration of the study.



Fig. 2.11. General view of the eight-channel converter (I8)

Changes in the water and air temperatures during the study are shown in Figures 2.13 and 2.14, respectively. Overall, the duration of a single experiment can be divided into three distinct stages.

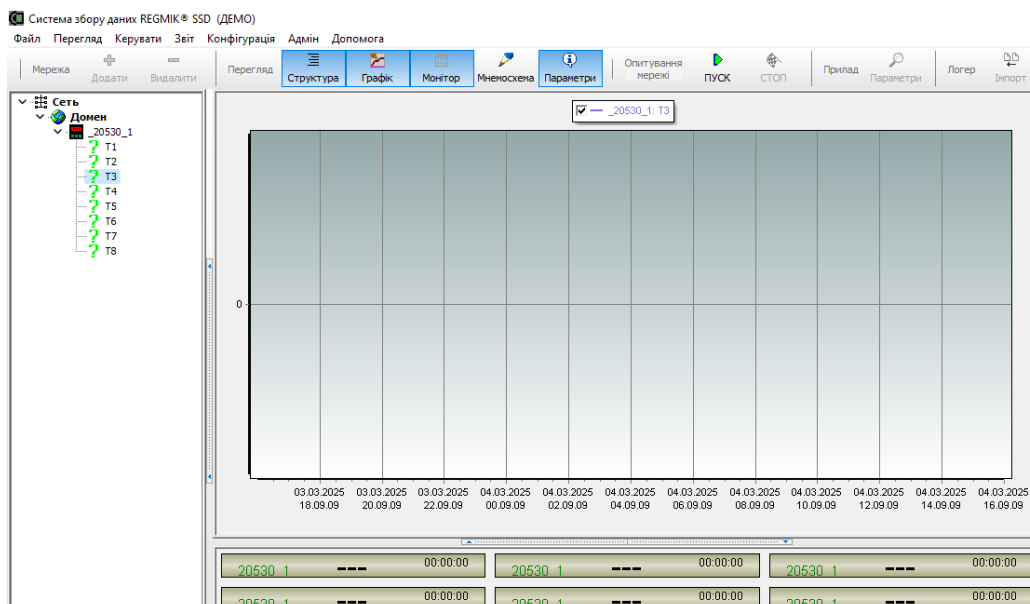


Fig. 2.12. Screenshot of the “REGMIK Data Acquisition System” software

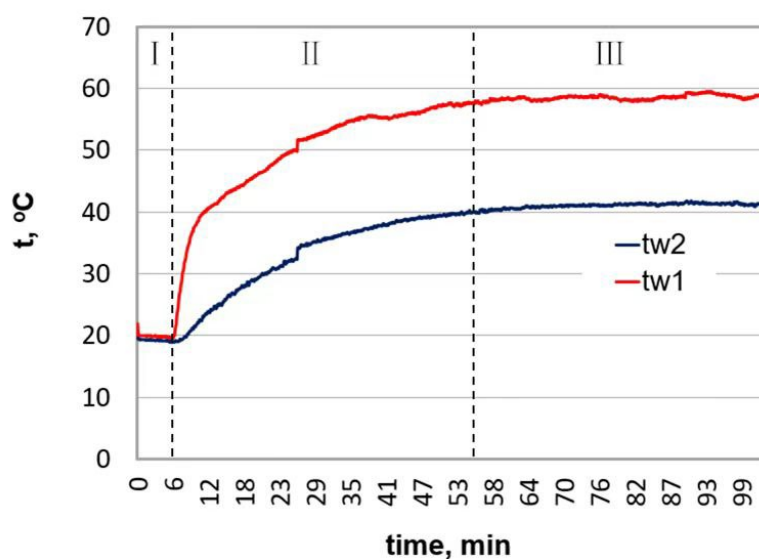


Fig. 2.13. Changes in water temperature during the experiment

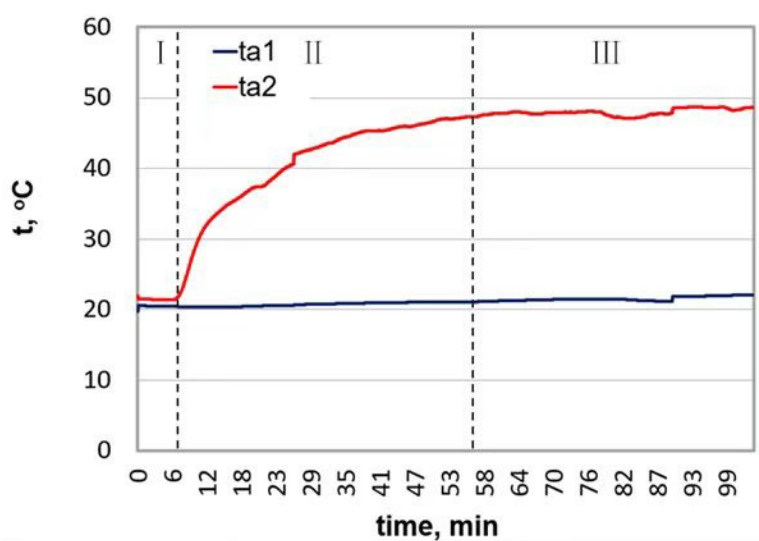


Fig. 2.14. Changes in air temperature during the experiment

After starting the setup, adjusting the required flow rates of air and water, and activating the measurement system, all four temperature values corresponded to the ambient laboratory air temperature (t_{a1}). During this initial period (Stage I), there were no significant temperature changes.

Following the activation of the heater and the setting of its required power, Stage II – heating – started. Within the first 30 minutes of the experiment, the temperatures t_{w1} , t_{w2} , and t_{a1} increased sharply. Subsequently, their growth slowed and continued until relatively constant values were reached. The stabilization of the temperatures t_{w1} , t_{w2} , and t_{a1} occurred approximately one hour after the start of the experiment, indicating that the system had approached thermal equilibrium.

Stage III lasted 30-40 minutes. A key feature of this period was the stability of the temperature regime without abrupt fluctuations. For further calculations of the energy performance of the humidifier, the average temperature and humidity values recorded during Stage III were used.

2.3. Experimental Data Processing Methodology

2.3.1. Heat Balance of the Humidifier

Data reduction of the measured results can be summarized in the following procedures. The thermodynamic properties of water and humid air are determined using the CoolProp library [67].

The mass flow rate of the air at the inlet to the experimental setup is determined using the following formula:

$$m_a = 0.25\pi w_a d^2 \rho_{a,in}. \quad (2.2)$$

The liquid velocity is calculated by the formula:

$$w_w = \frac{4m_w}{\pi d^2 \rho_{w,in}}. \quad (2.3)$$

The heat balance of the experimental humidifier is calculated as follows:

$$Q_a = Q_w. \quad (2.4)$$

The heat supplied to the water in the flow-through heater is determined in the following way:

$$Q_w = m_w c_{p,w,in} t_{w,in} - (m_w - \Delta\omega) c_{p,w,out} t_{w,out}. \quad (2.5)$$

where $\Delta\omega$ is the humidifier's performance (mass flow rate of humidity transferred from hot water to air):

$$\Delta\omega = m_a(\omega_{out} - \omega_{in}). \quad (2.6)$$

The total heat transferred to the air in the humidifier is calculated as follows:

$$Q_a = (m_a + \Delta\omega) h_{a,out} - m_a h_{a,in}. \quad (2.7)$$

The heat transferred to the air in the humidifier consists of two types:

$$Q_a = Q_a^{evap} + Q_a^{con}. \quad (2.8)$$

where Q_a^{evap} is latent heat (the heat transferred during the evaporation of water vapor into the air):

$$Q_a^{evap} = \Delta\omega h_{vl}. \quad (2.9)$$

Q_a^{con} is sensible heat (the heat transferred through convective heat exchange):

$$Q_a^{con} = m_a c_{p,a} (t_{a,out} - t_{a,in}). \quad (2.10)$$

As shown in Figure 2.15, approximately 87% of the heat is transferred from water to air through moisture evaporation, while about 13% is transferred via convective heat exchange. The distribution between latent and sensible heat in the thermal balance is consistent with the results of numerical modeling [68, 69] and experimental studies [70].

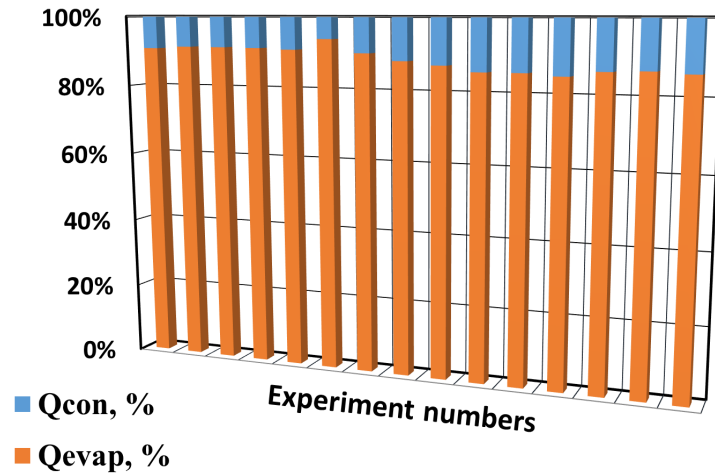


Fig. 2.15. Balance of latent and sensible heat in the humidifier during the experimental studies

The ratio of the thermal balance between water and air for all experiments is presented in Figure 2.16. The solid line represents a theoretical finding. The closer the square is to the black line, the smaller the deviation between Q_a and Q_w . It can be seen that the maximum discrepancy between Q_a and Q_w does not exceed 8%.

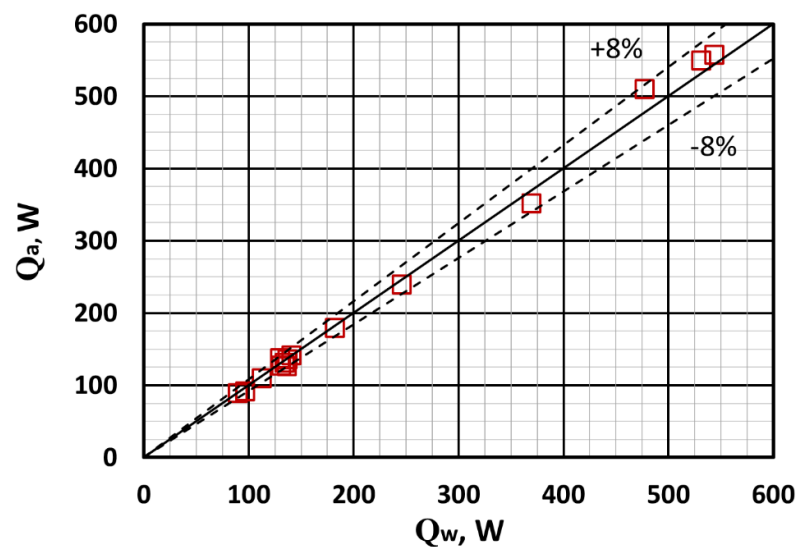


Fig. 2.16. The ratio between Q_a and Q_w in the humidifier during the experimental studies

The mean absolute deviation, mean deviation, and root mean square deviation of the thermal balance based on water and air in the humidifier are determined using the corresponding formulas:

$$e_A = \frac{1}{n} \sum 100 \left| \frac{Q_a - Q_w}{Q_w} \right| \quad (2.11)$$

$$e_R = \frac{1}{n} \sum 100 \left(\frac{Q_a - Q_w}{Q_w} \right) \quad (2.12)$$

$$\sigma_N = \left[\frac{1}{n-1} \sum (e - e_R)^2 \right]^{0.5} \quad (2.13)$$

where $e = 100 \left(\frac{Q_a - Q_w}{Q_w} \right)$, n is the number of calculated points.

The percentage of the calculated points that matched the experimental values within a $\pm 8\%$ margin of error was also determined. The results of the thermal balance error analysis for the humidifier are summarized in Table 2.3.

Table 2.3. Errors in the Thermal Balance of the Humidifier

<i>Error Type</i>	<i>Value</i>
mean absolute deviation e_A , %	3.5
mean deviation e_R , %	1.1
root mean square deviation σ_N , %	6.5
number of points within $\pm 8\%$ error margin	15 or 100%

An analysis of Figure 2.16 and the data presented in Table 2.1 indicates that the humidifier's thermal balance between water and air was determined with sufficient accuracy.

2.3.2. Determination of the Humidifier's Energy Performance Indicators

The electric energy consumption by the pump and the fan required to transfer 1 kg of moisture to the air in the humidifier is calculated as follows:

$$SEC = (N_{fan} + N_{pump}) / \Delta\omega. \quad (2.14)$$

The evaporation rate per unit humidifier volume is calculated using the formula

$$ER = \Delta\omega / V_{hum}, \quad (2.15)$$

$$V_{hum} = 0.25\pi d^2 l. \quad (2.16)$$

The humidifier's performance is calculated by the formula:

$$\eta_{hum} = (\eta_{hum,a}; \eta_{hum,w}), \quad (2.17)$$

where $\eta_{hum,a}$ is the efficiency of the humidifier on the air side:

$$\eta_{hum,a} = \frac{h_{a,out} - h_{a,in}}{h_{a,out}^{id} - h_{a,in}}; \quad (2.18)$$

where $\eta_{hum,w}$ is the efficiency of the humidifier on the water side:

$$\eta_{hum,w} = \frac{h_{w,in} - h_{w,out}}{h_{w,in} - h_{w,out}^{id}}. \quad (2.19)$$

Formulas (2.18) and (2.19) $h_{a,out}^{id}$ demonstrate ideal enthalpy of air at the humidifier outlet (assuming full saturation, $\varphi_{out}=100\%$ and $t_{a,out} = t_{w,in}$). $h_{w,out}^{id}$ shows ideal enthalpy of water at the humidifier outlet (assuming $t_{w,out} = t_{a,in}$).

The exergetic efficiency of the humidifier is calculated using the following formula [71]:

$$\varepsilon_{hum} = \frac{E_P}{E_F} = \frac{E_{a,out} + E_{a,in}}{E_{w,in} + E_{w,out}}, \quad (2.20)$$

where E_P is the exergy of the “product”, or an increase in exergy between the inlet and outlet for the continuous air flow;

E_F is the exergy of the “fuel”, or a decrease in exergy between the inlet and outlet for the water flow;

$E_{a,in}$ 0 W is the exergy of the incoming air (equal to the exergy of the ambient environment).

The values of the other components in the formula (2.19) are determined using the equations provided in [72].

The exergy of moist air at the outlet of the humidifier is calculated as follows:

$$E_{a,out} = m_a \left\{ (c_{p,a,out} + \omega_{a,out} c_{p,v}) \cdot \left(T_{a,out} - T_{a,in} - T_{a,in} \ln \frac{T_{a,out}}{T_{a,in}} \right) + R_a T_{a,in} \left[\left(1 + \frac{M_a}{M_v} \omega_{a,out} \right) \ln \frac{1 + \frac{M_a}{M_v} \omega_{a,in}}{1 + \frac{M_a}{M_v} \omega_{a,out}} + \frac{M_a}{M_v} \omega_{a,out} \ln \frac{\omega_{a,out}}{\omega_{a,in}} \right] \right\}. \quad (2.21)$$

The exergy of water at the humidifier inlet is calculated using the following equation:

$$E_{w,in} = m_w \left[h_{w,in} - h_{w,out}^{id} - T_{a,in} (s_{w,in} - s_w^{id}) - R_v T_{a,in} \ln \frac{\varphi_{a,in}}{100} \right]. \quad (2.22)$$

where s_w^{id} is the entropy of the “dead state”, J/(kg·K).

The exergy of water at the humidifier outlet is calculated as follows:

$$E_{w,out} = (m_w - \Delta\omega) \times \left[h_{w,out} - h_{w,out}^{id} - T_{a,in}(s_{w,out} - s_w^{id}) - R_v T_{a,in} \ln \frac{\varphi_{a,in}}{100} \right]. \quad (2.23)$$

2.4. Assessment of Calculation Uncertainty

In this study, the uncertainty of the calculated values was assessed using the method described by Holman et al. [73]. It is assumed that the result of calculating the parameter R is a function of independent variables (measured quantities) $X_1, X_2, X_3, \dots, X_n$, i.e.,

$$R = f(X_1, X_2, X_3, \dots, X_n). \quad (2.24)$$

In this case, the absolute uncertainty of the parameter R can be calculated using the following equation:

$$\Delta R = \sqrt{\left(\frac{\partial R}{\partial X_1} \Delta_1 \right)^2 + \left(\frac{\partial R}{\partial X_2} \Delta_2 \right)^2 + \left(\frac{\partial R}{\partial X_3} \Delta_3 \right)^2 + \dots + \left(\frac{\partial R}{\partial X_n} \Delta_n \right)^2}, \quad (2.25)$$

where $\Delta_1, \Delta_2, \Delta_3, \dots, \Delta_n$ are absolute uncertainties of independent variables $X_1, X_2, X_3, \dots, X_n$.

In the case where the result of the function R is determined as the product of the corresponding measured quantities, i.e.,

$$R = X_1^{a_1} X_2^{a_2} \dots X_n^{a_n}, \quad (2.26)$$

the partial derivatives in equation (2.25) can be written as follows:

$$\frac{\partial R}{\partial X_i} = X_1^{a_1} X_2^{a_2} (a_i X_i^{a_i-1}) \dots X_n^{a_n}. \quad (2.27)$$

After dividing equation (2.26) by equation (2.27), we obtain:

$$\frac{1}{R} \frac{\partial R}{\partial X_i} = \frac{a_i}{X_i}. \quad (2.28)$$

Substituting equation (2.28) into equation (2.25), we obtain the computational formula for determining the uncertainty of the calculated value:

$$\frac{\Delta R}{R} = \sqrt{\sum \left(\frac{a_i \Delta_i}{X_i} \right)^2}. \quad (2.29)$$

In the case where the result of function (2.24) is determined as the sum of the respective primary variables, i.e.,

$$R = a_1 X_1 + a_2 X_2 + \dots + a_n X_n, \quad (2.30)$$

the partial derivatives in equation (2.25) have the following form:

$$\frac{\partial R}{\partial X_i} = a_i. \quad (2.31)$$

After substituting the value of the partial derivative from equation (2.31) into formula (2.25), we obtain the following result:

$$\Delta R = \sqrt{\sum (a_i \Delta_i)^2}. \quad (2.32)$$

Equations (2.29) and (2.32) should be used together if the calculation formula (2.24) includes the measured variables related by a complex relationship (product and sum).

As an example, we determine the uncertainty of the calculation formula (2.2), which is used to find the mass flow rate of air at the inlet to the experimental setup:

$$m_a = 0.25\pi w_a d^2 \rho_{a,in}.$$

The values of the air mass flow rate are determined for the series of experiments conducted to evaluate the energy performance of the tube humidifier (Section. 3.3):

$$m_a = 0.25 \cdot 3.14 \cdot 5.02 \cdot 0.026^2 \cdot 1.182 = 0.0032 \text{ kg/s} \text{ а́о } 11.3 \text{ kg/h}.$$

The calculation formula (2.2) includes two values that are determined experimentally:

$$m_a = f(w_a, d). \quad (2.33)$$

The partial derivatives of the two respective functions are found:

$$\frac{\partial m_a}{\partial w_a} = 0.25\pi d^2 \rho_{a,in}, \quad (2.34)$$

$$\frac{\partial m_a}{\partial w_a} = 0.25 \cdot 3.14 \cdot 0.026^2 \cdot 1.182 = 6.27 \cdot 10^{-4}.$$

$$\frac{\partial m_a}{\partial d} = 0.5\pi d \rho_{a,in}, \quad (2.35)$$

$$\frac{\partial m_a}{\partial d} = 0.5 \cdot 3.14 \cdot 0.026 \cdot 1.182 = 0.048.$$

According to the formula (2.25), the absolute uncertainty of the air mass flow rate calculation is determined as follows:

$$\Delta m_a = \sqrt{\left(\frac{\partial m_a}{\partial w_a} \Delta w_a\right)^2 + \left(\frac{\partial m_a}{\partial d} \Delta d\right)^2}, \quad (2.36)$$

$$\Delta m_a = \sqrt{(6.27 \cdot 10^{-4} \cdot 0.3)^2 + (0.048 \cdot 10^{-4})^2} = 1.88 \cdot 10^{-4} \text{ kg/s} \text{ a} \pm 0.7 \text{ kg/h}$$

The relative uncertainty of the air mass flow rate calculation is determined using the equation (2.1):

$$\delta m_a = \frac{\Delta m_a}{m_a} 100\%, \quad (2.37)$$

$$\delta m_a = \frac{0.7}{11.3} 100\% = 6\%.$$

Similarly, the uncertainties of all calculated parameters are determined. The final results are presented in Table 2.4. Thus, it was established that the maximum combined uncertainty of the experimental results amounts to $\pm 11\%$.

Table 2.4. Standard uncertainties of the calculated parameters.

<i>Parameter</i>	<i>Range</i>	<i>Uncertainty</i>
m_a	7.4-35 kg/h	3.4-7.1 %
w_w	0.005-0.042 m/s	3.2-9.6 %
$\Delta \omega$	114-682 gr/h	6.9%
Q_a	89-557 W	11%
Q_w	90-554 W	8.4%
SEC	0.013-0.081 kWh/kg	7.1%
ER	108-642 kg/(m ³ h)	6.9%
η_{hum}	0.52-0.89	3.7%
ε_{hum}	0.32-0.66	5.3%

2.5. Conclusions to Chapter 2

1. The developed experimental setup has enabled both the investigation of the air humidification process in a film-type contact heat exchanger and the examination of the individual effects of air flow rate, water flow rate, and heat flux on the energy performance of contact humidifiers, while keeping other parameters constant or allowing only minimal variation.

2. Real-time monitoring and visualization of the air temperature and humidity data using the measurement and control equipment by *Regmik* have allowed for a detailed analysis of the heat and mass transfer dynamics within the humidifier. This facilitated accurate identification of the humidifier's operating regimes and an objective evaluation of its efficiency and performance.

3. An assessment of the maximum relative and absolute uncertainties arising during the experimental investigations and calculation of the derived quantities has been conducted. The employed measurement equipment and experimental methodology enabled the determination of the humidifier's energy performance characteristics with a maximum combined uncertainty of $\pm 11\%$. The maximum imbalance in the humidifier's thermal balance across all conducted experiments was 8 %.

CHAPTER 3. RESULTS OF STUDYING THE OPERATING PARAMETERS AND ENERGY CHARACTERISTICS OF THE CONTACT HUMIDIFIER

3.1. Design Air Flow Rate

3.1.1. Water Film and Air Flow Regimes in a Vertical Tube

In direct-contact film-type heat exchangers with counterflow of air-water mixture in a vertical tube, three two-phase flow regimes occur (Fig. 3.1).

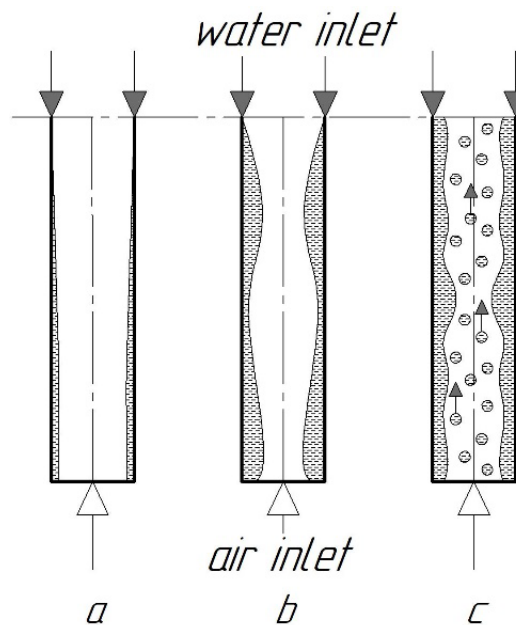


Fig. 3.1. Flow regimes of water film and air in a vertical tube: a – film flow without waves ($Re_{air} < 2300$); b – waves on the liquid surface ($Re_{air} = 2300 \dots 8000$); c – “flooding” regime ($Re_{air} = 8000 \dots 30000$)

At low air Reynolds numbers ($Re_{air} < 2300$), the falling film flows downward due to gravity with almost no waves (Fig. 3.1.a). As the air velocity gradually increases ($Re_{air} = 2300 \dots 8000$), waves begin to form on the surface of the film (Fig. 3.1.b). With further increase in air velocity, the liquid flows both upward and downward simultaneously (Fig. 3.1.c). This transition is referred to as “flooding”. The air flow velocities at which flooding occurs can be identified either through visual observation or by a sudden increase

in hydraulic resistance. If the air velocity is sufficiently high ($Re_{air} > 30000$), the entire liquid begins to move upward. In this regime, proper operation of a film-type direct-contact heat exchanger with a counterflow air-water stream is not possible [74].

Experimental data from various authors indicate that the boundaries between different flow regimes are not sharply defined and generally fall within the aforementioned ranges of air Reynolds numbers [75].

3.1.2. Flooding Point

The existing experimental results for determining the flooding point are known to be highly dependent on the design of the inlet and outlet sections of the investigated tubes [76]. Many of the results were summarized by Jeong and No [77] for tubes of various shapes. The authors [76, 77] identified the following mechanisms for the onset of flooding:

1. Flooding caused by surface waves: the amplitude of large waves increases when the waves collide in the cross-section of the tube. As a result, liquid bridges are formed, which break up into droplets and are carried upward by the air flow.
2. An increase in wave amplitude in the surroundings of the outlet, which starts as pressure-induced upflow of the stationary hanging liquid torus dripping from the borderline of the tube outlet section.
3. Entrainment of individual liquid droplets from the wavy surface of the film.

The experimental results presented in [77] indicate that flooding is merely a result of flow instability induced by the design of the outlet section of the tube. Flooding begins at much lower air velocities than can be predicted based on instabilities inside the tube. This explains the significant deviations between flooding curves obtained experimentally by different authors [76]. The key parameters influencing the onset of flooding are the design of the inlet and outlet sections of the tube, the length and diameter of the tube, as well as the viscosity and surface tension of the investigated liquids [76].

Based on a review of 2500 sets of experimental data obtained for liquids with viscosity similar to that of water, Jeong and No [77] proposed determining the onset of flooding using the following empirical equation:

$$j_a^{1/2} = aj_w + bj_w^{1/2} + c, \quad (3.1)$$

where superficial phase velocities are determined as follows

$$j_i = w_i \left[\frac{\rho_{i,in}}{(\rho_{w,in} - \rho_{a,in})dg} \right]^{\frac{1}{2}}. \quad (3.2)$$

The index $i = a, w$ denotes the air and liquid phase.

For a circular vertical tube with smooth inlet and outlet geometry, the authors [77] analyzed 536 experimental data points. All data corresponded to the following conditions: air-water system, countercurrent flow regime with water supplied from the top, tube length ranging from 0.7 to 2 m, and a diameter between 20 and 50 mm. The best fit for generalizing all 536 experimental data with formula (3.1) is achieved using the following coefficient values:

$$a = -0.439; b = -0.123; c = 0.791. \quad (3.3)$$

It should be noted that, to date, accurate methods for calculating air pressure losses below the flooding point are lacking. This is due to the predominant influence of the outlet geometry on flooding and the momentum transfer of the dispersed liquid droplets resulting from entrainment effects at the wavy film surface [76].

3.1.3. Determination of the Optimal Air Flow Rate

It is known that the higher the air flow rate passing through an HDH system, the greater its productivity [50, 57-61]. This is because an increase in airflow rate intensifies heat and mass transfer processes in the humidifier. As a result, more moisture is transferred to the air in a heat exchanger. At the same time, when the air flow rate increases in vertical tube direct contact heat exchangers, the liquid film flow is disrupted, and simultaneous upward movement of water and air begins. This regime is called “flooding” and is characterized by the detachment and entrainment of water bubbles by the air flow, along with a sudden increase in hydraulic resistance. Operating an HDH system under such conditions will lead to distillate contamination and increased energy consumption.

Thus, when using a vertical tube as a humidifier, it is necessary to find an optimal air flow rate that, on the one hand, ensures maximum HDH system productivity and, on the other, prevents the onset of an inefficient flooding regime. To achieve this goal, several experiments were conducted to measure the total air pressure losses in the humidifier at various air velocities and water flow rates. The obtained results are shown in Figure 3.2.

As seen from Figure 3.2, the experimental values of the total air pressure drop of single-phase flow ($m_w = 0$ kg/h) almost coincide (error $\pm 14\%$) with the frictional pressure drop obtained with the following Darcy-Weisbach’s correlation:

$$\Delta P_{a,calc} = 0.5 f d^{-1} \rho_{a,in} w_{a,in}^2, \quad (3.4)$$

$$f = 0.3164 Re_a^{-0.25}. \quad (3.5)$$

For the air in a tube humidifier, friction pressure loss is dominant. For engineering calculations, the values of the hydrostatic pressure difference and the acceleration pressure loss can be neglected.

The relationship between the experimental and calculated values of air pressure drop for values across all studies is shown in Figure 3.3. The solid line represents the

theoretical results. The closer a square is to the black line, the smaller the deviation between $\Delta P_{a,calc}$ and $\Delta P_{a,exp}$. It can be seen that the maximum discrepancy is 14%.

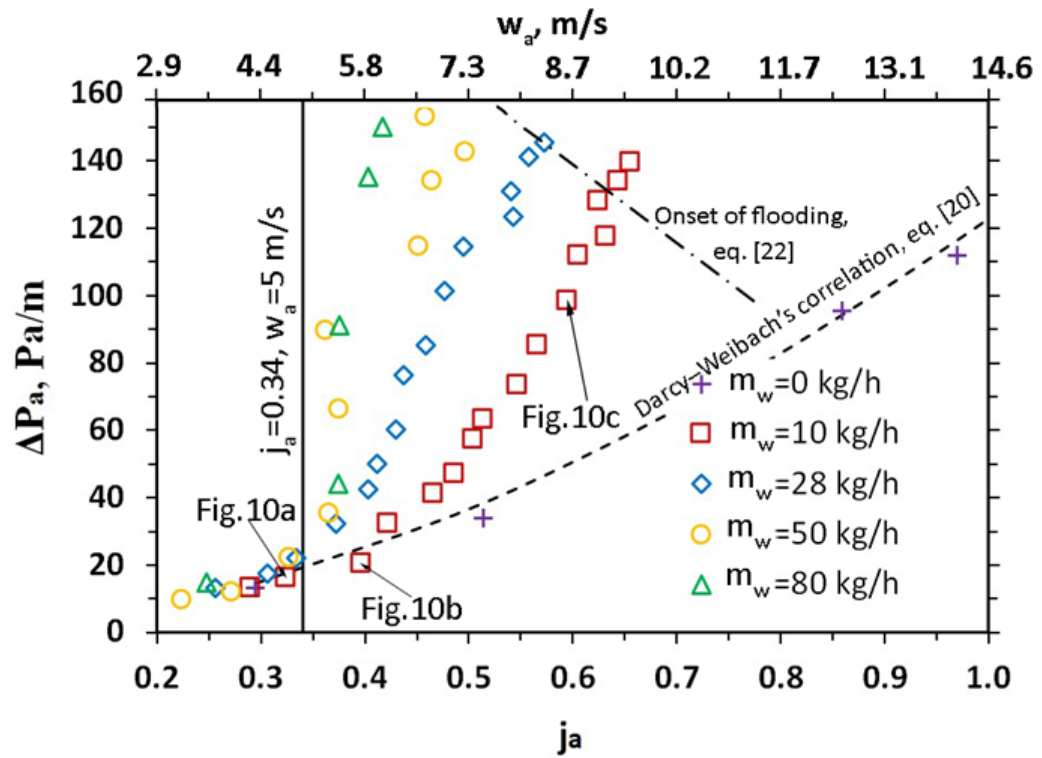


Fig. 3.2. Experimental values of total air pressure drop in a tube humidifier

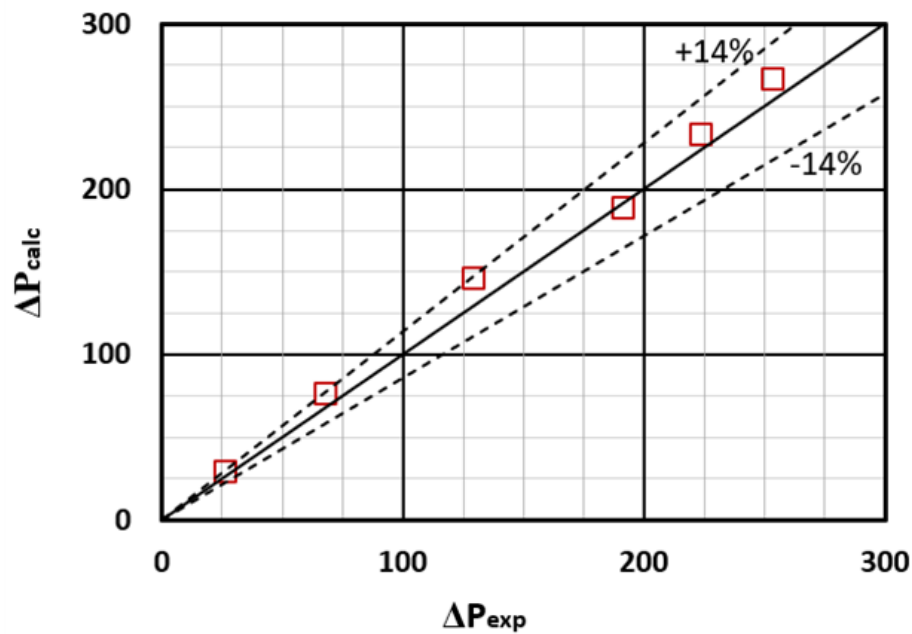


Fig. 3.3. The relationship between $\Delta P_{a,calc}$ and $\Delta P_{a,exp}$ in the humidifier during the experiments

The mean absolute deviation, mean deviation, and root mean square deviation of the heat balance based on water and air in the humidifier are determined using the corresponding formulas:

$$e_A = \frac{1}{n} \sum 100 \left| \frac{\Delta P_{a,calc} - \Delta P_{a,exp}}{\Delta P_{a,exp}} \right| \quad (3.6)$$

$$e_R = \frac{1}{n} \sum 100 \left(\frac{\Delta P_{a,calc} - \Delta P_{a,exp}}{\Delta P_{a,exp}} \right) \quad (3.7)$$

$$\sigma_N = \left[\frac{1}{n-1} \sum (e - e_R)^2 \right]^{0.5} \quad (3.8)$$

where $e = 100 \left(\frac{\Delta P_{a,calc} - \Delta P_{a,exp}}{\Delta P_{a,exp}} \right)$, n is the number of calculation points.

The percentage of calculation points that match the experimental values within the $\pm 14\%$ error margin is also determined. The results of the air pressure drop uncertainty calculations in the humidifier are summarized in Table 3.1.

Table 3.1. Uncertainties of the air pressure drop in the humidifier

<i>Uncertainty</i>	<i>Value</i>
mean absolute deviation e_A , %	7.7
mean deviation e_R , %	-7.2
root mean square deviation σ_N , %	5.6
Number of points predicted within the margin of error $\pm 8\%$	6 or 100%

An analysis of Figure 3.3 and the data in Table 3.1 indicates that the air pressure drop in the humidifier is determined with sufficient accuracy.

The identification of the onset of the flooding regime is conducted under the condition of equality between the superficial phase velocities of water and air, as determined by Eqs. (3.1) – (3.3).

At an air velocity in the tube of less than 5 m/s ($j_a < 0.34$), regardless of the water flow, the total air pressure drop is equal to the pressure losses of a single-phase flow. Under these parameters, the liquid film flows down almost without waves and does not interfere with the movement of air (Fig. 3.4.a). As the air velocity increases further, the total air pressure drop rises much faster than in a single-phase flow, and at water flow rates above 50 kg/h, it becomes almost independent of the air flow rate. This is due to the increasing amplitude and wave frequency on the liquid film surface. Additionally, the air begins to entrain water from the wave crests in the surrounding area of the tube outlet. The first appearance of single droplets from the wavy film surface is observed at $w_a = 6.18$ m/s and $j_a = 0.42$ (Fig. 3.4.b). The droplets rise with the air flow to a small height and then fall back down under the influence of gravity.

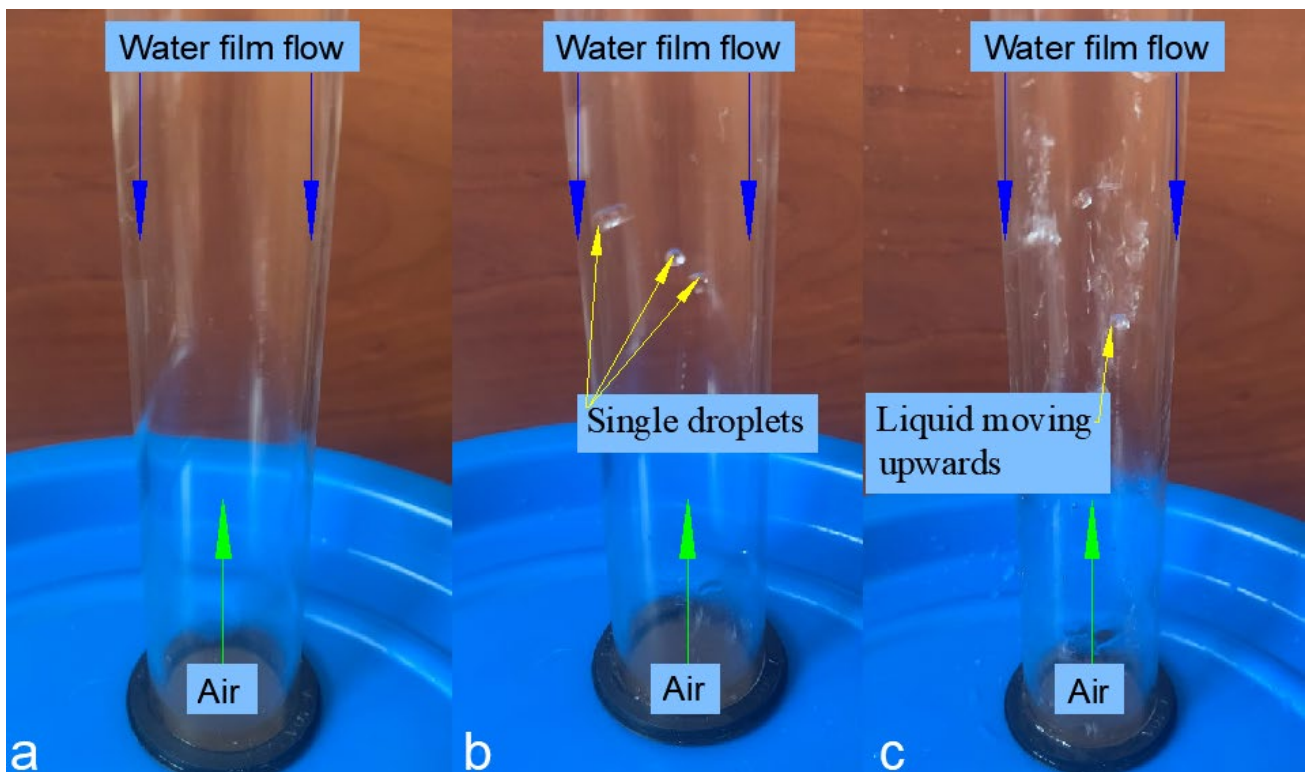


Fig. 3.4. Flow regimes in the tube humidifier:

a - film flow without waves; b – waves on the liquid surface; c – “flooding” regime onset

At a water flow rate of 10 kg/h, the onset of the flooding regime is observed at $j_a=0,61$ ($w_a=8.83$ m/s, $Re_a=15254$). Under these conditions, most of the liquid flowing to the lower edge of the tube is entrained by the incoming atmospheric air and recirculates back into the humidifier. As a result, a liquid layer forms at the bottom of the tube, through which the air passes, leading to the flow flooding (Fig. 3.4.c). It should be noted that the experimentally obtained values of Re_a , corresponding to the onset of transition between flow regimes, aligned with those reported in the study [70].

From Figure 3.1, it is evident that limiting the maximum air flow rate based on the onset of the flooding regime is impractical, as a sharp increase in the total air pressure drop (and consequently in fan power consumption) begins at lower air velocities. Considering this, it is proposed to limit the maximum superficial phase velocity in the humidifier to 0.34. Under this condition, contamination of the condensate by droplets from saline water is prevented, and the lowest pressure losses are ensured.

3.2. Optimal MR Ratio

The mass flow rate ratio (MR) is one of the key indicators for evaluating the energy efficiency of an HDH system. The MR value is calculated as the ratio between the saline water flow rate and the external air flow rate:

$$MR = m_w/m_a. \quad (3.9)$$

It is established that the lower the MR value, the higher the energy efficiency of the HDH system [50, 58, 65, 78]. This is because a lower saline water flow rate through the dehumidifier results in a higher outlet temperature of the water (Fig. 1.4). Consequently, less heat is required in the heater to raise the water to the desired temperature. However, for vertical tubes, the minimum water flow rate is determined by maintaining a continuous falling film over the entire surface of the tube [75, 79].

As seen from Figure 3.5, the temperatures $t_{w.in}$ and $t_{a.out}$ increase as MR decreases, while the humidity value φ_{out} remains constant. When the film breakup occurs (Fig. 3.6),

the temperature $t_{w.in}$ continues to rise, whereas the values $t_{a.out}$ and ϕ_{out} drop sharply. This is because the disruption of a continuous falling film reduces the intensity of the heat and mass transfer process in the tube. As a result, the amount of heat transferred to the air in the humidifier decreases.

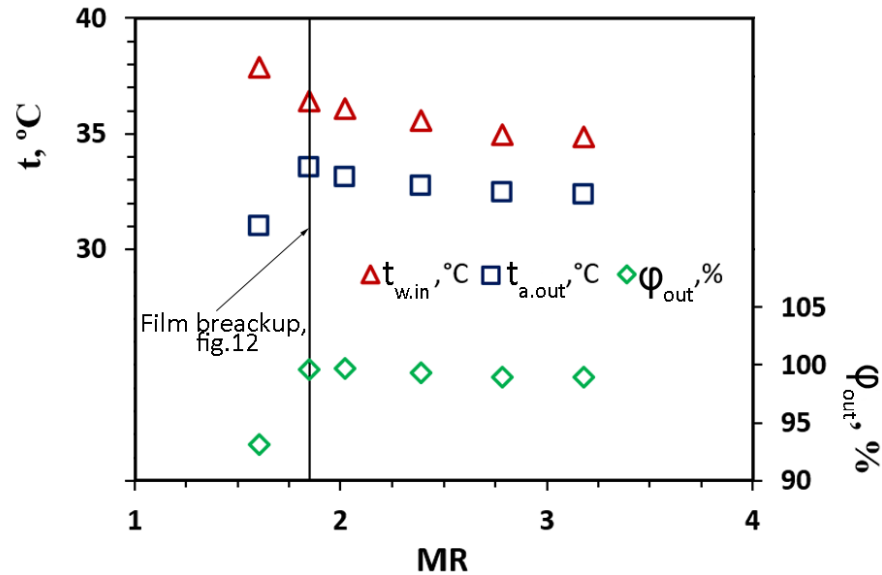


Fig. 3.5. Mass flow rate ratios required to maintain a continuous falling film

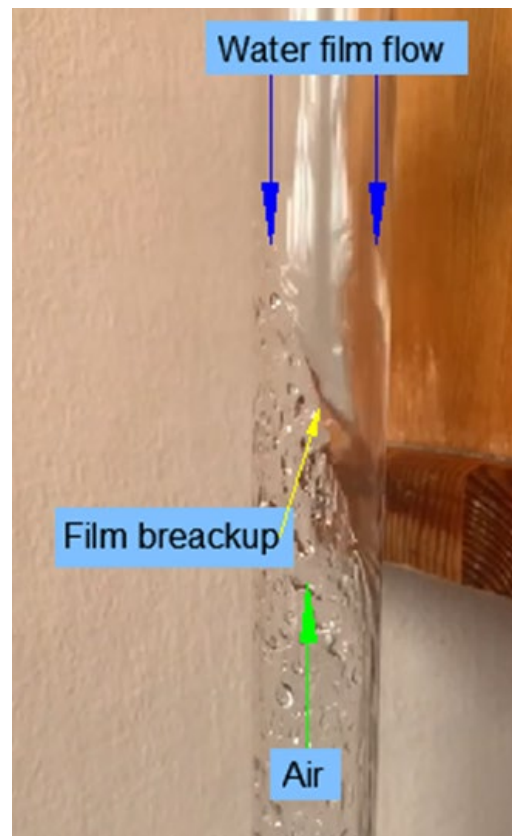


Fig. 3.6. The onset of the film breakup at MR=2

An analysis of Figures 3.7 and 3.8 shows that reducing the water flow rate (and consequently the MR coefficient) leads to an overall increase in the humidifier efficiency. Specifically, the mass flow rate of moisture $\Delta\omega$ increases, the specific energy consumption (SEC) decreases, while the thermodynamic and exergy efficiency of the humidifier remain nearly unchanged. However, when the film breakup occurs (Fig. 3.6), SEC sharply increases, while $\Delta\omega$, ε_{hum} , η_{hum} decrease significantly. This operating regime is inefficient for an HDH system. Therefore, setting the minimum MR coefficient for tube humidifiers at 2 is a reasonable approach. Under these conditions, a continuous liquid film flow is maintained, ensuring the most efficient humidifier performance.

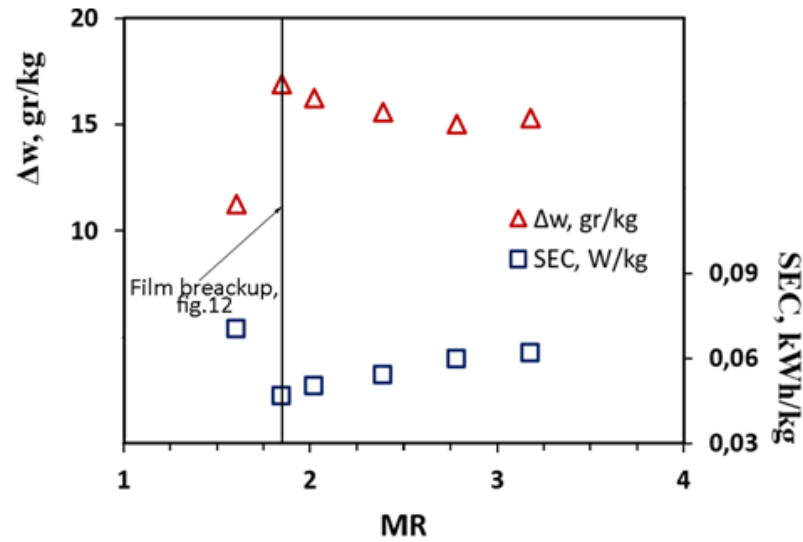


Fig. 3.7. Impact of MR on the humidifier's energy indicators

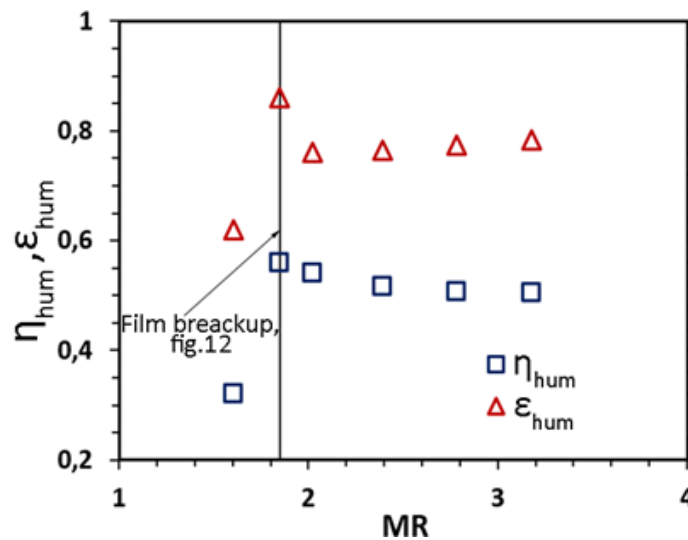


Fig. 3.8. Impact of MR on the humidifier's efficiency

3.3. Energy Efficiency Indicators

We conducted a series of experiments to determine the maximum energy efficiency of a tube humidifier. All experiments were carried out at a constant (optimal) air velocity and water flow rate ($w_a = 5$ m/s, $m_a = 11$ kg/h, $MR = 2$). During the experiments, the water temperature at the inlet of the humidifier $t_{w.in}$ was varied. The maximum $t_{w.in}$ value was limited to 60 °C to prevent scale formation in the system components [37]. The required $t_{w.in}$ value was set by adjusting the power Q_w of water to the flow heater (6) using the regulator (5) (Fig. 2.2).

Let us consider the effect of $t_{w.in}$ on the energy performance of the tube humidifier. As seen from Figure 3.9, the higher the $t_{w.in}$ in value, the higher the outlet air temperature $t_{a.out}$. This enhances heat and mass transfer processes in the humidifier and consequently increases its performance (Fig. 3.10). At the same time, the specific energy consumption of the humidifier remains nearly unchanged.

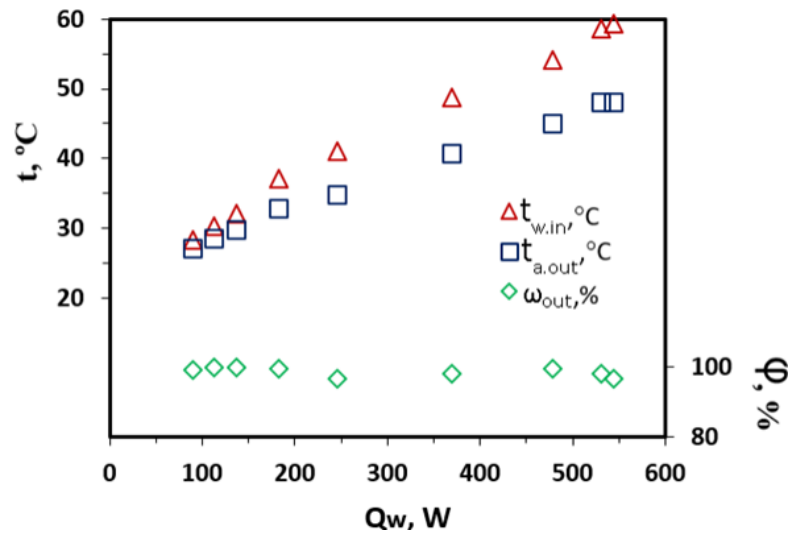


Fig. 3.9. Impact of the supplied heat on the air and water parameters

As seen from Figure 3.11, the thermodynamic efficiency η_{hum} decreases with an increase in $t_{w.in}$. This is due to the growing temperature difference ($t_{w.in} - t_{a.out}$) in the upper part of the humidifier. According to Equations (2.17) – (2.19), as this temperature difference ($t_{w.in} - t_{a.out}$) increases, the irreversibility of heat and mass transfer processes in

the humidifier also rises. At the same time, the exergy efficiency ε_{hum} remains practically unchanged, with an average value of 0.58.

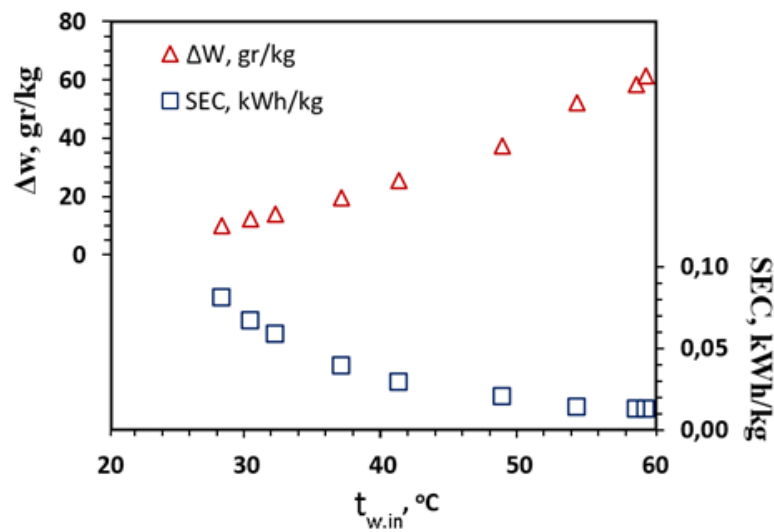


Fig. 3.10 Impact of the supplied heat on the energy indicators

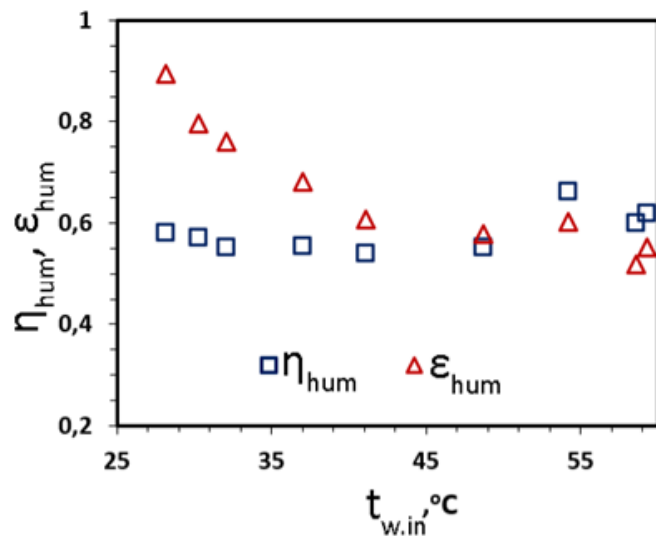


Fig. 3.11. Impact of the supplied heat on the humidifier's efficiency

3.4. Conclusions to Chapter 3

The experimental studies of the air humidification process in a film-type contact heat exchanger allow the following conclusions to be drawn:

1. The optimal value of the air superficial phase velocity in the tube humidifier ($j_a=0.34$) has been established. Under this condition, the performance of the HDH system will be maximum, and the air pressure drop will be minimal. At the same time, contamination of the condensate by droplets from saline water has been prevented.

2. It has been shown that for air superficial phase velocity less than 0.34, the air pressure drop in the humidifier can be determined with sufficient accuracy (error $\pm 14\%$) using Darcy-Weisbach's correlation (3.4).

3. The minimum value of the mass flow rate ratio in the tube humidifier ($MR=2$) has been established. Below this MR value, a continuous film flow is disrupted, resulting in a deterioration of the intensity of heat and mass transfer processes in the tube.

4. The influence of the inlet water temperature on the energy efficiency of the humidifier has been demonstrated. At higher values of $t_{w.in}$, the humidifier performance increases. At the same time, the specific energy consumption of the humidifier remains nearly unchanged. The thermodynamic efficiency of the humidifier decreases with an increase in $t_{w.in}$, while the exergy efficiency remains practically unchanged.

CHAPTER 4. THERMODYNAMIC MODEL DESING AND CALCULATION METHOD

4.1. Mathematical Description of the Model

A thermodynamic model of a tube humidifier was developed using the engineering software PTC Mathcad. For the modeling, the following assumptions were made [80]:

- the HDH-system operates under steady conditions;
- heat losses from the equipment are neglected.

The model includes balance equations (4.2) and (4.3), and the amount of heat transferred from the heated water to the air in the humidifier due to heat and mass transfer [70].

$$Q_w = Q_a = Q_{hmt}. \quad (4.1)$$

$$Q_w = m_w c_{p,w,in} t_{w,in} - (m_w - \Delta\omega) c_{p,w,out} t_{w,out}. \quad (4.2)$$

$$Q_a = (m_a + \Delta\omega) h_{a,out} - m_a h_{a,in}. \quad (4.3)$$

$$Q_{hmt} = Q_{evap} + Q_{con} = \Delta\omega h_{vl} + h_{con} F_{hmt} \Delta T, \quad (4.4)$$

where Q_{evap} is the heat transferred by water evaporation into the air (W);

Q_{con} is the heat transferred to the air due to its heating (W).

The amount of moisture absorbed by the air is determined using the following equation:

$$\Delta\omega = J F_{hmt}, \quad (4.5)$$

The diffusion flux is calculated using the formula:

$$J = \frac{h_d}{R_v t_{a,aver}} (p_{w,par} - p_{a,par}). \quad (4.6)$$

The partial pressure of water vapour in moist air along the interphase surface $p_{w,par}$ is determined based on the average water temperature. The partial pressure of water vapor

in the moist air away from the interphase surface $p_{a,par}$ is assumed to be the arithmetic mean of partial pressures at the air inlet and outlet of the humidifier:

$$p_{a,par} = 0.5(p_{a,in,par} + p_{a,out,par}). \quad (4.7)$$

The pressures $p_{a,in,par}$ and $p_{a,out,par}$ are determined by the temperatures $t_{a,in}$ and $t_{a,out}$, respectively.

The correlations for determining the heat and mass transfer coefficients are derived from [70]:

$$h_d = ShD/d, \quad (4.8)$$

$$h_{con} = Nu\lambda/d, \quad (4.9)$$

where

$$Sh = 0.009Re_a^{0.8}Re_f^{0.16}Sc_a^{0.4}, \quad (4.10)$$

$$Nu = 0.009Re_a^{0.8}Re_f^{0.16}Pr_a^{0.4}. \quad (4.11)$$

The experimental results indicate that the tube humidifier operates most efficiently at a constant air velocity ($j_a=0.34$, section 3.1), and a constant water flow rate (MR=2, section 3.2). Additionally, the operational temperature range for air and water in HDH systems varies between 20...60 °C [81]. This allows assuming constant values for w_a , MR, ν_a , Sc_a , and D . By substituting these into Equations (4.8) and (4.9), a simplified empirical formula for engineering calculations is obtained:

$$h_d = 0.0246d^{-0.04}, \quad (4.12)$$

$$h_{con} = 26d^{-0.04}. \quad (4.13)$$

The model validation was carried out by comparing the experimental and calculated values of air and water temperatures at the humidifier outlet. As seen in Figure 4.1, all the temperatures align within the accuracy of ± 4 . The only exception is the point at which the film breakup occurs.

The mean absolute deviation, mean deviation, and root mean square deviation of air and water temperatures at the humidifier outlet are determined using the following formulas:

$$e_A = \frac{1}{n} \sum 100 \left| \frac{t_{i,calc} - t_{i,exp}}{t_{i,exp}} \right| \quad (4.14)$$

$$e_R = \frac{1}{n} \sum 100 \left(\frac{t_{i,calc} - t_{i,exp}}{t_{i,exp}} \right) \quad (4.15)$$

$$\sigma_N = \left[\frac{1}{n-1} \sum (e - e_R)^2 \right]^{0.5} \quad (4.16)$$

where $e = 100 \left(\frac{t_{i,calc} - t_{i,exp}}{t_{i,exp}} \right)$, n is the number of calculated data points.

The percentage of calculated data points that match the experimental values within an error margin of $\pm 4\%$ is also determined. The results of the error analysis of air and water temperatures at the humidifier outlet are summarized in Tables 4.1 and 4.2.

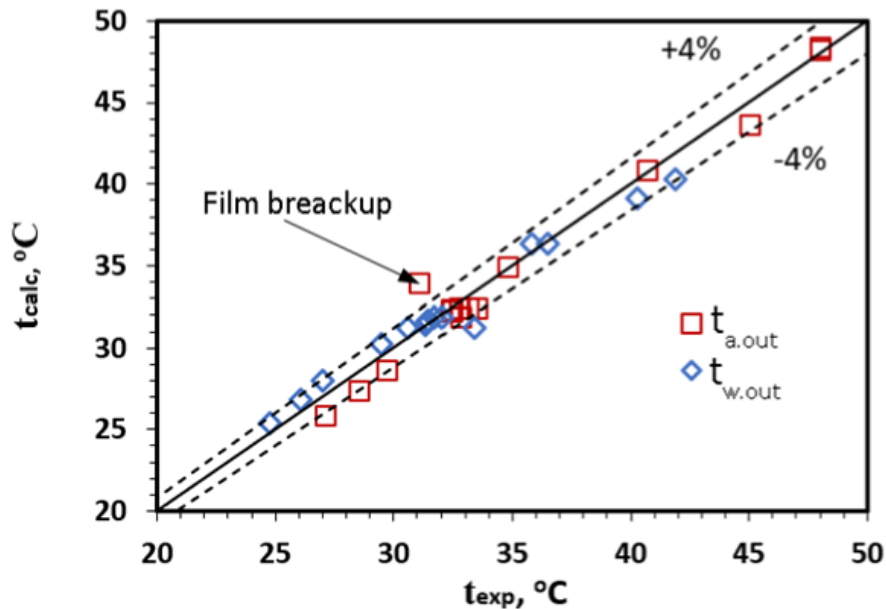


Fig. 4.1. Validation of the thermodynamic model with experimental data

Table 4.1. Uncertainties of the air temperature at the humidifier outlet

<i>Uncertainty</i>	<i>Values</i>
mean absolute deviation e_A , %	2.6
mean deviation e_R , %	1.0
root mean square deviation σ_N , %	5.6
number of data points that are generalized within an error margin of $\pm 4\%$	13 or 100%

Table 4.2. Uncertainties of the water temperature at the humidifier outlet

<i>Uncertainty</i>	<i>Value</i>
mean absolute deviation e_A , %	1.9
mean deviation e_R , %	-0.4
root mean square deviation σ_N , %	4.2
number of data points that are generalized within an error margin of $\pm 4\%$	13 or 100%

An analysis of Figure 4.1 and the data in Tables 4.1 and 4.2 indicates that the developed mathematical model is sufficiently accurate.

4.2. Results of Mathematical Modeling

4.2.1. Optimal Geometric Dimensions of the Humidifier

The following input data have been adopted for modeling the operation of the film humidifier [82]:

- water inlet temperature $t_{w,in} = 60\text{ }^\circ\text{C}$;
- constant air velocity and water flow rate: $j_a = 0.34$, $MR=2$;
- external air parameters $t_{a,in} = 25\text{ }^\circ\text{C}$, $\varphi_{a,in} = 50\%$;
- air humidity at the humidifier outlet $\varphi_{a,out} = 98\%$.

The modeling results provide values $t_{a,out}$ and $t_{w,out}$ for different geometric dimensions of the humidifier. Based on these results, the following energy characteristics of the humidifier are determined:

- performance G_{fw} (eq. 2.6);
- evaporation rate per unit humidifier volume ER (Eq. 2.15);
- humidifier efficiency η_{hum} (Eq. 2.17);
- exergy efficiency ε_{hum} (Eq. 2.20).
- gain output ratio:

$$GOR = \frac{G_{fw} h_{lv}}{Q_w}; \quad (4.17)$$

- electric energy consumption:

$$SEC = \frac{N_{fan} + N_{pump}}{G_{fw}}, \quad (4.18)$$

where N_{fan} is the fan electric power, which is calculated using the following formula:

$$N_{fan} = \frac{1}{l} \frac{G_a \Delta P_a}{\eta_{fan} \rho_{a.in}}; \quad (4.19)$$

where ΔP_a denotes specific aerodynamic pressure losses in the humidifier (Eq. 3.4);

η_{fan} is the efficiency of the fan according to the specifications (Chapter 2.1).

N_{pump} is the water pump electric power, which is determined by the formula:

$$N_{pump} = \frac{G_{sw} \Delta P_w}{\eta_{pump} \rho_{w.in}}; \quad (4.20)$$

where ΔP_w is the pressure losses in the water flow. For a vertical tube-type humidifier, it can be expressed as follows:

$$\Delta P_w = 1.1\rho_{w.in}gh. \quad (4.21)$$

η_{pump} is the efficiency of the diaphragm pump according to the specifications (Chapter 2.1).

The results of modeling are shown in Figures 4.2 – 4.7.

As seen from Figure 4.2, the larger the values of d and h , the more moisture is absorbed by the air. A larger diameter allowed more air to pass through, and a higher tube improves the heat and mass transfer efficiency. However, with large diameters ($d > 50$ mm), the air volume passing through the central part of the tube cannot reach saturation due to insufficient contact area with the water and limited interaction time. Under these conditions, Equations (29) – (34) start to give inaccurate results and require refinement [40].

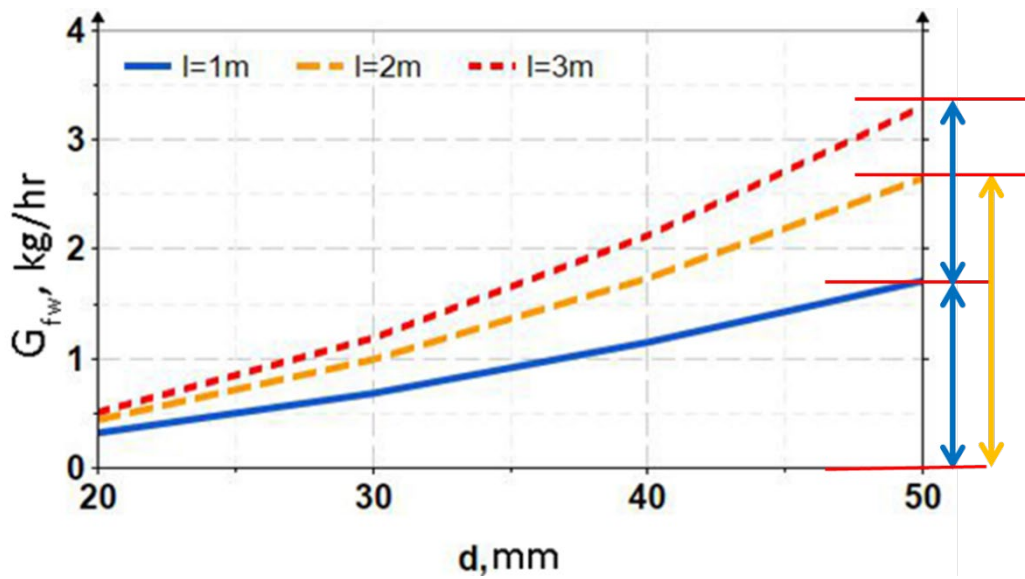


Fig. 4.2. Impact of geometric parameters on the humidifier performance

With the same diameter, the performance of two 1 m high tubes is greater than that of one 3 m long tube (Fig. 4.2). This is due to the fact that ER for the 1 m tube is the largest (Fig. 4.3).

Although the performance of the humidifier increases with its diameter (Fig. 4.2), the evaporation rate is almost independent of the diameter (рис. 4.3). This is because an

increase in performance is solely due to an increase in the geometric volume of the humidifier caused by the diameter, and an increase is linear in nature.

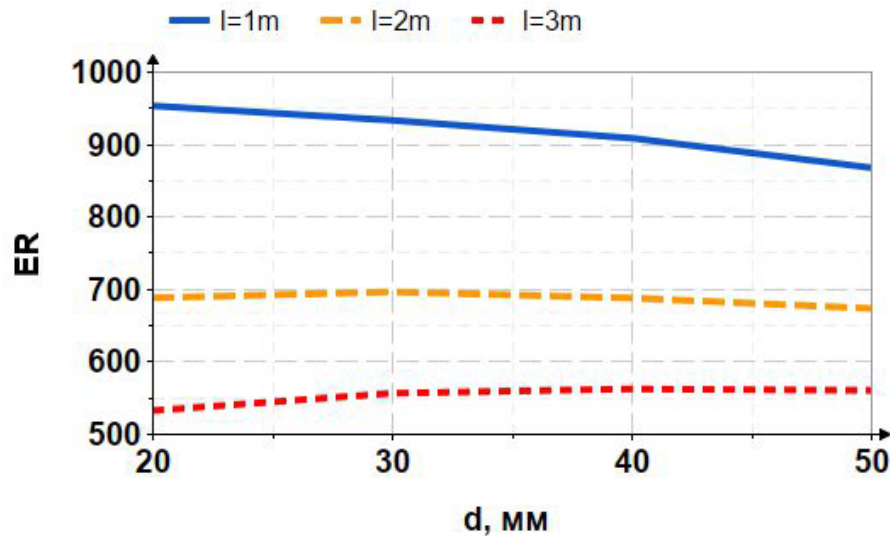


Fig. 4.3. Impact of geometric parameters on the evaporation rate

A different situation is observed with changes in the height of the humidifier. As seen from Figure 4.3, with a decrease in the height of the humidifier, the value of ER increases. Thus, although increasing the height leads to an increase in the humidifier's performance, it is inefficient in terms of the use of the humidifier's volume.

Therefore, it is not advisable to increase the height of the tube by more than 1 m; it is better to increase the number of tubes.

Figure 4.4. shows a change in the energy efficiency coefficient of the humidifier (GOR) depending on the diameter and height of the tube. It can be seen that all three curves (for different lengths) practically coincide. The value of $GOR \approx 0.78$ remains constant even when the diameter changes from 20 to 50 mm. This indicated that changes in geometric dimensions do not affect the thermal efficiency of the film-type humidifiers. In other words, an increase in the supplied heat directly contributes to increasing performance but does not change the efficiency of thermal energy conversion.

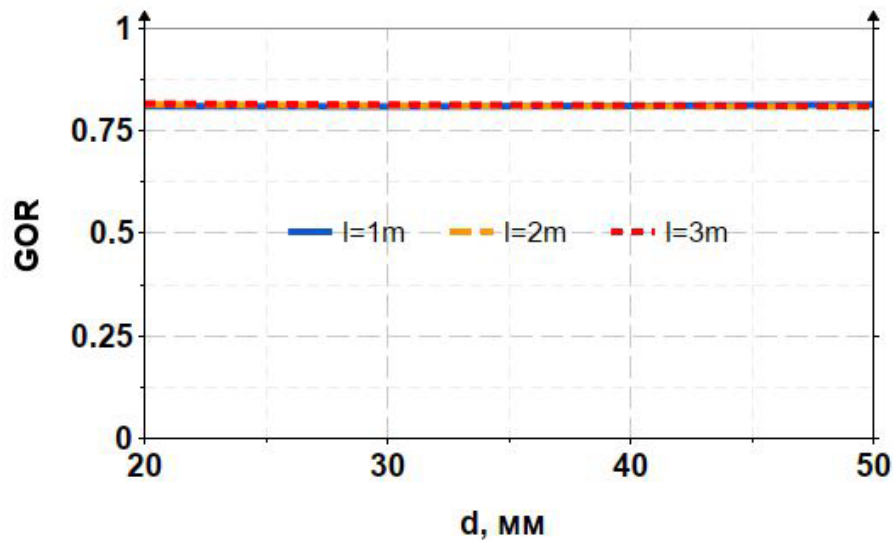


Fig. 4.4. Impact of the geometric parameters on GOR

As seen from Figure 4.5, the specific energy consumption practically does not depend on the height of the humidifier. The main reason for this is the low pressure losses of air and water in the heat exchanger. Such low pressure losses do not have a noticeable effect on electricity consumption when the tube height changes.

In contrast, with an increase in the humidifier diameter, the specific energy consumption increases (Fig. 4.5). This is explained by an increase in the air flow rate that must be pumped through the humidifier. According to (4.19), the greater the flow rate, the higher the energy costs for its movement.

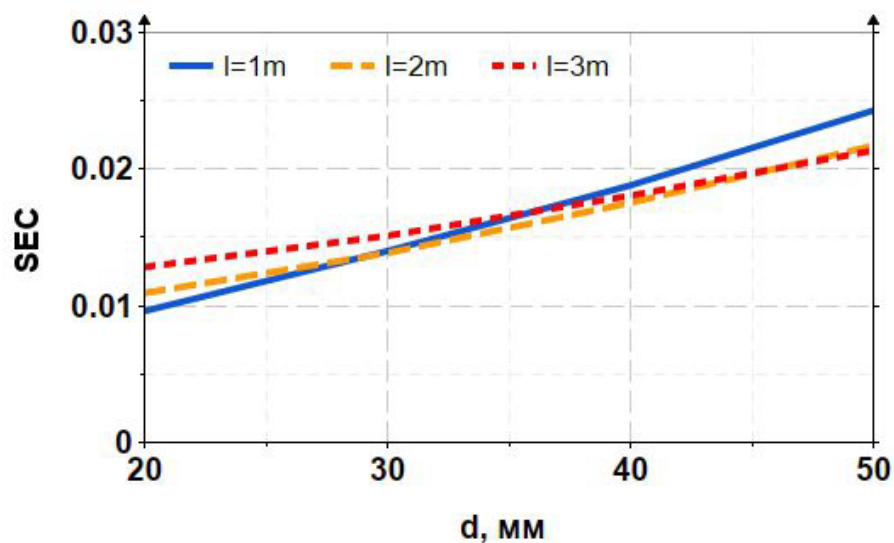


Fig. 4.5. Impact of the geometric parameters on electric energy consumption

As seen from Figures 4.6 and 4.7, the influence of the humidifier's geometric dimensions on ε_{hum} and η_{hum} is similar. As the diameter d increases, both indicators decrease, while an increase in the tube length l results in their growth.

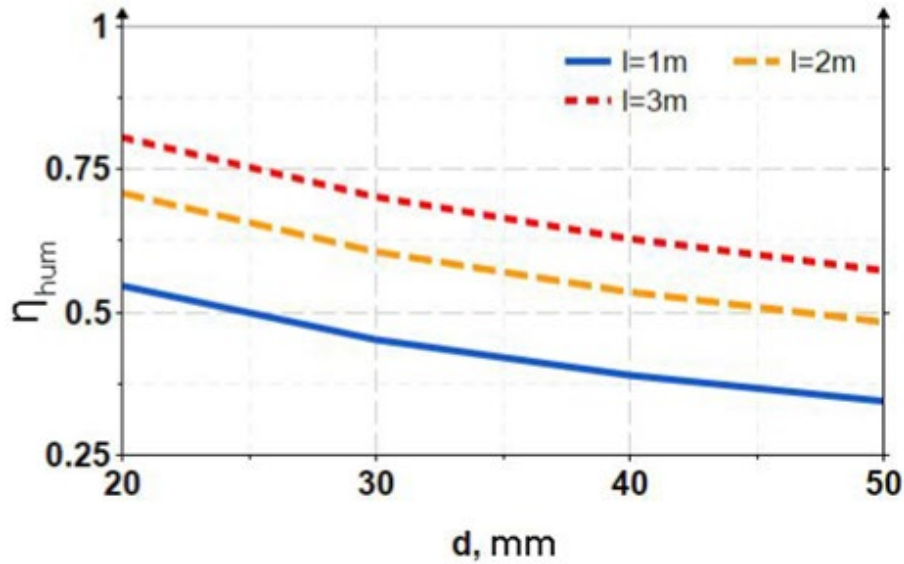


Fig. 4.6. Impact of the geometric parameters on thermodynamic efficiency

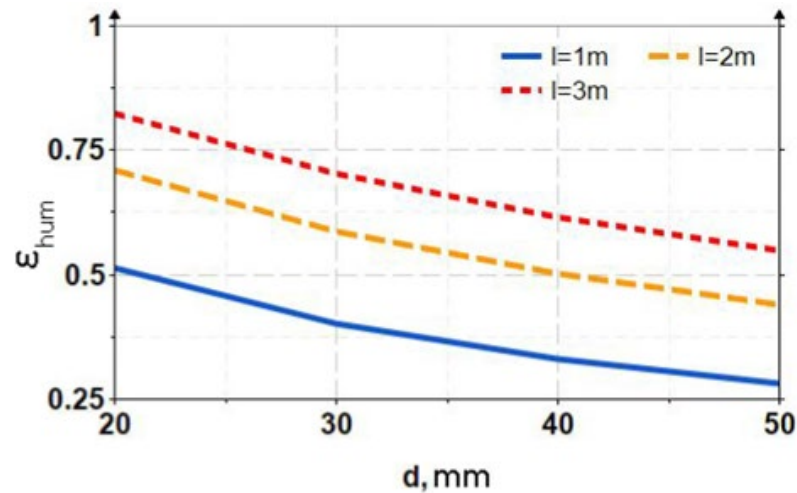


Fig. 4.7. Impact of the geometric parameters on exergy efficiency

Analyzing the graphs in Figures 4.2 – 4.7, it can be concluded that the optimal geometric dimensions of the tube film humidifier are a diameter of $d = 50$ mm and a height of $l = 1$ m. With these parameters, the volume of the humidifier is utilized most efficiently, allowing for its high performance with minimal thermal and electrical energy consumption.

The only drawback of this configuration is its relatively low thermodynamic and exergy efficiency. However, if the renewable solar energy is used to heat the water and power the pump and fan, this drawback can be considered negligible.

4.2.2. Influence of External Air Parameters on the Humidifier Efficiency

The influence of ambient air parameters ($t_{a,in}$ and $\varphi_{a,in}$) on the energy performance of the film humidifier was investigated. The simulation of its operation was conducted using the following initial conditions [82]:

- water inlet temperature $t_{w,in} = 60$ °C;
- constant air velocity and water flow rate: $j_a = 0.34$, $MR=2$;
- air humidity at the humidifier outlet $\varphi_{a,out} = 98\%$;
- diameter $d = 50$ mm and height $l = 1$ m.

During the modeling, the ambient air parameters varied as follows:

- $t_{a,in} = \text{const} = 25$ °C, $\varphi_{a,in} = \text{var}$ (Fig. 4.8);
- $\varphi_{a,in} = \text{const} = 50\%$; $t_{a,in} = \text{var}$ (Fig. 4.9).

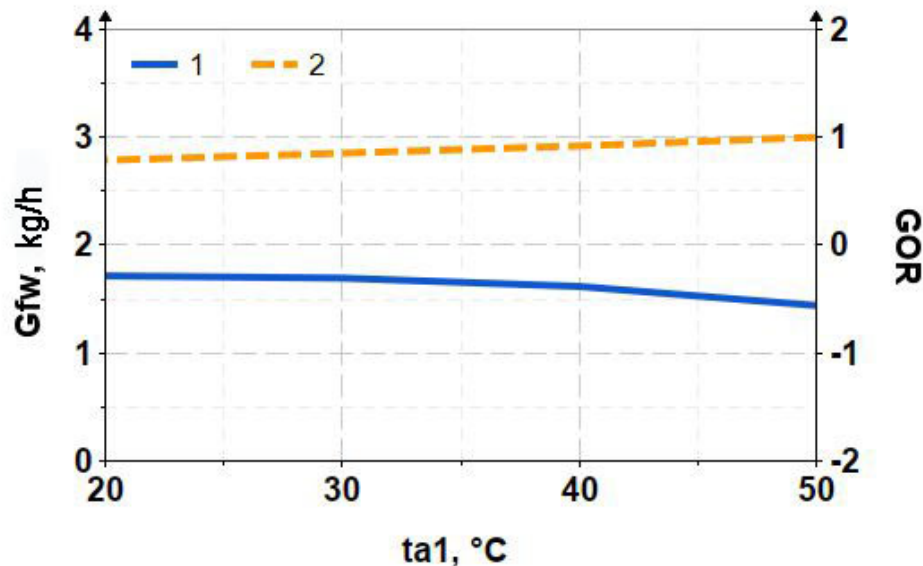


Fig. 4.8. Dependence of GOR and G_{fw} on t_{a1} at $d = 50$ mm and $l = 1$ m:

1 – G_{fw} ; 2 – GOR

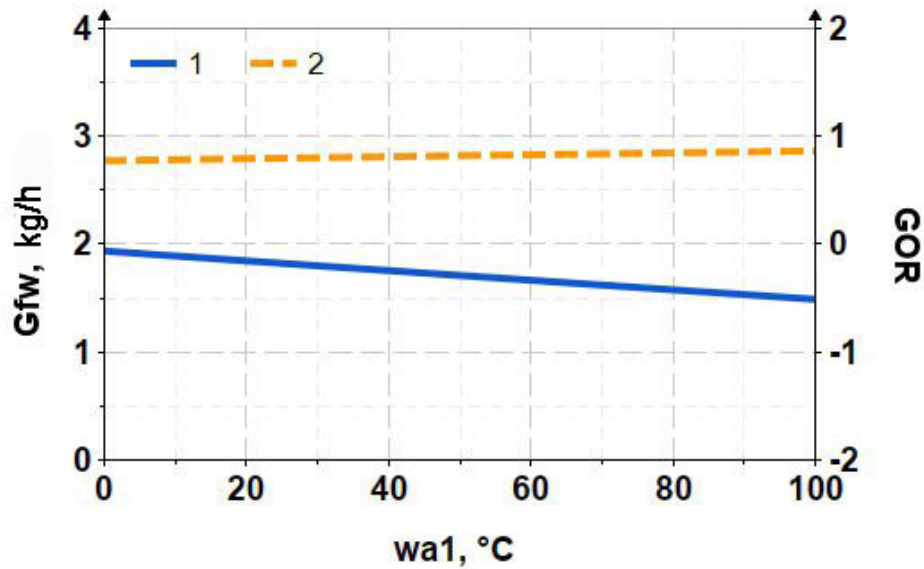


Fig. 4.9. Dependence of GOR and G_{fw} on $\varphi_{a,in}$ at $d = 50$ mm and $l = 1$ m:

1 – G_{fw} ; 2 – GOR

Figures 4.8 and 4.9 demonstrate that the temperature of the ambient air ($t_{a,in}$) have minimal influence on the system performance. In contrast, as the relative humidity ($\varphi_{a,in}$) increases, the productivity of the humidifier decreases. This is due to the fact that a high moisture content in the ambient air reduces the amount of water vapor that can be transferred from the hot water to the air within the humidifier. At the same time, the value of GOR increases slightly with rising $t_{a,in}$ and $\varphi_{a,in}$. This outcome can be explained by the fact that during sensible heating and humidification, air becomes lighter. Consequently, at a constant velocity inside the tube ($j_a = 0.34$), the mass flow rate of the air G_a decreases, which in turn reduces the mass flow rate of the water G_w (since $G_w = 2 \cdot G_a$). As discussed in Chapter 3.2, a lower G_w requires less heat to raise the water temperature to $t_{w,in}$. It should be noted that this influence of air density on GOR variation is characteristic when the air velocity at the inlet of the humidifier is kept constant. However, if the air mass flow rate is controlled directly, then changes in $t_{a,in}$ and $\varphi_{a,in}$ do not affect the GOR coefficients.

4.3. Development of a calculation method

The results obtained from experimental studies and numerical modeling provide a solid foundation for proposing a method for calculating the performance of film-type humidifiers, as outlined below. The development of this method is based on the following assumptions [49, 80, 82]:

- the humidifier operates under steady-state conditions;
- heat losses from any equipment are neglected;
- the relative humidity of the air exiting the humidifier is assumed to be 100 %.

The input parameters for the calculation include:

- inlet water temperature $t_{w.in}$, °C;
- inlet air temperature $t_{a.in}$, °C;
- relative humidity of the inlet air $\omega_{a.in}$, %.
- diameter of the tube humidifier d , m;
- height of the tube humidifier l , m.

The proposed calculated method consists of the following steps (Fig. 4.10):

1. Determination of the mass flow rate of the air:

$$m_a = F_{hum} w_a \rho_{a.in}, \quad (4.22)$$

where $F_{hum} = 0.25\pi d^2$ is the cross-sectional area of the humidifier, m².

Air velocity w_a is determined by the formula (3.2), assuming that superficial air velocity is $j_a = 0.34$:

$$w_a = \frac{j_a}{\left[\frac{\rho_{i.in}}{(\rho_{w.in} - \rho_{a.in})dg} \right]^{0.5}}. \quad (4.23)$$

2. Determination of the mass flow rate of the water:

$$m_w = MRm_a, \quad (4.24)$$

$$MR = 2.$$

3. Specification of the air and water outlet temperatures from the humidifier:

$$t_{a.out} = t_{w.in} - 5^{\circ}C;$$

$$t_{w.out} = t_{a.in} + 5^{\circ}C.$$

4. Calculation of the heat and mass transfer coefficients h_d and h_{con} by new simplified empirical formulas (4.12) and (4.13), respectively.

5. Determination of the humidifier productivity (the amount of moisture absorbed by the air):

$$\Delta\omega = \frac{h_d F_{hmt}}{R_v t_{a.aver}} (p_{w,par} - p_{a,par}). \quad (4.25)$$

6. Calculation of the heat transferred by water evaporation into the air Q_{evap} and heat transferred to the air due to its heating Q_{con} according to the formulas:

$$Q_{evap} = \Delta\omega h_{vl}, \quad (4.26)$$

$$Q_{con} = h_{con} F_{hmt} \Delta T. \quad (4.27)$$

7. Determination of the amount of heat transferred from the heated water to the air in the humidifier due to heat and mass transfer by the formula (4.4).

8. Calculation of the heat input to water in the flow heater:

$$Q_w = c_{p,w} [m_w (t_{w,in} - t_{w,out}) + \Delta\omega t_{w,out}]. \quad (4.28)$$

9. Determination of total heat transferred to the air in the humidifier:

$$Q_a = m_a (h_{a,out} - h_{a,in}) + \Delta\omega h_{a,out}. \quad (4.29)$$

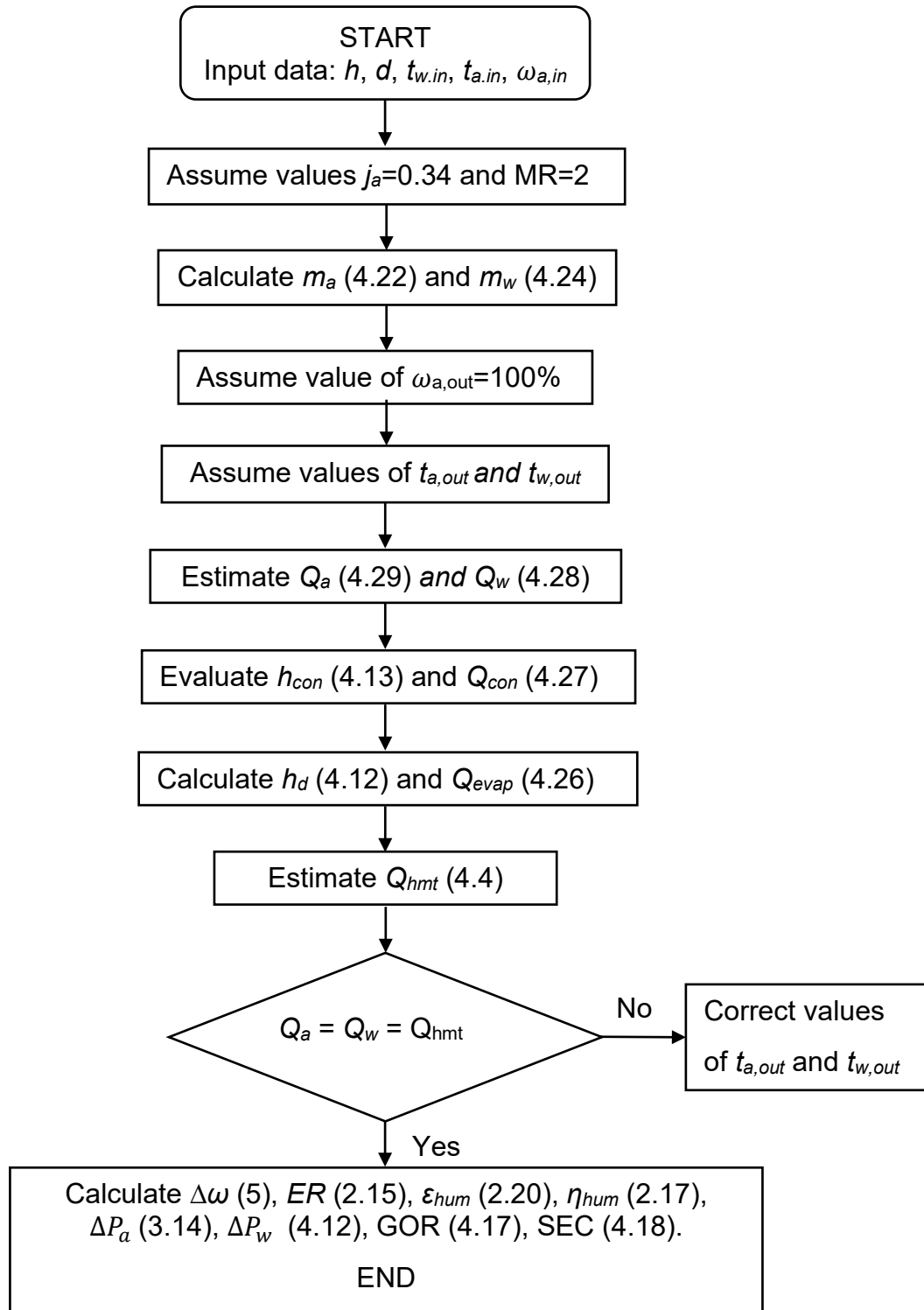


Fig. 4.10. Algorithm for calculating the tube humidifier performance parameters

10. Verification of the humidifier's heat balance conducted using Equation (4.1). If the deviation between the results obtained from the balance equations (4.28) and (4.29) and the heat and mass transfer equation (4.4) is less than 0,5%, the calculation is considered complete. In the case of a larger discrepancy, it is necessary to refine the values of the air and water temperatures at the humidifier outlet and repeat steps 4 through 9.

11. After the thermal balance is reconciled, the energetic parameters of the humidifier are determined:

- productivity G_{fw} , kg/h;
- evaporation rate per unit humidifier volume ER, kg/(h·m²), Eq. (2.15);
- efficiency η_{hum} , Eq. (2.17), and exergy efficiency ε_{hum} , Eq. (2.20);
- gain output ratio GOR, Eq. (4.17);
- electric energy consumption SEC, kW·h/kg, Eq. (4.18);
- specific aerodynamic pressure losses ΔP_a , Pa/m, Eq. (3.4);
- water head losses ΔP_w , kPa, Eq. (4.21).

The calculation algorithm for the tube humidifier is shown in Fig. 4.10.

4.4. Conclusions to Chapter 4.

1. A thermodynamic model of the humidifier has been developed based on the heat and mass transfer equations. New empirical relations (4.12) and (4.13) have been suggested for a mathematical model of the film humidifier. These formulas are recommended to be applied for tubes (with a diameter from 20 to 50 mm and a length from 1 to 3 m) under the following operating conditions of the HDH system: $ja \leq 0.34$, $MR \leq 2$, and $t_{w,in} \leq 60$ °C. For other conditions, the proposed mathematical model needs to be refined.

2. The results of modeling have demonstrated that the evaporation rate (ER) of the film humidifier is almost independent of the tube diameter but varies with height. The maximum value of ER is observed at a height of $h=1$ m. The gain output ratio (GOR) remains constant and is not influenced by the geometric parameters of the humidifier. In

contrast, the specific energy consumption (SEC) shows no dependence on the height of the tube, although a slight influence of the tube diameter has been observed.

3. The optimal geometric parameters of a tube film humidifier for HDH systems are a tube diameter of 50 mm and a height of 1 m. These dimensions have ensured the maximum productivity with minimal specific thermal and electrical energy consumption.

4. The ambient air temperature $t_{a,in}$ has almost no effect on the humidifier's productivity, whereas an increase in relative humidity $\varphi_{a,in}$ leads to a reduction in the value of G_{fw} . However, as both $t_{a,in}$ and $\varphi_{a,in}$ increase, the energy efficiency coefficient (GOR) also increases. Consequently, the amount of heat required to raise the water temperature to $t_{w,in}$ in the heater decreases.

5. The proposed calculation method for film humidifiers makes it possible to determine the key performance parameters by taking into account the main hydrodynamic, thermal, and mass transfer processes. The method is based on experimentally validated assumptions, empirical correlations for heat and mass transfer coefficients, and the energy and mass balances of the system components.

5. COMPARATIVE ANALYSIS OF THE HUMIDIFIERS' PERFORMANCE

5.1. Comparison of a Film Humidifier with Packed Bed Humidifiers

For comparison, we selected the experiments where the water temperature, air temperature, and mass flow rate ratios were approximately the same. The following packing materials met these conditions.

1. Cellulose pads from [78] and [65]. Cellulose pads are manufactured from a natural organic material – cellulose paper (Fig. 5.1). The advantages of cellulose pads include high efficiency, cost-effectiveness, and low energy consumption. However, this packing material also has several drawbacks: the need for regular maintenance, frequent replacement, and susceptibility to algae growth under humid conditions.

The humidifier with cellulose pads investigated in [78] has cross-sectional dimensions of $122 \times 30.5 \times 30$ cm³. Inside the humidifier, three cellulose pads with a total height of 65 cm are installed. The total volume of the packing material is 0.06 m³. The operating conditions and energy characteristics of the humidifier are presented in Table 5.1.



Fig. 5.1. Cellulose pads from [78]

Table 5.1. Performance indicators of the humidifier from [78]

Volume, m ³	G_a , kg/h	G_{fw} , kg/h	MR	ER, kg/(m ³ h)	GOR	η_{hum}
0.06	198	2.7	1.35	45.4	0.335	0.54
	237.6	2.3	1.83	47.6	0.351	0.34
	288	2.8	2.27	47.8	0.353	0.25

The authors in [65] investigated another form of cellulose pads – honeycomb. This packing material features a structured honeycomb lattice geometry (Fig. 5.2), which provides a large specific surface area, efficient water evaporation, and uniform airflow distribution. Due to its porous structure and high moisture retention capacity, honeycomb cellulose paper is widely used in evaporative cooling and air humidification systems. The geometric dimensions and description of the humidifier with honeycomb cellulose pads studied in [65] are provided in Section 3.1. The operating parameters and energy characteristics of the humidifier are presented in Table 5.2. The thermodynamic efficiency of the humidifier during the experiments was 0.61.

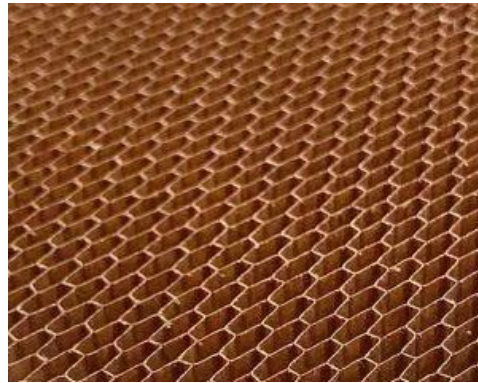


Fig. 5.2. Packing material with honeycomb cellulose paper [65].

Table 5.2. Performance indicators of the humidifier from [65]

Volume, m^3	$G_a, \text{kg/h}$	$G_{fw}, \text{kg/h}$	MR	ER, $\text{kg}/(\text{m}^3\text{h})$
0.06	10	2	5.1	16.1
	9	1.6	5.7	12.8
	8.28	1.4	6.2	11.2

2. Paddy grass, as studied in [60], is an agricultural by-product consisting of the dry stalks of rice plants left after harvesting. It represents nearly half of the total biomass yield of crops such as rice, barley, oats, and wheat. This packing material is widely available, cost-effective, easy to use, and environmentally friendly. The actual appearance of the paddy grass material is shown in Figure 1.19. It can be arranged in a humidifier either horizontally or vertically.

In study [60], a total of 1600 paddy grass stalks were used, each with a diameter of 5 mm and a length of 0.4 m. The packing density of paddy grass was $157 \text{ m}^2/\text{m}^3$, a with a total surface area of 10.05 m^2 (Fig. 5.3). The geometric dimensions and description of the humidifier filled with paddy grass are presented in Section 3.1. The operating parameters and energy characteristics are summarized in Table 5.3. The thermodynamic efficiency of the humidifier varied between 0.65 and 0.95 during the experiments.



Fig. 5.3. Paddy grass as packing material from [60]

Table 5.3. Performance indicators of the humidifier with paddy grass from [60]

Volume, m^3	$G_a, \text{ kg/h}$	$G_{fw}, \text{ kg/h}$	MR	ER, $\text{kg}/(\text{m}^3\text{h})$
0.16	21.6	0.3	1.1	4.68
	39.6	0.32	1.5	5
	54	0.34	2	5.31
	72	0.35	2.4	5.47
	90	0.39	2.9	6.09
	100.8	0.48	3.4	7.5
	122.4	0.55	3.8	8.59
	136.8	0.6	4.3	9.37
	154.8	0.72	4.7	11.25

3. Hydrophobic plastic in the form of hackettes was investigated in [61]. Hackettes are third-generation packing material. They have a hollow spherical shape and are manufactured by injection molding (see Fig. 5.4). Hackettes are characterized by a high specific geometric surface area, low hydraulic resistance, and minimal pressure drop.

Additionally, they exhibit good water retention capacity and provide complete surface wetting during operation.

For the samples used in [61], the void fraction was 92%, and the specific surface area was $280 \text{ m}^2/\text{m}^3$. The geometric dimensions and a detailed description of the humidifier filled with hydrophobic plastic hackettes are provided in Section 3.1. The operating parameters and energy characteristics of the humidifier are presented in Table 5.4.



Fig. 5.4. Hydrophobic plastic packing material in the form of hackettes [61]

Table 5.4. Performance indicators of the humidifier with hackettes [61]

Volume, m^3	G_a , kg/h	G_{fw} , kg/h	MR	ER, kg/(m^3h)	ΔP_a , Pa/m
0.0072	20.16	0.41	0.6	57	39
	21.6	0.45	0.57	63	45
	23.04	0.48	0.53	67	52
	24.48	0.53	0.5	74	58
	25.92	0.5	0.47	69	65
	27.36	0.48	0.45	67	73

4. ABS plastic as a packing material [63]. Acrylonitrile Butadiene Styrene (ABS) plastic was investigated in [63] as an effective packing material for use in humidification-based desalination systems. Its key advantages include mechanical strength, excellent resistance to impact, wear and moisture, and relatively low cost, making it a promising choice for small-scale applications. The packing material examined in [63] has a specific surface area of $226 \text{ m}^2/\text{m}^3$ (Fig. 5.5) and is capable of withstanding temperatures up to 80°C , as specified by the manufacturer. The geometric parameters and construction

details of the humidifier filled with ABS plastic are provided in Section 3.1. The operational and energy performance characteristics are summarized in Table 5.5. The thermodynamic efficiency of the humidifier ranges from 0.7 to 0.9, while the average GOR value is 0.49.



Fig. 5.5. ABS plastic from [63]

Table 5.5. Performance indicators of the humidifier with ABS plastic [63]

Volume, m^3	$G_a, \text{kg/h}$	$G_{fw}, \text{kg/h}$	MR	ER, $\text{kg}/(\text{m}^3\text{h})$	GOR	η_{hum}
0.5	72.7	5.2	2.34	10.5	0.8	0.725
	61.9	5	2.75	10.1	0.75	0.77
	48.6	4.7	3.5	9.5	0.65	0.85
	41	4.4	4.15	8.9	0.62	0.87
	27.4	3.5	6.22	7.1	0.46	0.9

5. Rushing packing from [83]. Raschig rings represent a classical type of packing material characterized by their simple cylindrical shape with a height-to-diameter ratio of 1:1 (Fig. 5.6).



Fig. 5.6. Rushing packing from [83].

Due to their durability and cost-effectiveness, Raschig rings are widely employed in the mass transfer processes. In the study [83], the humidifier tower with a height of 1 m and a diameter of 0.25 m was filled with metal Raschig rings. The total volume of the packing material amounted to 0.2 m³. The operating conditions and energy performance characteristics of the humidifier equipped with rushing packing are presented in Table 5.6.

Tabla 5.6. Performance indicators of the humidifier with rushing packing from [83].

Volume, m ³	G_a , kg/h	G_{fw} , kg/h	MR	ER, kg/(m ³ h)
0.2	202	14.4	1.65	71
	233	16.7	1.43	82
	264	18.6	1.27	92
	202	15.8	2.51	78
	233	18	2.18	89
	264	20.4	1.92	101

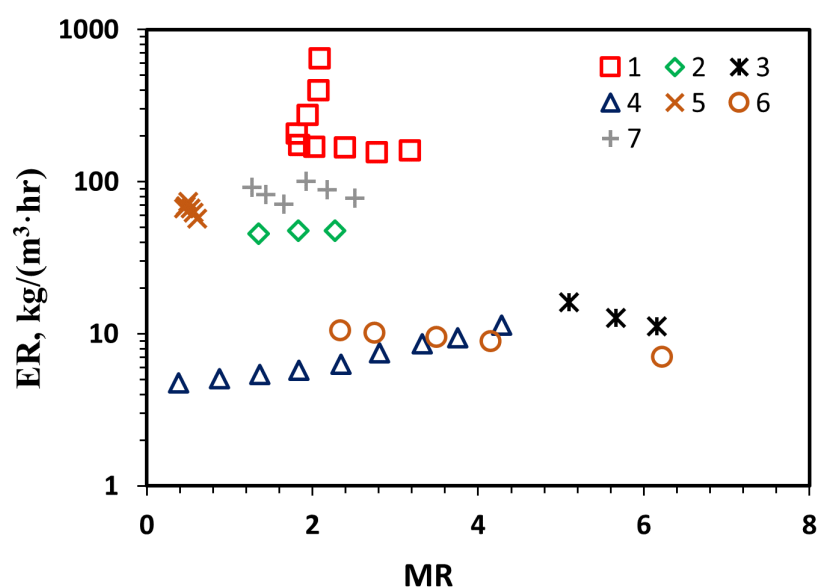


Fig. 5.7. Comparison of the evaporation rate of the packed bed humidifiers:
1 – film type; 2 – cellulose pads, [78]; 3 – honeycomb cellulose paper, [65]; 4 – paddy grass, [60]; 5 – hackettes, [61]; 6 – ABS plastic, [63]; 7 – rushing packing, [83].

Let us compare the performance indicators of the film humidifier with those of the packing materials described above. Figure 5.7 illustrates the variation in evaporation rate

(ER) as a function of the mass flow ratio (MR). It can be observed that across the entire MR range, paddy grass, ABS plastic and honeycomb cellulose paper exhibit the lowest ER values, which are nearly $10 \text{ kg}/(\text{m}^3 \cdot \text{h})$. Humidifiers with cellulose pads, hackettes and rushing packing have ER values around $100 \text{ kg}/(\text{m}^3 \cdot \text{h})$. The highest ER values – exceeding $600 \text{ kg}/(\text{m}^3 \cdot \text{h})$ – are achieved by the proposed film humidifier when the inlet water temperature is 60°C . Considering a typical inlet water temperature range of $30\text{--}60^\circ\text{C}$, which corresponds to the operating conditions of HDH systems with solar water heaters, the ER values for a film humidifier fall within the range of $200\text{--}800 \text{ kg}/(\text{m}^3 \cdot \text{h})$.

Therefore, a film humidifier demonstrates significantly higher evaporation rate (ER) values than those of all the other packing materials. This enhanced performance is attributed to the efficient utilization of the internal volume of the film humidifier as an active heat and mass transfer zone during the evaporation of moisture from water into air.

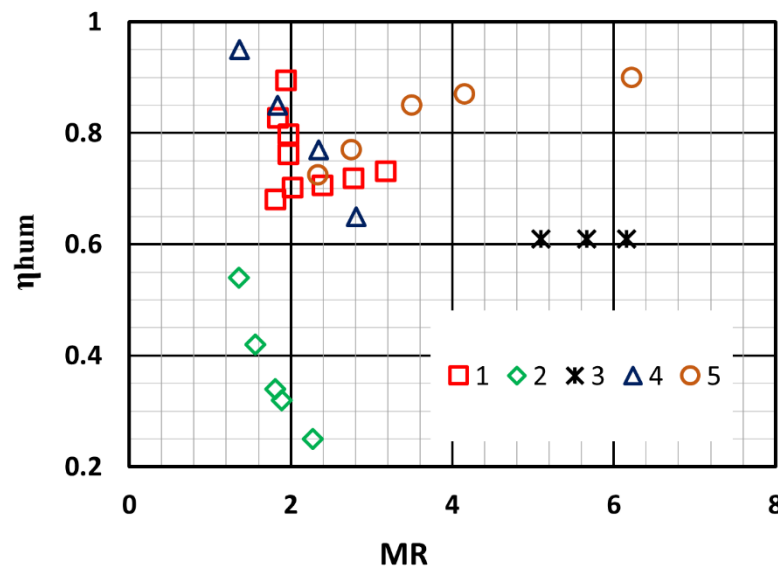


Fig. 5.8 Comparison of the thermodynamic efficiency of packed bed humidifiers:
 1 – film type; 2 – cellulose pads, [78]; 3 – honeycomb cellulose paper, [65];
 4 – paddy grass, [60]; 5 – ABS plastic.

Figure 5.8 illustrates the variation of thermodynamic efficiency as a function of the mass flow ratio (MR). Across the entire MR range, cellulose paper exhibits the lowest values of thermodynamic efficiency (η_{hum}), which is nearly 0.4. Slightly higher efficiency is observed for honeycomb cellulose paper, with $\eta_{hum} = 0.61$. The highest thermodynamic

efficiency (η_{hum}) is demonstrated by the film humidifier, paddy grass, while the ABS plastic shows the highest value (around 0.8). The maximum value of thermodynamic efficiency ($\eta_{hum} = 0.95$) is achieved using the natural packing material – paddy grass.

Thus, the film humidifier achieves a thermodynamic efficiency comparable to that of the best-performing packing materials, confirming the high effectiveness of heat and mass transfer processes in film humidifiers under the typical operating conditions of HDH systems.

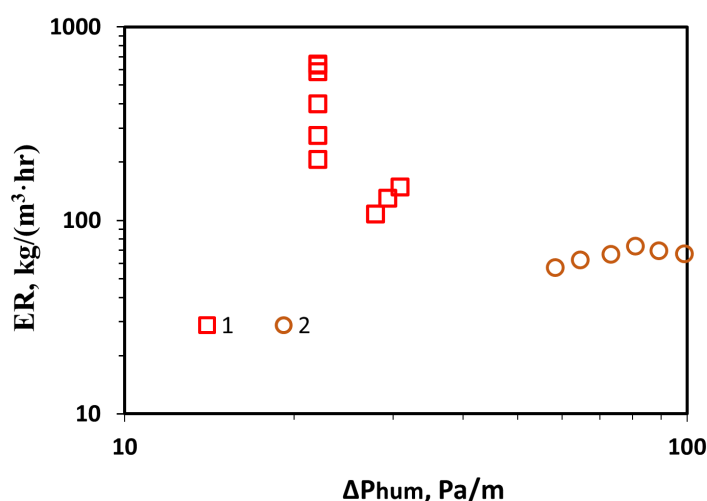


Fig. 5.9 Comparison of the air pressure drop of the packed bed humidifiers:
1 – film type; 2 – paddy grass, [60].

Figure 5.8 shows the variation in evaporation rate as a function of air pressure drop. It can be seen that paddy grass creates an aerodynamic resistance nearly four times higher than that of the film humidifier, while the film humidifier demonstrates significantly higher evaporation efficiency.

Thus, the film humidifier exhibits the lowest aerodynamic resistance among all the considered packing materials, which contributes to the reduced energy consumption of the fan supplying air through the humidifier in the HDH desalination system.

Based on the analysis of Figures 5.7 – 5.9, it can be concluded that under the typical operating parameters of HDH systems, the film humidifier achieves the highest evaporation rate, the lowest air pressure drop, and thermodynamic efficiency comparable to the best-performing packing materials commonly used in thermal desalination. Furthermore, the film humidifier has the lowest hydraulic losses on the water side, since

– unlike conventional packing materials – it does not require water spray nozzles for operation. The required water pressure is generated solely by lifting the water to a specified height within a supply tube.

5.2. Comparison of a Film Humidifier with Bubble Columns

Among the studies reviewed in Section 1.3, only two papers – [50] and [64] – investigating the operation of bubble column humidifiers provided comparable experimental conditions, where the water temperature, air temperature, and mass flow rate ratios are approximately the same as in the current research.

In study [50], the humidifier was constructed using a mild steel sheet with a surface area of 0.09 m^2 and a height ranging from 0.5 m at one end to 0.6 m at the other end. It provided an inclined top cover that channeled the condensate to the distillate collection tray. A bubble column with a diameter of 0.039 for air supply was installed at a height of 0.12 m from the humidification chamber bottom. Saline water was fed into the humidifier column from a storage tank. The humidifier was connected to the dehumidifier via a 0.076 m diameter pipe. Fins were attached to the bottom of the humidifier (Fig. 5.10) at uniform intervals to enhance the heat absorption rate from the combustion chamber. The humidifier is insulated with jute rope to minimize heat losses.

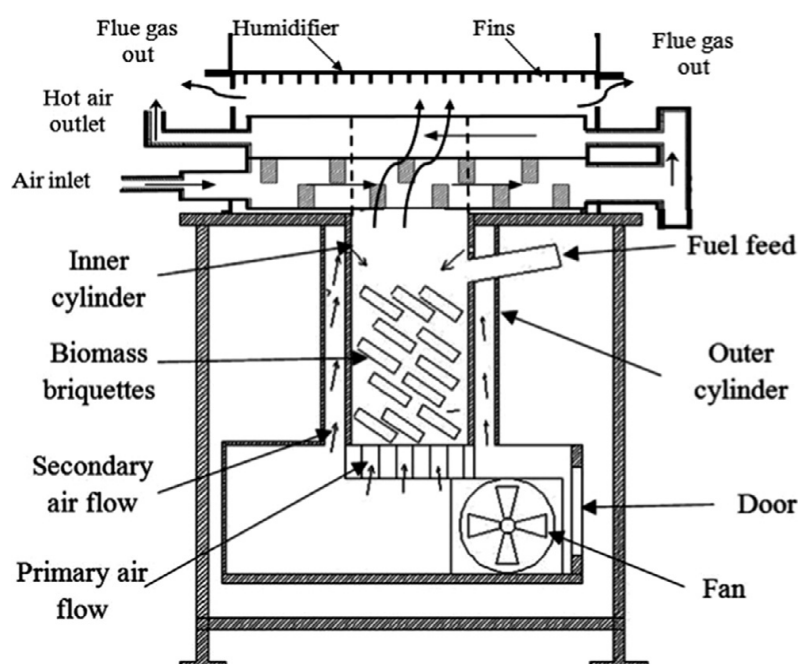


Fig. 5.10. Bubble column from [50].

For comparison, we selected the data corresponding to the optimal humidifier geometry (water column height of 160 mm, bubble column orifice diameter of 1 mm), and the optimal operating parameters of HDH systems (cooling water flow rate of 209 kg/h, inlet water temperature of 60 °C). The operating parameters and energy performance characteristics of the humidifier under these conditions are presented in Table 5.7.

Table 5.7. Performance indicators of a bubble column humidifier [50].

Volume, m ³	G _a , kg/h	G _{fw} , kg/h	MR	ER, kg/(m ³ h)	ΔP_a , kPa/m	η_{hum}
0.015	50.4	5.35	4.1	372	7	0.915
	54	5.15	3.9	357	9	0.925
	57.6	5.8	3.6	403	11	0.93
	61.2	6	3.4	417	13	0.94
	64.8	6.15	3.2	427	15	0.97

The geometric dimensions and description of a two-stage bubble column humidifier investigated in [64] are presented in Section 3.1. The optimal operating parameters and energy performance characteristics of the humidifier are provided in Table 5.8.

Table 5.8. Performance indicators of a bubble column humidifier from [64].

Volume, m ³	G _a , kg/h	G _{fw} , kg/h	MR	ER, kg/(m ³ h)	GOR	SEC, kWh/kg
0.00125	2	0.38	-	306	0.33	2.36

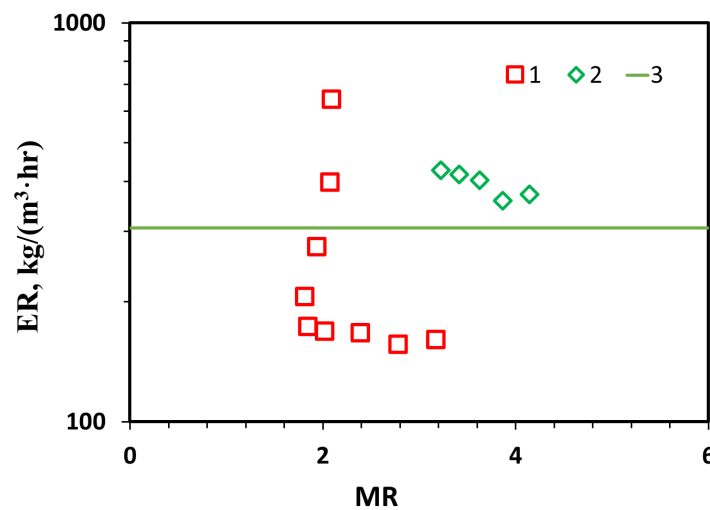


Fig. 5.11 Comparison of the evaporation rate of bubble columns:

1 – film type; 2 – biomass bubble column [50]; 2 – two-stage bubble column [64].

Let us compare the performance indicators of the film humidifier with those of the bubble column humidifiers described above. Figure 5.11 shows the variation of the evaporation rate as a function of the mass flow ratio. It can be seen that the ER values for the bubble column humidifiers are significantly higher than those of the packed bed humidifiers (Fig. 5.7) and are comparable to those of the film humidifier – around $300 \text{ kg}/(\text{m}^3 \cdot \text{h})$. This indicates equally high efficiency in utilizing the physical volume of both bubble column and film humidifiers for heat and mass transfer.

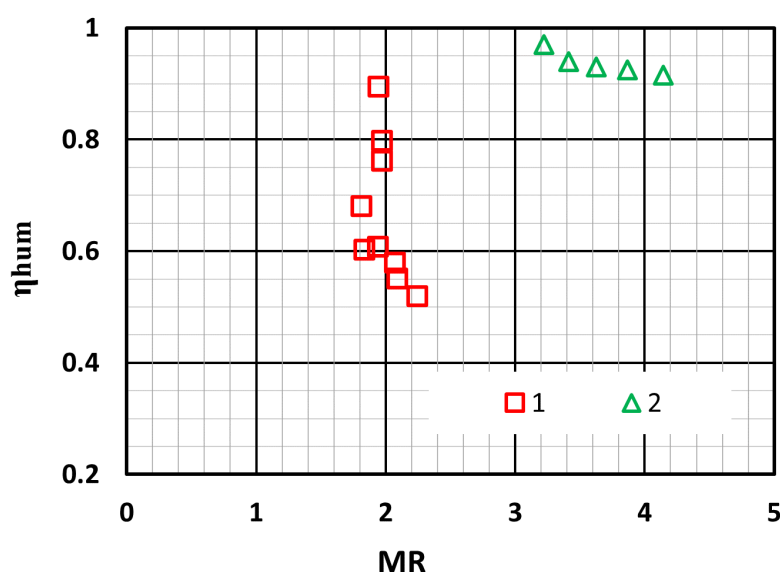


Fig. 5.12 Comparison of the thermodynamic efficiency of bubble columns:

1 – film type; 2 – biomass bubble column [50].

Figure 5.12 illustrates the variation of thermodynamic efficiency concerning the mass flow ratio. It is evident that the bubble column demonstrates the highest η_{hum} values, approaching 1. On average, the thermodynamic efficiency of the film humidifier is approximately 20% lower.

Thus, bubble columns provide a higher rate of heat and mass transfer between air and hot water. This is attributed to the intensive contact between air and fine water bubbles, which creates a large interfacial area and promotes effective air humidification.

Figure 5.13 shows the change in evaporation rate as a function of air pressure drop. It is clear that to achieve the same level of evaporation efficiency, the aerodynamic

The geometric dimensions and description of the rotating humidifier studied in [62] are provided in Section 3.1. The design features of the humidifier are shown in Figure 1.22. The operating parameters and energy performance characteristics are presented in Table 5.9.

Table 5.9. Energy performance characteristics of a rotating humidifier [62].

Volume, m ³	G _a , kg/h	G _{fw} , kg/h	MR	ER, kg/(m ³ h)
0.36	11.5	1.24	1.2	3.43
	158.4	0.84	1.3	2.33
	136.8	0.64	1.6	1.77
	111.6	0.5	2.0	1.3
	90	0.46	2.7	1.27

A multi-string humidifier studied in [51] consists of a vertical acrylic cylindrical air duct with an internal diameter of 6.35 cm, an upper water reservoir, a lower chamber with flow conditioners to ensure uniform air distribution, and a square array of 24 cotton strings with a radius of 0.375 mm (Fig. 5.14). The spacing between the strings is 10 mm. All the strings are fixed to a metal rod to maintain tension. A circulating bath is used to heat the feed water and pump it into the upper reservoir. The heated liquid is split into several streams using a row of nozzles embedded in the upper tank. As the liquid flows downward along the strings under the gravity, it forms moving liquid beads due to inherent instabilities caused by the interaction of surface tension, viscosity, gravity, and inertia forces. The operating parameters and energy performance characteristics of the humidifier are presented in Table 5.10.

Table 5.10. Energy performance characteristics of the multi-string humidifier from [51].

Volume, m ³	G _a , kg/h	G _{fw} , kg/h	MR	ER, kg/(m ³ h)	ΔP_a , Pa/m	η_{hum}
-	4.1	-	2.1	198	0.17	0.62
	6.1		1.4	220	0.25	
	8.1		1.0	246	0.36	
	10.2		0.85	258	0.54	
	12.1		0.71	280	0.72	

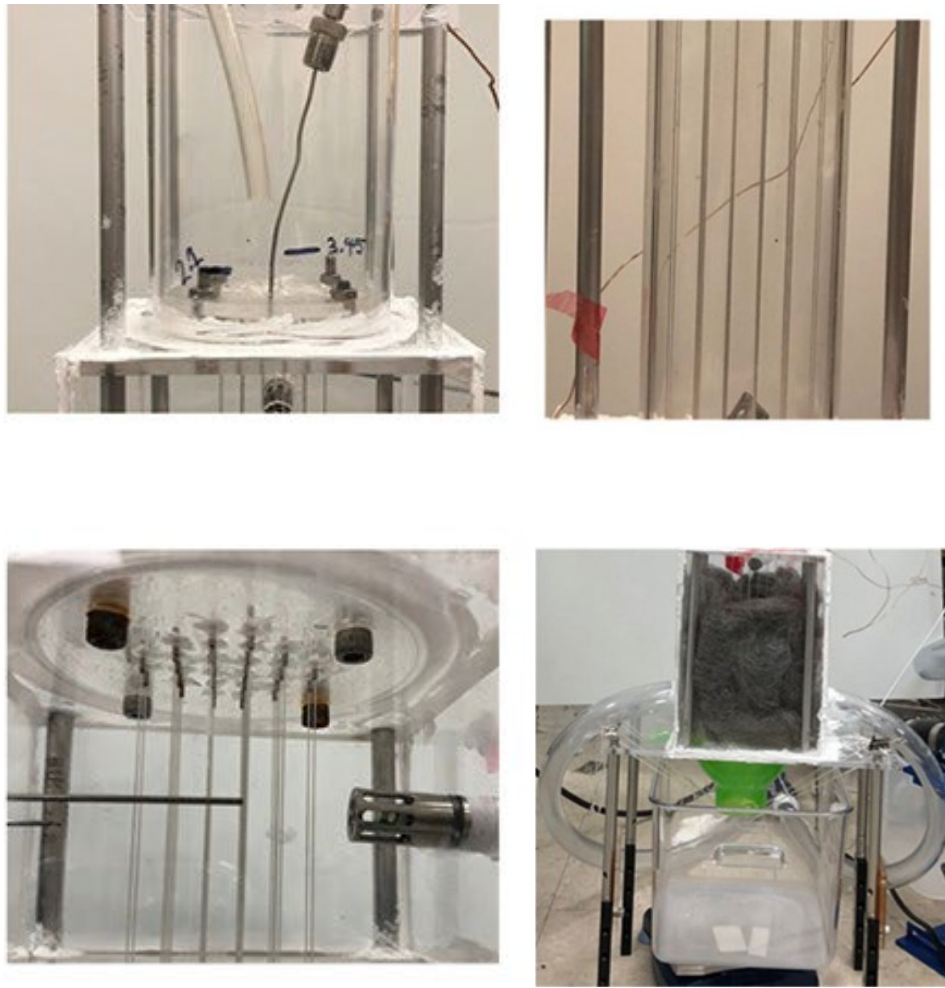


Fig. 5.14. Schematic of a multi-string humidifier [51].

The geometric dimensions and description of an ultrasonic humidifier studied in [57] are provided in Section 3.1. The design features of the humidifier are shown in Figure 1.16. The operating parameters and energy performance characteristics of the humidifier are presented in Table 5.11.

Table 5.11. Energy performance characteristics of the ultrasonic humidifier [57].

Volume, m^3	G_a , kg/h	G_{fw} , kg/h	MR	ER, kg/(m^3h)
0.024	32.4	0.72	2.78	30.6
	36	0.77	2.5	32.5
	39.6	0.96	2.27	40.5
	46.8	0.92	1.92	38.8
	50.4	0.91	1.79	38.4
	57.6	0.84	1.56	35.4
	61.2	0.76	1.47	32.0

The geometric dimensions and description of a porous humidifier studied in [58] are provided in Section 3.1. The design features of the humidifier are shown in Figure 1.17. The operating parameters and energy performance characteristics of the humidifier are presented in Table 5.12.

Table 5.12. Energy performance characteristics of a porous humidifier [58].

Volume, m ³	G_a , kg/h	G_{fw} , kg/h	MR	ER, kg/(m ³ h)
0.16	20.52	0.35	3.86	2.2
	30.96	0.52	2.56	3.3
	41.4	0.74	1.91	4.7
	51.84	0.58	1.53	3.7
	62.28	0.46	1.27	2.9

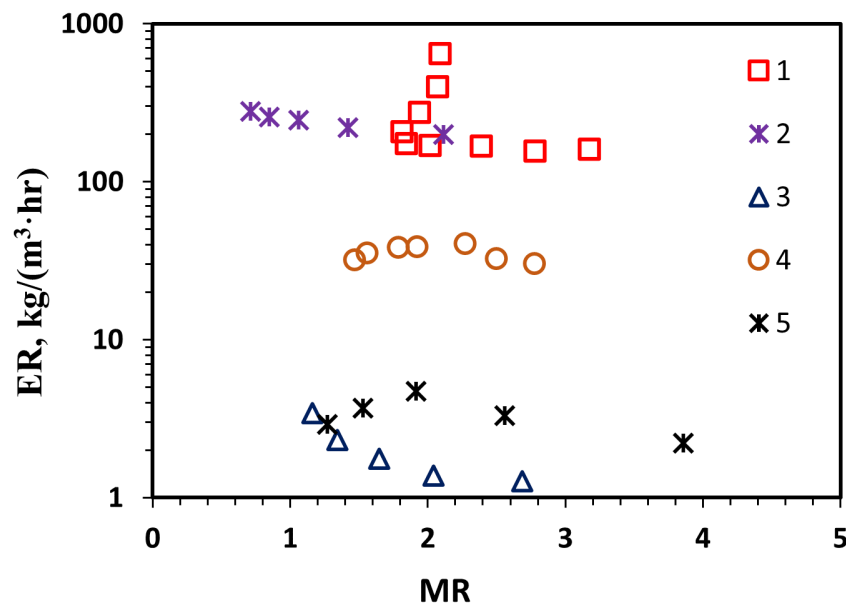


Fig. 5.15 Comparison of the evaporation rate of atypical humidifiers: 1 – film type; 2 – multi-string [51]; 3 – rotating [62]; 4 – ultrasonic [57]; 5 – porous [58].

Let us compare the performance indicators of the film humidifier with that of the atypical designs described above. Figure 5.15 shows the variation of the evaporation rate (ER) depending on the mass flow ratio (MR). It is evident that across the entire MR range, the rotating and porous designs demonstrate the lowest ER values – approximately 4-5 kg/(m³·h). An ultrasonic humidifier shows *ER* values of around 40 kg/(m³·h).

The ER values for the multi-string humidifier are on the same level as those for the film humidifier – around 200-300 kg/(m³·h). It is worth noting that in [51], the multi-string humidifier was studied at the inlet water temperature of 90 °C, whereas the proposed film humidifier was rested at 60 °C. In addition, the ER values of atypical designs (except for the multi-string) are significantly lower than those of the packed bed materials (Fig. 5.7) and bubble columns (Fig. 5.11). This calls into question the feasibility of complicating humidifier designs without a substantial improvement in their performance.

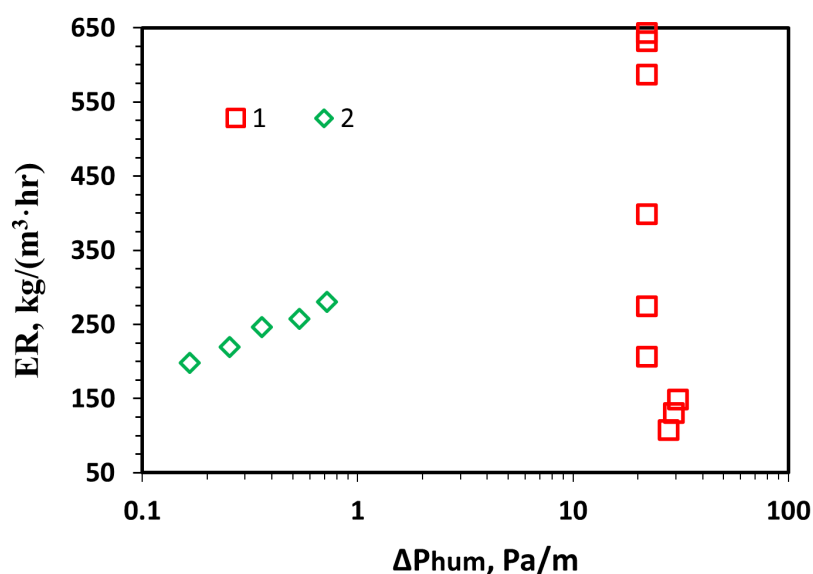


Fig. 5.16. Comparison of the air pressure drop of multi-string and film humidifiers:
1 – film type; 2 – multi-string [51].

Figure 5.16 demonstrates the variation of the evaporation rate depending on the air pressure drop. It can be seen that the multi-string humidifier generates the lowest aerodynamic resistance among all humidifier designs. At the same time, the evaporation efficiency of the film humidifier is 2.5 times higher.

Based on the analysis of Figures 5.15-5.16 and the data from Tables 5.9-5.12, it can be concluded that under typical operating conditions of HDH systems, the multi-string humidifier demonstrates the performance comparable to that of the film humidifier. Other atypical designs significantly underperform not only compared to the film humidifier, but also to packed bed humidifiers and bubble columns. Furthermore, their use is associated with increased energy consumption of the system.

5.4. Conclusions to Chapter 5

1. A comparison of the energy efficiency indicators of different types of humidifiers has shown that the film humidifier demonstrates the highest ER across the entire range of MR variations.

2. Compared to the packed bed humidifiers, the film humidifier has exhibited the lowest air pressure drop, the smallest hydraulic losses on the water side, and comparable thermodynamic efficiency.

3. In comparison with bubble column humidifiers, the film humidifier has also demonstrated the lowest air pressure drop. However, it lagged behind in thermodynamic efficiency due to more intensive heat and mass transfer processes in bubble columns.

4. The multi-string humidifier has shown the performance closest to that of the film humidifier. In contrast, other atypical designs (rotating, porous, ultrasonic, etc.) significantly underperformed not only compared to the film humidifier, but also to conventional contact heat exchangers with packing materials and bubble columns. Moreover, their application is associated with increased energy consumption, which reduces the overall efficiency of HDH systems.

CONCLUSIONS

The dissertation presents a comprehensive study of the energy performance characteristics of a film-type contact heat exchanger and determines their influence on the efficiency of air humidification under typical operating conditions of thermal water desalination systems. The obtained results have allowed the following conclusions to be drawn:

1. A comparative analysis of existing contact heat exchanger designs within HDH systems has been performed. It is established that current humidifier designs are characterized by significant pressure losses and high energy consumption, which reduces the overall efficiency of thermal desalination systems. It is shown that one of the key directions for improving the efficiency of such systems is the optimization of heat and mass transfer processes in humidifiers, as these have a decisive impact on the productivity and energy efficiency of thermal water desalination systems.

2. An experimental setup was developed to study the process of air humidification in a film-type contact heat exchanger. The implemented monitoring system, based on *Regmik* measurement and control equipment, has provided continuous recording of operating parameters in thermal desalination systems and enabled an objective assessment of the energy performance characteristics of the film-type humidifier. An analysis of the maximum deviations (uncertainties) between experimental and calculated data confirms the reliability of the obtained results and the adequacy of the applied experimental methodology.

3. Optimal operating parameters for the tube film-type humidifier have been established. At an air superficial phase velocity of $j_a = 0,34$, a water-to-air mass flow rate ratio of $MR = 2$, and an inlet water temperature to the humidifier of $t_{w,in} = 60$ °C, the HDH system achieves maximum productivity with minimal water and air pressure losses, minimum energy consumption, and without condensate contamination with water droplets.

4. A thermodynamic model of the tube film-type humidifier has been developed based on the heat and mass transfer equation, incorporating new empirical dependencies

suitable for practical application in HDH systems. The simulation results have shown that the highest performance is achieved with a tube height of 1 m and a diameter of 50 mm, which ensure the minimum energy consumption.

5. The developed calculation method can be applied for the engineering design of the film-type humidifiers, techno-economic analysis, and optimization of their operating regimes in water desalination systems, air-conditioning systems, or heat recovery applications.

6. A comparison of the energy efficiency indicators of different types of humidifiers show that the film humidifier demonstrates the highest ER across the entire range of MR variations. Moreover, the pressure losses for water and air are the lowest, 22.3 kPa and 25 Pa/m, respectively. Thus, using a vertical tube as a humidifier in the HDH system will reduce the desalination unit power and specific energy consumption.

7. The results of the dissertation research have been tested in the course of designing HDH desalination systems at China Hydrogen Energy Group Co., Ltd and Liaoning Hongsheng Environmental Solutions Technology Co., Ltd.

REFERENCES

1. Amidpour, M., Salimi, M., He, W. (2024). Chapter 1 – Need for low-grade heat-driven desalination systems. *Advances in Sustainable Humidification-Dehumidification Thermal Desalination Systems*, 1-15. doi:10.1016/B978-0-323-95658-1.00001-6.
2. International research center of big data for sustainable development goals. (2024). *Big earth data in support of the sustainable development*. doi:10.12237/casearth. CBAS2024P01.
3. He, C., Liu, Z., Wu, J., Pan, X., Fang, Z., Li, J., Bryan, B. (2021). Future global urban water scarcity and potential solutions. *Nature Communications*, 12, 4667. doi:10.1038/s41467-021-25026-3.
4. She, Y., Chen, J., Zhou, Q., Wang, L., Duan, K., Wang, R., Qu, S., Xu, M., Zhao, Y. (2024). Evaluating losses from water scarcity and benefits of water conservation measures to intercity supply chains in China. *Environmental Science & Technology*, 58(2), 1119–1130. doi: 0.1021/acs.est.3c07491.
5. Hu, T., Zhang, T., Wang, X., Du, S., Sun, W., Zhang, X. (2023). Optimizing the layout of major productive forces in the new development stage: its feature, key mission and stratagic measures. *Regional Economic Review*, 62(2).
6. Hu, M., Ma, R., Cao, Z., Xiong, J., Xue, K. (2021). Remote estimation of trophic state index for inland waters using landsat-8 oli imagery. *Remote Sensing*, 13(10). doi:10.3390/rs13101 988.
7. Zheng, X. (2025). Water recycling and water-saving measures in urban water system planning. *China Resources Comprehensive Utilization*, 43(5). doi:10.3969/j.issn.1008-9500.2025.05.046.
8. Liu, W., Zhang, Y., Xu, R., Zhang, Z. (2022). Water shortage risk evaluation and its primary cause. *Empirical evidence from rural China*, 46(2). doi:10.1111/1477-8947.12249.
9. Wang, H., Xu, X., Cheng, J., Zhou, Z., Chu, J., Zhang, J. (2023). Basing four aspects on water resources in water resources protection and utilization: basic

- cognition and key technology system. *Water Resources Protection*, 39(1), 1-7. doi: 10.3880/j.issn.1004-6933.2023.01.001.
10. Huang, Y., Huang, X., Xie, M., Cheng, W., Shu, Q. (2021). A study on the effects of regional differences on agricultural water resource utilization efficiency using super-efficiency SBM model. *Scientific Reports*, 11, 9953. doi: 10.1038/s41598-021-89293-2.
 11. Chu, W., Yang, X., Xiao, R. Jin, W. (2022). Research on the strategies for safe management of drinking water in the Yangtze river delta. *Strategic Study of CAE*, 24(5), 19–25. doi:10.15302/J-SSCAE-2022.05.003.
 12. Sun, S., Chen, Y., Lim, Y., An, D. (2018). Occurrence, spatial distribution and seasonal variation of emerging trace organic pollutants in source water for Shanghai, China. *Science of the Total Environment*, 639, 1–7. doi: 10.1016/j.scitotenv.2018.05.089.
 13. He, Y. (2022). Coordinated legislation on drinking water source quality safety and substantive systems in the Yangtze River Delta Demonstration Area. *Environmental pollution and prevention*, 44(2), 278–284. doi:10.15302/J-SSCAE-2022.05.003.
 14. Li, L., Liu, X., Zhang, X. (2021). Public attention and sentiment of recycled water: Evidence from social media text mining in China. *Journal of Cleaner Production*, 303(20), 126814. doi:10.1016/j.jclepro.2021.126814.
 15. Shirish K, P., Kalpesh V, M. (2020). Techniques to improve the performance of enhanced condensation area solar still: a critical review. *Journal of Cleaner Production*, 268. doi:10.1016/j.jclepro.2020.122260.
 16. Mohsenzadeh, M., Lu, A., Christopher, P. (2021). A review on various designs for performance improvement of passive solar stills for remote areas. *Solar Energy*, 228, 594-611. doi:10.1016/j.solener.2021.09.086.
 17. Shoeibi, S., Rahbar, N., Abedini, A., Kargarsharifabad, H. (2021). A comprehensive review of enviro-exergo-economic analysis of solar stills. *Renewable and Sustainable Energy Reviews*, 149. doi:10.1016/j.ser.2021.111404.

18. AbdelMeguid, H. (2025). Examining the performance of optically optimized solar stills with phase change materials: A theoretical perspective on ongoing debates. *Solar Energy Materials and Solar Cells*, 282, 113394. doi:10.1016/j.solmat.2024.113394.
19. AbdelMeguid, H., El Awady, W. M. (2024). Optimizing solar still performance through glass cover optical properties: A mathematical modeling and theoretical investigation. *Ain Shams Engineering Journal*, 15(3), 102589. doi:10.1016/j.asej.2023.102589.
20. AbdelMeguid, H., Gherissi, A., Elsayy, M., Aljohani, Z., Asiri, A., Saber, M., Fouda, A. (2024). Potential application of solar still desalination in NEOM region. *Applied Water Science*, 14, 53. doi:10.1007/s13201-024-02115-4.
21. Al-Hinai, H., Ali, B. (2002). Parametric investigation of a double-effect solar still in comparison with a single-effect solar still. *Desalination*, 150 (1), 75-83. doi:10.1016/S0011-9164(02)00931-1.
22. Ma, Q., Xu, Z., Wang, R. (2021). Distributed solar desalination by membrane distillation: current status and future perspectives. *Water Research*, 198, 117154. doi: 10.1016/j.watres.2021.117154.
23. Rasool, M., Banat, F. (2013). Desalination by solar powered membrane distillation systems. *Desalination*, 308, 186-197. doi:10.1016/j.desal.2012.01.021.
24. Cai, F., Guo, F. (2017). Study of mass transfer coefficient in membrane desalination. *Desalination*, 407, 46-51. doi:10.1016/j.desal.2016.12.013.
25. Ahmed, F.E., Lalia, B.S., Hashaikeh, R., Hilal, N. (2020). Alternative heating techniques in membrane distillation: A review. *Desalination*, 496, 114713. doi:10.1016/j.desal.2020.114713.
26. Bamasag, A., Alqahtani, T., Sinha, S., Ghaffour, N., Phelan, P. (2021). Solar-heated submerged vacuum membrane distillation system with agitation techniques for desalination. *Separation and Purification Technology*, 256, 117855. doi:10.1016/j.seppur.2020.117855.

27. Narayan, A., Pitchumani, R. (2020). Analysis of an air-cooled air gap membrane distillation module. *Desalination*, 475, 114179. doi:10.1016/j.desal.2019.114179.
28. Omar, A., Nashed, A., Li, Q., Taylor, R.A. (2021). Experimental and numerical evaluation of the energy requirement of multi-stage vacuum membrane distillation designs. *Separation and Purification Technology*, 257, 117303. doi:10.1016/j.seppur.2020.117303.
29. Shih, W., Rahardianto, A., Lee, R-W., Cohen, Y. (2005). Morphometric characterization of calcium sulfate dihydrate (gypsum) scale on reverse osmosis membranes. *Journal of Membrane Science*, 252(1-2), 253–263. doi:10.1016/j.memsci.2004.12.023.
30. Greenlee, L.F., Lawler, D.F., Freeman, B.D., Marrot, B., Moulin, P. (2009). Reverse osmosis desalination: water sources, technology, and today's challenges. *Water Research*, 43, 2317-2348. doi:10.1016/j.watres.2009.03.010.
31. Monnot, M., Carvajal, G.D.M., Laborie, S., Cabassud, C., Lebrun, R. (2018). Integrated approach in eco-design strategy for small RO desalination plants powered by photovoltaic energy. *Desalination*, 435, 246-258. doi:10.1016/j.desal.2017.05.015.
32. Ayoub, D.S., Ega, H.M., Coronas, A. (2022). A feasibility study of a small-scale photovoltaic-powered reverse osmosis desalination plant for potable water and salt production in Madura Island: a techno-economic evaluation. *Thermal Science and Engineering Progress*, 35(24), 101450. doi:10.1016/j.tsep.2022.101450.
33. Khan, M.A.M., Rehman, S., Al-Sulaiman, F.A. (2018). A hybrid renewable energy system as a potential energy source for water desalination using reverse osmosis: a review. *Renewable and Sustainable Energy Reviews*, 97, 456-477. doi: 10.1016/j.rser.2018.08.049.
34. Bhagwati, A., Shah, M., Prajapati, M. (2023). Emerging technologies to sustainability: a comprehensive study on solar desalination for sustainable development. *Sustainable Manufacturing and Service Economics*, 2, 100007. doi: 10.1016/j.smse.2022.100007.

35. Tashtoush, B., Al-Omari, J. (2023). Solar-assisted hybrid integration of humidification-dehumidification and forward osmosis for brackish water desalination: A parametric study. *Case Studies in Chemical and Environmental Engineering*, 8, 100500. doi:10.1016/j.cscee.2023.100500.
36. Karhe, Y. B., Walke, P. V. (2013). A solar desalination system using humidificationdehumidification process – a review of recent research. *International Journal of Modern Engineering Research*, 3(2), 962-969.
37. Velmurugan, V., Kumar, S. P., Ragul, S. (2018). Humidificaton-dehumidification desalination system – an overview. *International Journal of Scientific Research in Science and Technology*, 4(5), 1163-1177.
38. Sereda, V. V., Prytula, N. O. (2023). Energy performance of thermal desalation systems with humidifiers of different types. *Bulletin of Vinnytsia Polytechnic Institute*, 6, 14-22. doi:10.31649/1997-9266-2023-171-6-14-22.
39. Behnam, P., Arefi, A., Shafii, M. B. (2018). Exergetic and thermoeconomic analysis of a trigeneration system producing electricity, hot water, and fresh water driven by low-temperature geothermal sources. *Energy Conversion and Management*, 157, 266-276. doi:10.1016/j.enconman.2017.12.014.
40. Ariyanfar, L., Yari, M., Aghdam, E. A. (2016). Proposal and performance assessment of novel combined ORC and HDD cogeneration systems. *Applied Thermal Engineering*, 108, 296-311. doi:10.1016/j.applthermaleng.2016.07.055.
41. He, W. F., Han, D., Xu, L. N., Yue, C., Pu, W. H. (2016) Performance investigation of a novel water-power cogeneration plant (WPCP) based on humidification dehumidification (HDH) method. *Energy Conversion and Management*, 110, 184-91. doi:10.1016/j.enconman.2015.12.019.
42. He, W. F., Zhu, W. P., Han, D., Huang, L., Wu, Y. K., Zhang, X. K. (2017). Performance simulation of a power-water combined plant driven by low grade waste heat. *Energy Conversion and Management*, 145, 107-116. doi: 10.1016/j.enconman.2017.04.094.

43. He, W. F., Zhang, X. K., Han, D., Gao, L. (2017). Performance analysis of a water-power combined system with air-heated humidification dehumidification process. *Energy*, 130, 218-227. doi:/10.1016/j.energy.2017.04.136.
44. He, W. F., Han, D., Wen, T. (2018). Energy, entropy and cost analysis of a combined power and water system with cascade utilization of geothermal energy. *Energy Conversion and Management*, 174, 719-729. doi:10.1016/j.enconman.2018.08.089.
45. Mhamed, A. S., Ahmed, M. S., Maghrabie, H. M., Shahby. A. G. (2020). Desalination process using humidification–dehumidification technique: a detailed review. *International Journal of Energy Research*, 45(3), 3698-3749. doi: 10.1002/er.6111.
46. Zhang, Z., Han, D., Lu, Y., He, W. (2024). Off-design behaviors of a solar-powered hdh system for water and power cogeneration. *Applied Thermal Engineering*, 257, 124126. doi:10.1016/j.applthermaleng.2024.124126.
47. Lawal, D. W., Usman, J., Abba, S. I., Yogarathinam, L. T., Usman, A. G., Antar, M. A., Aljundi, I. H., Zubair, S. M. (2024). Effective design of sustainable energy productivity based on the experimental investigation of the humidification-dehumidification-desalination system using hybrid optimization. *Energy Conversion and Management*, 319, 118942. doi:10.1016/j.enconman.2024.118942.
48. Kabeel, A. E., Hamed, M. H., Omara, Z. M., Sharshir, S. W. (2014). Experimental study of a humidification-dehumidification solar technique by natural and forced air circulation. *Energy*, 68, 218–228. doi:10.1016/j.energy.2014.02.094.
49. Sereda, V. V., Solomakha, A. S., Pritula, N. O., Zabolotny O. A. (2021). Thermodynamical analysis of thermal dessery plant with air humidification-drying cycle. *Materials science and mechanical engineering*, 69. doi:10.20535/kpissn.2021.4.250663.
50. Rajaseenivasan, T., Srithar, K. (2017). An investigation into a laboratory scale bubble column humidification dehumidification desalination system powered by

- biomass energy. *Energy Conversion and Management*, 139, 232–244. doi: 10.1016/j.enconman.2017.02.043.
51. Zeng, Z., Sadeghpour, A., Ju, Y.S. (2019). A highly effective multi-string humidifier with a low gas stream pressure drop for desalination. *Desalination*, 449, 92–100. doi: 10.1016/j.desal.2018.10.017.
52. Eder, E., Preißinger, M. (2020). Experimental analysis of the humidification of air in bubble columns for thermal water treatment systems. *Experimental Thermal and Fluid Science*, 115, 110063. doi:10.1016/j.expthermflusci.2020.110063.
53. Eder, E., Hiller, S., Brüggemann, D., Preißinger, M. (2022). Characteristics of air–liquid heat and mass transfer in a bubble column humidifier. *Applied Thermal Engineering*, 209, 118240. doi:10.1016/j.applthermaleng.2022.118240.
54. Rahimi-Ahar, Z., Hatamipour, M. S., Ghalavand, Y. (2018). Experimental investigation of a solar vacuum humidification-dehumidification (VHDH) desalination system. *Desalination*, 437, 73–80. doi:10.1016/j.desal.2018.03.002.
55. Rahimi-Ahar, Z., Hatamipour, M. S., Ghalavand, Y., Palizvan, A. (2020). Comprehensive study on vacuum humidification-dehumidification (VHDH) desalination. *Applied Thermal Engineering*, 169, 114944. doi:10.1016/j.applthermaleng.2020.114944.
56. Aref, L., Fallahzadeh, R., Madadi Avargani, V. (2021). An experimental investigation on a portable bubble basin humidification/dehumidification desalination unit utilizing a closed-loop pulsating heat pipe. *Energy Conversion and Management*, 228, 113694. doi:10.1016/j.enconman.2020.113694.
57. El-Said, E. M. S., Dahab, M. A., Omara, M., Abdelaziz, G. B. (2021). Solar desalination unit coupled with a novel humidifier. *Renewable Energy*, 180, 297–312. doi: 10.1016/j.renene.2021.08.105.
58. El-Said, E. M. S., Dahab, M.A., Omara, M., Abdelaziz, G. B. (2022). Humidification-dehumidification solar desalination system using porous activated carbon tubes as a humidifier. *Renewable Energy*, 187, 657–670. doi:10.1016/j.renene.2022.01.023.

59. Abdelaziz, G.B., Dahab, M.A., Omara, M.A., Sharshir, S. W., Elsaid, A. M., El-Said, E. M. S. (2022). Humidification dehumidification saline water desalination system utilizing high frequency ultrasonic humidifier and solar heated air stream, *Thermal science and engineering progress*, 27, 101144. doi:10.1016/j.tsep.2021.101144.
60. Thanaiah, K., Gumtapure, V., Mitiku Tadesse, G. (2021). Experimental analysis on humidification-dehumidification desalination system using different packing materials with baffle plates. *Thermal Science and Engineering Progress*, 22, 100831. doi:10.1016/j.tsep.2020.100831.
61. Soomro, S. H., Santosh, R., Bak, C., Yoo, C., Kim, W., Kim, Y. (2022). Effect of humidifier characteristics on performance of a small-scale humidification-dehumidification desalination system. *Applied Thermal Engineering*, 210, 118400. doi:10.1016/j.applthermaleng.2022.118400.
62. Khalaf-Allah, R. A., Abdelaziz, G. B., Kandel, M. G., Easa, A. S. (2022). Development of a centrifugal sprayer-based solar HDH desalination unit with a variety of sprinkler rotational speeds and droplet slot distributions. *Renewable energy*, 190, 1041-1054. doi:10.1016/j.renene.2022.04.019.
63. Garg. K., Beniwal. R., Das, S. K., Tyagi. H. (2023). Experimental investigation of a low-cost humidification-dehumidification desalination cycle using packed-bed humidifier and finned-tube heat exchanger. *Thermal Science and engineering progress*, 41, 101858. doi:10.1016/j.tsep.2023.101858.
64. Khan, M., Faizan, M., Antar, M. A., Khalifa, A. E. (2023). Experimental study on optimum performance of two-stage air-heated bubble-column humidification–dehumidification system. *Water S.A.*, 49(4), 374–386. doi:10.17159/wsa/2023.v49.i4.4009.
65. Shaikh, J. S, Ismail, S. (2023). Performance evaluation of a solar humidification dehumidification desalination system employing a multistage bubble column dehumidifier. *Solar Energy*, 263, 111933. doi:10.1016/j.solener.2023.111933.

66. Official website of Regmik [Online]. Available: <https://regmik.ua>. [Accessed: Aug. 13, 2025].
67. Bell, I. H., Wronski, J., Quoilin, S., Lemort, V. (2014). CoolProp: An open-source thermophysical property library. *Industrial & Engineering Chemistry Research*, 53(6), 2498–2508. <https://coolprop.org>.
68. Tsay, Y. L. (1994) Analysis of heat and mass transfer in a countercurrent-flow wet surface heat exchanger. *Heat and Fluid Flow* 15(2), 149-156. doi:10.1016/0142-727X(94)90069-8.
69. Feddaoui, M., Mir, A., Belahmidi, E. (2003) Cocurrent turbulent mixed convection heat and mass transfer in falling film of water inside a vertical heated tube. *International Journal of Heat and Mass Transfer*, 46 (18), 3497-3509. doi: 10.1016/S0017-9310(03)00129-7
70. Barabash, P., Solomakha A., Sereda V. (2023). Heat and mass transfer of countercurrent air-water flow in a vertical tube. *Heat Mass Transfer*, 59, 1343–1351. doi:10.1007/s00231-023-03342-2.
71. Voloshchuk, V., Gullo, P., Nikiforovich E., Buyak, N. (2021). Simulation and exergy analysis of a refrigeration system using an open-source web-based interactive tool, *Applied Sciences*, 11(23), 11535. doi:10.3390/app112311535.
72. Nematollahi, F., Rahimi, A., Gheinani T. T. (2013). Experimental and theoretical energy and exergy analysis for a solar desalination system. *Desalination*, 317, 23-31. doi:10.1016/j.desal.2013.02.021.
73. Holman, J. P. (2001). *Experimental methods for engineers* (8th ed.). New York, NY: McGraw-Hill., *Experimental Methods for Engineers*, eighth ed., McGraw Hill.
74. Barabash, P., Solomakha, A., Sereda, V. (2020). Experimental investigation of heat and mass transfer characteristics in direct contact exchanger. *International Journal of Heat and Mass Transfer*, 162, 120359. doi:10.1016/j.ijheatmasstransfer.2020.120359.
75. Bezrodnyi, M. K., Barabash, P. A., Goliiad, N. N. (2017). *Hidrodynamic i kontaktni teplo masoobmin v hazoridynnykh systemakh* [Hydrodynamics and interfacial heat and mass transfer in gas–liquid systems] (2nd ed., revised and

enlarged). Kyiv, Ukraine: Igor Sikorsky Kyiv Polytechnic Institute, Politekhnik. ISBN 978-966-622-856-3.

76. Schmidt, H. (2010). L2.5 Two-phase gas–liquid flow. In VDI Heat Atlas (VDI-Buch, pp. 1164-1168). Berlin, Heidelberg: Springer. doi:10.1007/978-3-540-77877-6_78.

77. Jeong, J. H., No, H. C. (1994). Classification of flooding data according to type of tube-end geometry. *Nuclear Engineering and Design*, 148(1), 109–117. doi:10.1016/0029-5493(94)90246-1.

78. Zubair, S. M., Antar, M. A., Elmutasim, S. M., Lawal, D. U. (2018). Performance evaluation of humidification-dehumidification (HDH) desalination systems with and without heat recovery options: An experimental and theoretical investigation. *Desalination*, 436, 161–175. doi:10.1016/j.desal.2018.02.018.

79. Park, I., Mudawar, I. (2013). Climbing film, flooding and falling film behavior in upflow condensation in tubes. *International Journal of Heat and Mass Transfer*, 65, 44-61. doi:10.1016/j.ijheatmasstransfer.2013.05.065.

80. Sereda, V., Solomakha, A., Prytula, N., Shvets, N. (2022). Thermodynamical analysis of the thermal water desalination system with open and closed air cycle. *Scientific notes of the V.I. Vernadsky TNU. Series: Technical Sciences*, 33(72), 146-152. doi:10.32782/2663-5941/2022.6/25.

81. Sharqawy, M. H., Antar, M. A., Zubair, S. M., Elbashir, A. M. (2014). Optimum thermal design of humidification dehumidification desalination systems. *Desalination*, 349, 10-21. doi:10.1016/j.desal.2014.06.016.

82. Sereda, V., Liu, Y., Podstievaia, T. (2023). Highly effective direct contact humidifier for thermal desalination system. *Power engineering: economics, technique, ecology*, 73(3), 131-138. doi:10.20535/1813-5420.3.2023.289729.

83. Zarei, T., Miroliaei, M. R. (2022). Performance evaluation of an HDH desalination system using direct contact packed towers: experimental and mathematical modeling study. *Water Reuse*, 12 (1), 92–110. doi:10.2166/wrd.2022.095.

APPENDIX A: List of Publications

1. Barabash, P., Solomakha, A., Sereda, V., Prytula, N., Strynada, P., **Liu, Y.** (2023). Heat and mass transfer of countercurrent air-water flow in a vertical tube. *Heat Mass Transfer*, 59, 1343–1351. <https://doi.org/10.1007/s00231-023-03342-2> (SCOPUS Q2).
2. Середя, В., **Лю, Я.**, Подстєвая, Т. (2023). Високоєфективний контактний зволожувач для термічної опріснювальної установки. *Енергетика: економіка, технології, екологія*, 73(3), 131-138. doi:10.20535/1813-5420.3.2023.289729 (фахова, категорія Б).
3. Середя, В., **Лю, Я.**, Подстєвая, Т. (2025). Експериментальне дослідження оптимальної продуктивності плівкового зволожувача для термічної системи опріснення. *Refrigeration Engineering and Technology*, 61(1), 25-36. doi:10.15673/ret.v61i1.3135 (фахова, категорія Б).
4. Solomakha, A., Strynada, P., Barabash, P., Sereda, V., Prytula, N., **Liu, Y.** (2022). Mass transfer at fluid and gas countercurrent flow in vertical tubes. *International Conference of Young Scientists on Energy and Natural Sciences Issues: proceedings of the 18th International Conference* (pp. 406-409), May 24–27, 2022, Kaunas, Lithuania. Published by Lithuanian Energy Institute, 2022. ISSN 2783-6339, 796 p.
5. **Лю, Я.**, Подстєвая, Т., Середя, В. (2023). Високоєфективний контактний зволожувач для термічної опріснювальної установки. *Сучасні проблеми наукового забезпечення енергетики: матеріали XX Міжнародної науково-практичної конференції молодих вчених та студентів у 2-х т. (с. 226-227)*, м. Київ, 25–28 квітня 2023 р. – Київ: КПП ім. Ігоря Сікорського, видавництво «Політехніка», 2023. – ISBN 978-966-990-072-2 (Т. 1). – 256 с.
6. **Лю, Я.**, Подстєвая, Т., Середя, В. (2025) Експериментальне дослідження оптимальної продуктивності плівкового зволожувача для термічної системи опріснення. *Сучасні проблеми наукового забезпечення енергетики: матеріали XXII Міжнародної науково-практичної конференції молодих вчених і студентів у 2-х т. (с. 164-166)*, м. Київ, 22–25 квітня 2025 р. – Київ: КПП ім. Ігоря Сікорського, видавництво «Політехніка», 2025. – ISBN 978-966-990-153-8 (Т. 1). – 215 с.

**APPENDIX B: The act of implementation
in the China Hydrogen Energy Group**

China Hydrogen Energy Group Co., Ltd.

National Technical University of Ukraine

“Igor Sikorsky Kyiv Polytechnic Institute”

Implementation Act of the dissertation research for obtaining the degree of Philosophy Doctor in specialty 144 “Heat Power Engineering” 25.09.25 the Process National Technical University of Ukraine “Igor Sikorsky Kyiv Polytechnic Institute”, postgraduate Mr. Yang Liu.

By this implementation act, I confirm that the results of the dissertation research “Increasing the efficiency of contact humidifiers in the operating conditions of thermal water desalination systems.” were used in the China Hydrogen Energy Group Co., Ltd.

The results, obtained in term of experimental research and mathematical modeling, made it possible to reduce the energy consumption for water desalination in small-scale decentralized humidification-dehumidification system.

China Hydrogen Energy Group Co., Ltd.



APPENDIX C: The act of implementation in the Liaoning Hongsheng Environmental Solutions Technology

Liaoning Hongsheng Environmental Solutions Technology Co., Ltd.

Implementation Act of the dissertation research for obtaining the degree of Philosophy Doctor in specialty 144 “Heat Power Engineering” 25.09.25 the Process National Technical University of Ukraine “Igor Sikorsky Kyiv Polytechnic Institute”, postgraduate Mr. Yang Liu.

By this implementation act, I confirm that the results of the dissertation research “Increasing the efficiency of contact humidifiers in the operating conditions of thermal water desalination systems.” were used in the Liaoning Hongsheng Environmental Solutions Technology Co., Ltd.

Small scale solar desalination HDH system with film humidifier was built. Humidifier consist from 5 plastic tubes with heighth 1 m and diameter 40 mm. The installation allows you to get up to 40 liters of water per day. The electricity consumption is 2 kWh, so the cost of money is 0.156 Euro.

Liaoning Hongsheng Environmental Solutions Technology Co., Ltd.

